HIGH-PERFORMING SIMULATIONS OF THE SPACE RADIATION ENVIRONMENT FOR THE INTERNATIONAL SPACE STATION AND APOLLO MISSIONS

by

Matthew Lawrence Lund

A thesis submitted to the faculty of
The University of Utah
in partial fulfillment of the requirements for the degree of

Master of Science

in

Nuclear Engineering

Department of Civil and Environmental Engineering

The University of Utah

May 2016

The University of Utah Graduate School

STATEMENT OF THESIS APPROVAL

The thesis of **Matthew Lawrence Lund**

has been approved by the following supervisory committee members:

Tatjana Jevremovic , Chair **1/25/2016**
Date Approved

Terry Arthur Ring , Member **1/25/2016**
Date Approved

Wayne Springer , Member **1/25/2016**
Date Approved

and by **Michael Earnest Barber** , Chair/Dean of

the Department/College/School of **Civil and Environmental Engineering**

and by David B. Kieda, Dean of The Graduate School.

ABSTRACT

The space radiation environment is a significant challenge to future manned and unmanned space travels. Future missions will rely more on accurate simulations of radiation transport in space through spacecraft to predict astronaut dose and energy deposition within spacecraft electronics. The International Space Station provides long-term measurements of the radiation environment in Low Earth Orbit (LEO); however, only the Apollo missions provided dosimetry data beyond LEO. Thus dosimetry analysis for deep space missions is poorly supported with currently available data, and there is a need to develop dosimetry-predicting models for extended deep space missions.

GEANT4, a Monte Carlo Method, provides a powerful toolkit in C++ for simulation of radiation transport in arbitrary media, thus including the spacecraft and space travels. The newest version of GEANT4 supports multithreading and MPI, resulting in faster distributive processing of simulations in high-performance computing clusters. This thesis introduces a new application based on GEANT4 that greatly reduces computational time using Kingspeak and Ember computational clusters at the Center for High Performance Computing (CHPC) to simulate radiation transport through full spacecraft geometry, reducing simulation time to hours instead of weeks without post simulation processing. Additionally, this thesis introduces a new set of detectors besides the historically used International Commission of Radiation Units (ICRU) spheres for calculating dose distribution, including a Thermoluminescent Detector (TLD), Tissue Equivalent Proportional Counter (TEPC), and human phantom combined with a series of new primitive scorers in GEANT4 to calculate dose equivalence based on the International Commission of Radiation Protection (ICRP) standards. The developed models in this thesis predict dose depositions in the International Space Station and during the Apollo missions showing good agreement with experimental measurements. From these models the greatest contributor to radiation dose for the Apollo missions was from Galactic Cosmic Rays due to the short time within the radiation belts. The Apollo 14 dose measurements were an order of magnitude higher compared to other Apollo missions. The GEANT4 model of the Apollo Command Module shows consistent doses due to Galactic Cosmic Rays and Radiation Belts for all missions, with a small variation in dose distribution across the capsule. The model also predicts well the dose depositions and equivalent dose values in various human organs for the International Space Station or Apollo Command Module.

CONTENTS

CHAPTERS

APPENDICES

ACKNOWLEDGMENTS

I am grateful for the advice and mentoring of Dr. Tatjana Jevremovic; without her this thesis would not be possible. She has graciously reviewed presentations, abstracts, publications, and this thesis with insightful and helpful revisions. I'm grateful to the entire faculty at the Utah Nuclear Engineering Program for all the material and information I have learned over the course of my master's program. I thank Dr. Terry Ring for feedback and advising in research group and Dr. Wayne Springer for his assistance.

I would also like to thank Dr. Tori Ersmark for his GDML models of ISS from the DESIRE project; the models were invaluable to benchmark simulations. I'm grateful to Dr. Eric Benton from Oklahoma State University for Apollo mission dose data and his correspondence. I am thankful for Dr. Kerry Lee and Dr. Dan Fry, along with the Space Radiation Analysis Group at Johnson Space Center, where I had the opportunity to complete an internship and learn so much about space weather, radiation, and modeling. I'm grateful for their support and pictures of space detectors.

I would like to thank the Center for High Performance Computing at the University of Utah for their support in providing computational time on the Ember and Kingspeak cluster, without which this thesis wouldn't be possible. I'm grateful for the assistance of Wim Cardoen at CHPC for installing and updating GEANT4, and for assistance in code issues. I'm thankful for the online SPENVIS and OLTARIS database used to access radiation environment models, CelesTrak for TLE element data, and SILSO World Data Center for solar cycle data. I would like to thank the Utah Nuclear Engineering Program for funding and support and the Nuclear Regulatory Commission Fellowship for funding, without which this research would not be possible.

Finally I'm very grateful to my family for their support and for instilling a love of learning. Without the support of family and friends, I would not have been able to finish this thesis.

CHAPTER 1

INTRODUCTION

1.1 Motivation

The space radiation environment is one of the limiting factors to deep-space human explorations. The International Space Stations (ISS) and shuttle missions well documented radiation exposure in Low Earth Orbit (LEO); however, the radiation environment of the moon and deep space is not well characterized [1]. The high levels of radiation in space prevent manned long-duration missions to deep space unless better shielding materials are found, along with better tools to precisely predict the exposure rates to astronauts and electronic equipment.

During the late 1960s and 1970s, the United States sent ten manned missions to the moon. During the time, very little was known of the effects of radiation and radiation shielding. On Earth, humans are protected by the Earth's magnetic field and atmospher, which deflect Solar Particle Events (SPE) and Galactic Cosmic Rays (GCR). Earth's magnetic field also creates an area of higher radiation known as the Van Allen belt, where particles are trapped. As the Apollo astronauts left Earth's protective magnetic field, the radiation dose increased to higher levels than for astronauts in LEO. Thus the dose rates for the astronauts on the Apollo missions over the period were higher than would be acceptable for future longer missions to Mars and deep space. For example Apollo astronauts received a dose of 1.6 mGy to 14 mGy over two weeks. Assuming a quality factor of around four, the missions resulted in an equivalent dose of 6.4 mSv to 56 mSv in just a couple weeks during the Translunar voyage, which is greater then the allowable radiation workers' yearly dose limit of 50 mSv and maximum public allowable exposure limit of 1 mSv.

Astronauts are exposed to the space radiation environment containing ionizing radiation of high energy from mostly heavy-ions, protons, and beta particles. This radiation then passes through spacecraft shielding, causing secondary radiation through interactions like bremhstrulung, elastic scattering, inelastic scattering, Compton scattering, radiative capture, etc. This primary and secondary radiation are possible to predict using accurate models of the spacecraft combined with Monte Carlo methods, which provide a powerful tool to analyze and predict particle interactions and radiation doses. The DESIRE study provided a detailed full spacecraft geometry with Monte

Carlo methods to predict astronaut dose for the Columbus module of the International Space Station (ISS) [2]; however, the study used extensive postprocessing, long computational times due to single threaded application, and was without anatomical human phantoms. A Monte Carlo model of the Apollo missions does not exist. During the Apollo missions, the capsules were made merely of aluminum with insulation, thus had very little shielding as opposed to more heavily shielded ISS. Current studies of radiation shielding for future missions suggest using Nomex, Kevlar, polyethylene, borated polyethylene, boron nanotubes, or blankets of water to shield against radiation. For example, water would be an ideal shielding material due to being mostly hydrogen, which has a small atomic mass, thus absorbing more energy in an elastic collision with an ion. The best future shielding materials will have a high ability to slow down and stop heavy high-energy ions with minimal secondary products. Thus future designs will require the ability to test new materials quickly with high-fidelity simulations. NASA developed HZETRN [3] and OLTARIS [4] applications to model radiation transport in the space environment, whereas the European Space Agency (ESA) developed MULASSIS [5] and GRAS [6] applications based on GEometry ANd Tracking 4 (GEANT4). The applications are independent computer software programs that use an input geometry and particle spectrum files to simulate the radiation through a spacecraft, scoring radiation interactions. These applications run a single calculation at a time as a single thread; however, the newest version of GEANT4 supports multithreading and Message Passing Interface (MPI), allowing for much faster distributive simulations across high-performance computing clusters through computational parallelism, reducing computational times from weeks to just a few hours. The GRAS and SPENVIS applications are tied to older, single-thread versions of GEANT4 not allowing for parallelism.

This thesis advances the design and implementation of a high-performance computer application, based on GEANT4, to quickly and precisely model the space radiation environment through a full-sized spacecraft. This newly developed model and application allows for the quick prototyping of new materials in shielding, precise prediction of astronaut dose, and energy deposition within sensitive electrons in economical computational times. As missions increase in length, astronauts will reach closer to the allowed lifetime exposure limits possibly excluding astronauts from missions. Thus more precise simulations allow for better mission planning and protection of astronaut health.

1.2 Thesis Objectives

This thesis aims to improve spacecraft simulations in the space radiation environment by the following objectives:

1. Demonstrate the need for a better computational application and outline the methodology needed for simulating full-sized spacecraft.

2. Develop a new simulation application to predict radiation transport through a full-sized spacecraft quickly using high-performance computing.
3. Benchmark the effectiveness of the application and reproducibility to actual experimental data.
4. Implement a series of space radiation detectors based on Thermoluminescent Dosimeters, Tissue Equivalent Proportional Counters, International Commission on Radiation Units Spheres, and anatomical human phantoms for use within this new simulation application. Thermoluminescent Dosimeters and Tissue Equivalent Proportional Counters are used currently for dosimetry on the ISS, whereas International Commission on Radiation Units Spheres and anatomical human phantoms are used currently for dose predictions in current radiation transport models.
5. Create a new GEANT4 statistics model to predict the simulation error for the application, since GEANT4 internally does not provide a statistical error model of stochastic modeling like other Monte Carlo codes such as, for example, MCNP [7].
6. Create new equivalent dose scorers for GEANT4.
7. Improve current simulation models from DESIRE project of the International Space Station (ISS).
8. Simulate the radiation dose during Apollo 11 and 14 missions in order to understand what produced the magnitude difference in exposure for Apollo 14.
9. Create dynamic visualizations of radiation dose progressions during space flights.

1.3 Organization of Thesis

In Chapter 2 the radiation environment in space of interest to space radiation model is described. Chapter 3 compares the existing radiation transport codes used to model space radiation through spacecraft. Chapter 4 explains GEometry ANd Tracking 4 (GEANT4) along with the components needed to create simulations of space missions in the new application. Chapter 5 describes dosimeters currently used in space. Chapter 6 summarizes outcomes of previous studies of the ISS along with new simulations of the ISS in high-performance computing clusters. Chapter 7 describes the Apollo missions and created models of the Apollo missions. Chapter 7 outlines the conclusions and future work.

CHAPTER 2

RADIATION ENVIRONMENT IN SPACE

2.1 Introduction

The radiation environment in space is composed of Galactic Cosmic Rays (GCR); Earth's radiation belts, often referred to as the Van Allen Belts; Solar Particle Events (SPE); and albedo neutrons and protons. GCRs are composed of protons, alpha particles, and heavy-Z ions (HZE) in energy up to 1000 TeV. The trapping of charged particles within the magnetosphere causes Earth's radiation belts as protons and electrons follow the magnetic field lines from magnetic pole to pole. The interaction of GCRs with the atmosphere causes the albedo neutrons and protons. Solar Particle Events are mostly energetic protons and electrons from the Sun released during solar activity. Table 2.1 shows the composition of these radiation sources, models of the source, and the effect on spacecraft, each of which is described in detail in the following sections [8].

In Low Earth Orbit (LEO), the trapped radiation belts and GCR contribute most to astronaut dose, since Earth's magnetosphere shields spacecraft from SPEs except at latitudes near the poles. At high latitudes, GCR contributes more, whereas at mid latitudes the South Atlantic Anomaly, an area off the coast of Brazil where the trapped radiation belt descends to lower altitudes, contributes more, shown in Figure 2.1. The dotted line in Figure 2.1 shows the orbit of the ISS around Earth, with each dot representing the dose from the TEPC radiation detector onboard, described in chapter 5. As, the ISS approaches the coast of Brazil, the dose rate increases, as shown, due to the radiation belts; whereas when the spacecraft approaches the poles, Figure 2.1 shows that GCR contributes more to astronaut dose. As a spacecraft leaves LEO, the craft will pass through the Radiation Belts, which significantly impact spacecraft at higher altitudes around Earth. The Radiation Belts are a significant hazard for manned missions, thus spacecraft trajectories such as during the Apollo Missions are designed to quickly pass through the belts, resulting in as minimal dose as possible to astronauts [9, 10]. In free, space within the Solar System, GCR dominate the astronaut dose except for sporadic SPEs, which probability minimize during solar minimum.

Table 2.1: Radiation Environment in Space [8]

	Galactic Cosmic Rays	Earth's Radiation Belts	Solar Particle Events	Albedo Neutrons and Protons
Composition	87% Protons 12% Alpha 1% Heavy Ions 2% Electrons and Positrons	Electrons < 6 MeV Protons < 250 MeV	Low Energy Protons and Electrons with some heavy ions	Neutrons Protons
Solar Cycle Effect	Decreases with solar max.	Solar max creates temporary radiation belts and changes altitude. East/West Anisotropy changes with cycle.	Increases frequency and magnitude with solar max.	
Earth's Magnetic Field Effect	In LEO protected by cutoff rigidity of magnetosphere varying with latitude and particle direction.	Caused by magnetic field with a higher area over Brazil known as South Atlantic Anomaly.	In LEO protected by cutoff rigidity of magnetosphere varying with latitude and particle direction.	Caused by magnetosphere trapping of particles from GCR collision with atmospheric atoms.
Models	Badhwar/O'Neill CREME96	AE-8 AP-8 AE-9 AP-9	NOAA Space Environment Monitoring, GOES Satellites, Neutron Ground Monitoring	AE-8 AP-8 AE-9 AP-9
Effect on Dose in LEO	~50% of ISS Dose Dominates for high-inclination orbits	~50% of ISS Dose Dominates for low-inclination and high-altitude orbits	Unknown	Little effect
Effect on Dose in Free Space	Constant		Varies with Solar Cycle	
Spacecraft Shielding's Effects	Little attenuation by shielding. Target fragmentation by heavy ions and protons creating secondaries.	Low Energy- attenuated High Energy- Target Fragmentation creating secondaries.	Low Energy- attenuated High Energy- Target Fragmentation creating secondaries.	Low energy attenuated.

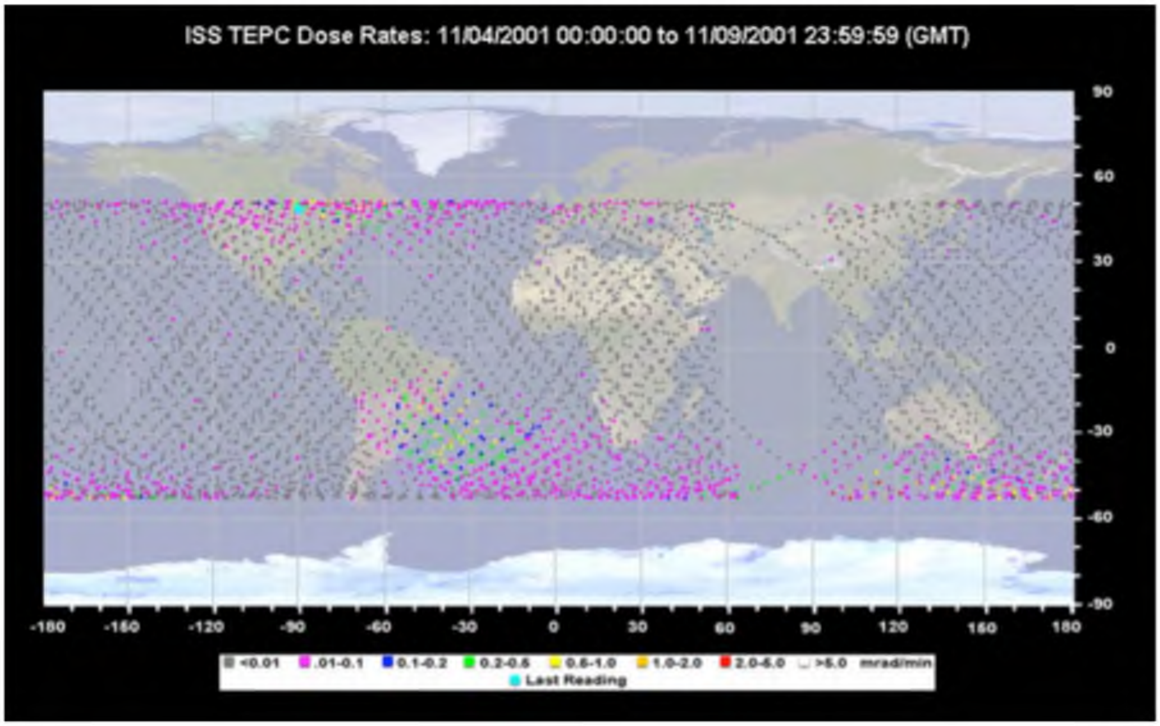

Figure 2.1: Astronaut dose rates from the TEPC instrument onboard the ISS. Graphic by Space Radiation Analysis Group, Johnson Space Center, NASA, used by permission [11].

The radiation environment in space is measured in terms of current, flux, and fluence, which describe the radiation intensity, directionality, and energies. Current is the scalar net number of particles passing through a unit area, whereas flux is a vector quantity describing the total number of particles passing in a direction through a unit area. The integral flux is the total number of particles above an energy passing through a volume, whereas the differential flux is the number of particles within a given energy range passing through the unit area in a direction. The differential flux is historically found from the integral flux by using the derivative of a second-degree interpolating Lagrange polynomial, as shown:

$$\frac{dP(x)}{dx} = \frac{2x - x_2 - x_3}{(x_1 - x_2)(x_1 - x_3)} y_1 + \frac{2x - x_1 - x_3}{(x_2 - x_1)(x_2 - x_3)} y_2 + \frac{2x - x_1 - x_2}{(x_3 - x_1)(x_3 - x_2)} y_3 \tag{2.1}$$

Thus written as a Lagrange polynomial, the differential flux is then given in terms of the energy bins (i) from 1 to n and integral flux (F), as shown:

$$\begin{aligned} f\left(E_i\right) = \;& -\tfrac{E_i - E_{i+1}}{(E_{i-1} - E_i)(E_{i-1} - E_{i+1})} F(E_{i-1}) - \tfrac{2E_i - E_{i-1} - E_{i+1}}{(E_i - E_{i-1})(E_i - E_{i+1})} F(E_i) \\ & -\tfrac{E_i - E_{i-1}}{(E_{i+1} - E_{i-1})(E_{i+1} - E_i)} F(E_{i+1}) \end{aligned} \tag{2.2}$$

$$\begin{aligned} f\left(E_1\right) = \;& -\tfrac{2E_i - E_2 - E_3}{(E_1 - E_2)(E_1 - E_3)} F(E_1) - \tfrac{E_1 - E_3}{(E_2 - E_1)(E_2 - E_3)} F(E_2) \\ & -\tfrac{E_1 - E_2}{(E_3 - E_1)(E_3 - E_2)} F(E_3) \end{aligned} \tag{2.3}$$

$$f\left(E_n\right) = -\frac{E_n-E_{n-1}}{(E_{n-2}-E_{n-1})(E_{n-2}-E_n)}F(E_{n-2}) - \frac{E_n-E_{n-2}}{(E_{n-1}-E_{n-2})(E_{n-1}-E_n)}F(E_{n-1}) - \frac{2E_n-E_{n-2}-E_{n-1}}{(E_n-E_{n-2})(E_n-E_{n-1})}F(E_n) \tag{2.4}$$

Radiation flux around the Earth is an anisotropic; however, for simulations the flux is assumed to be omnidirectional, requiring the flux to be integrated over the solid angle, multiplied by 4π. The fluence is the total particles passing through a given volume given by integrating the flux over the time interval [12]. The total flux or fluence varies with each type of radiation: GCR, Earth's radiation belts, albedo neutrons, and SPE. Within the solar system, SPEs generate the highest flux and dose, with a small contribution by GCRs [8]. The relative intensities of each radiation vary with orbit location within Earth's protective magnetic field and time period during solar cycle.

2.2 Solar Particle Events (SPE)

The sun constantly releases particles in an unending solar wind from its surface. The Sun's large fusion engine creates vast amounts of heat, radiation, and neutrinos constantly leaving the plasma surface. The outside layers are superheated through its atmosphere, creating energetic plasma ions with enough energy to escape the Sun's gravity as part of the solar winds.

The surface of the sun itself is a tumultuous place due to the ever-changing magnetic field, which cause solar events such as sunspots, solar prominences, solar flares, and coronal mass ejections. The faster rotation of the Sun's equator causes the magnetic poles of the Sun to swap every eleven years [13]. Before the poles flip, the magnetic fields become warped, causing them to twist in loops outside of the Sun's surface creating solar prominences. When the lines become so tightly twisted, the field lines break, releasing plasma as one of two types of Solar Particle Events (SPEs): impulsive flares or Coronal Mass Ejections (CMEs). Impulsive flares occur usually over hours, with high fluxes of electrons but with low total fluence between 107 to 108 particles/cm^{2}s. CMEs produce SPEs over days, with total fluence over 109 particles/cm^{2}s [14]. Figure 2.2 shows historical major SPEs available in OLTARIS database. The highest historical event was in September 1859, shown in the red line on Figure 2.2 [15]. The fluence for each event varies up to three orders of magnitude with particle fluence dropping with increasing energy up to 1 GeV.

The National Oceanic and Atmospheric Administration (NOAA) tracks SPEs at the Space Weather Prediction Center (SWPC) using the Advanced Composite Explorer (ACE) satellite, Geostationary Operational Environmental Satellites (GOES), and Polar-orbiting Operational Environmental Satellites (POES). Historical data may be accessed through OLTARIS, SPENVIS, or NOAA Space Weather Prediction Center database.

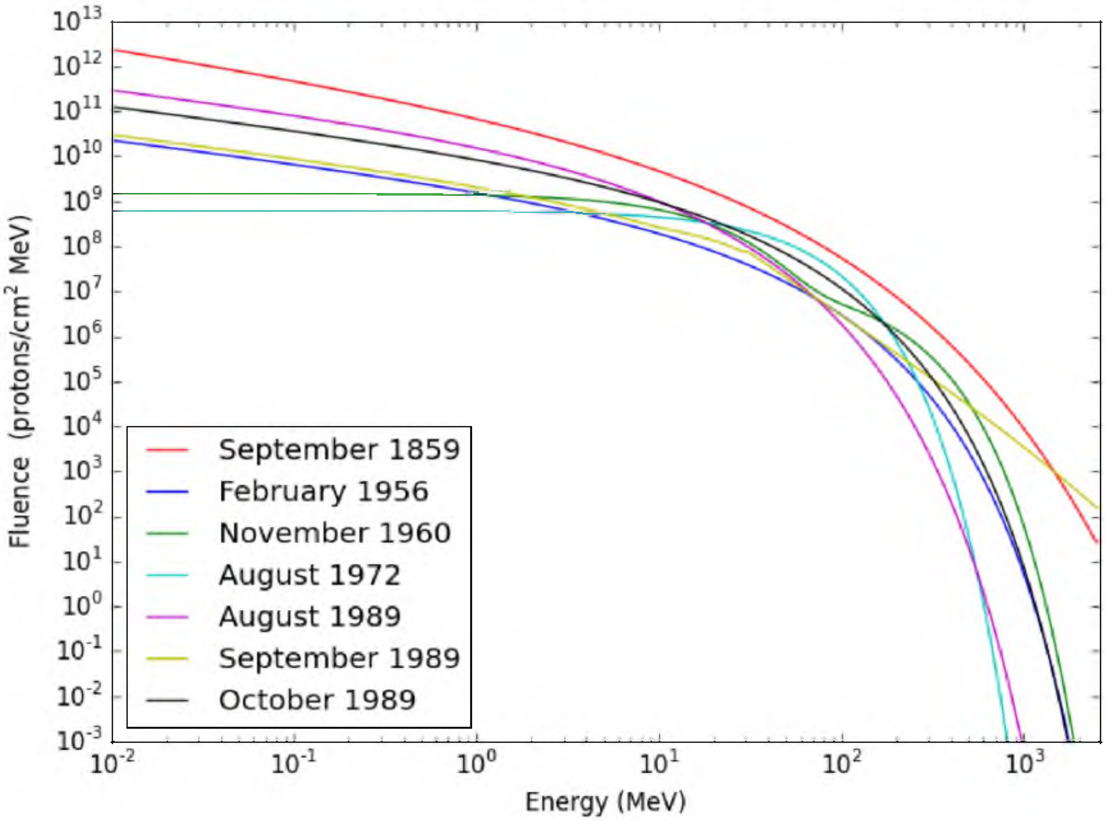

Figure 2.2: Historical SPE's fluences versus energy from OLTARIS database [4].

2.3 Galactic Cosmic Rays (GCR)

Baade and Zwicky in the early 1930s theorized that supernovas create the high energy of galactic cosmic rays (GCRs). The supernova shock waves accelerate the particles in GCRs to very high energies; however, the exact mechanism of GCR creation is still unknown [16]. GCRs are isotropicly distributed charged particles originating from outside the solar system, ranging in energy from 10-1012 MeV. The GCR spectrum peaks around 1 GeV within the solar system, consisting of 98% baryons: 87% protons, 12% alpha particles, and 1% heavy ions from Lithium to Uranium. The remaining 2% are leptons (electrons and positrons). The heavy ions, HZE, contribute significantly to radiation dose, especially from the abundant iron nuclei that have high linear energy transfer (LET) [8]. The distributions of GCR flux as a function of ions are shown in Figure 2.3, whereas the elemental flux versus the energy is shown in Figure 2.4 [17]. Figure 2.3 shows the highest flux is from hydrogen ions, followed by helium (alpha particles) then carbon, oxygen, and iron. Figure 2.4 shows the GCR flux peak at around 1 GeV.

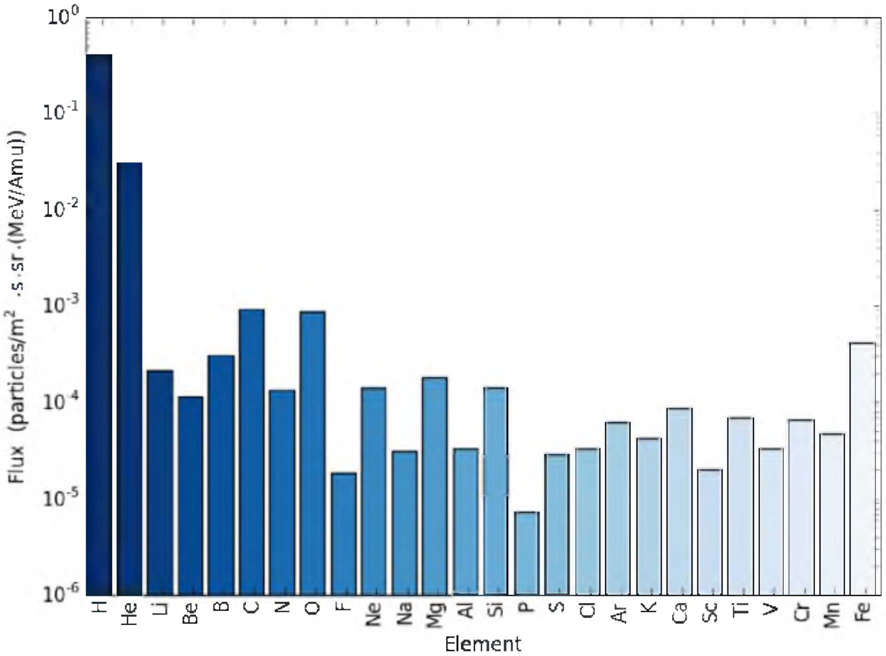

Figure 2.3: GCR ion fluxes at 1 MeV based on CREME96 database [17].

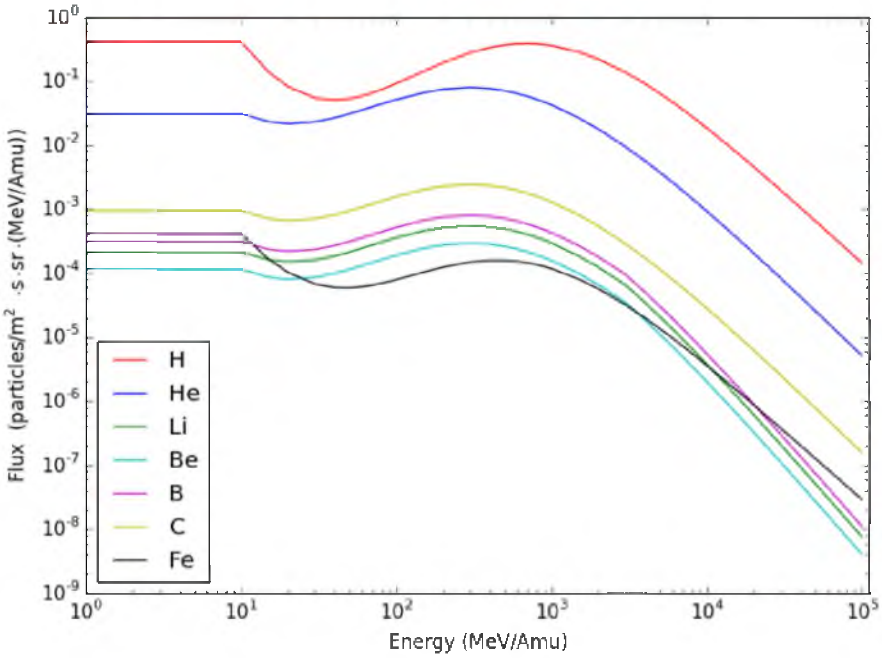

Figure 2.4: GCR ion flux vs. energy based on CREME96 database [17].

Galactic Cosmic Ray intensity within the solar system changes with the 11 year solar cycle. GCR flux below 1 GeV drops during solar maximum, attenuated by the increased solar winds [18]. Low-energy GCRs follow Earth's magnetic field lines to the poles, resulting in higher flux in LEO, whereas the GCR flux is less at the equator, with only high-energy GCR affecting spacecraft in LEO. GCR also include anomalous cosmic rays, which are low energy, nonpenetrating into a spacecraft.

Several different models give estimations of GCR flux based on observational data: namely the CRÈME model of Adams, Badhwar, and O'Neill and the CRÈME Nymmik model, an improvement on the original model [19]. CREME96 uses the CRÈME Nymmik model, which is available over the internet through the CREME96 website and SPENVIS [20]. The models predict GCR flux based on solar activity and heliospheric magnetic field during the solar cycle [21]. Since GCR are deflected by the Earth's magnetic field, the models also calculate GCR flux at locations around the Earth based on the particle flux rigidity and energy within the geomagnetic field. These models provide input GCR fluxes to model GCRs through the spacecraft simulations.

2.4 Trapped Radiation Belts

James Van Allen discovered the radiation belts in 1958 during the Explorer 1 mission [22]. The trapped radiation belts (Van Allen Belts) consist of mostly protons and electrons, which follow the Earth's geomagnetic field. The particles move back and forth from mirror points in the Northern and Southern Hemispheres, revolving around the field lines in cyclotron motion caused by the dipole nature of the magnetic field [8]. The belts form two regions: the Inner Belt dominated by protons and the Outer Belt dominated by electrons both, shown in Figure 2.5. Trapped protons drift west, and electrons drift east, giving the particles an anisotropic distribution, as shown for protons in Figure 2.6 for the ISS at 380 km and 51.6° inclinations. Since the energies and fluxes of the trapped protons are greater than the electrons, the trapped protons create a higher dose to astronauts in LEO [18].

The consistent inner electron belt ranges from 1.2 to 3 Earth radii of 6,371 km with energies below about 5 MeV formed by inward radial diffusion of electrons from the outer belt by Coulomb scattering and whistler mode pitch angle diffusion, which occurs when the electrons oscillating in the magnetosphere rotating in right-hand circularly polarized waves oscillate until the particle's velocity vector is diffused away from the mirror-magnetic field line. The outer electron belt ranges from 3 to 7 Earth radii, with energies below about 7 MeV varying in flux with solar cycles [23]. The outer belt flux is a magnitude greater than the inner flux, with energies below the required 10 MeV for Bremsstrahlung production, thus the electrons are easily blocked by spacecraft skin, with little effect to astronaut dose [8].

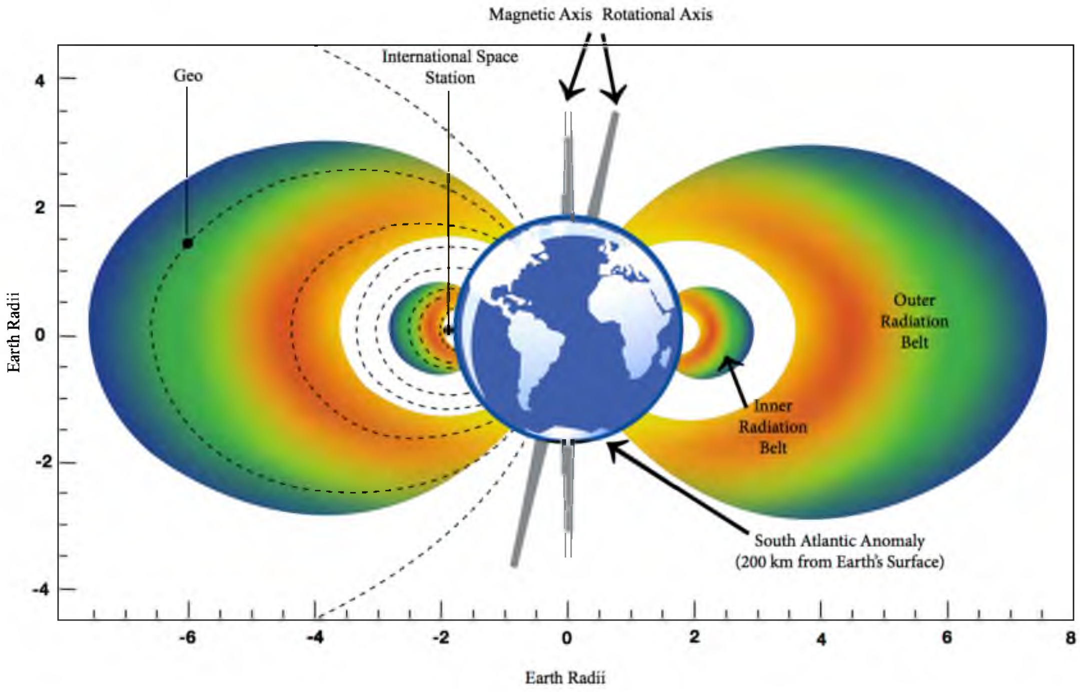

Figure 2.5: Diagram of Earth's radiation belts showing the inner and outer belt, South Atlantic Anomaly, magnetic and rotational axis, and ISS [24].

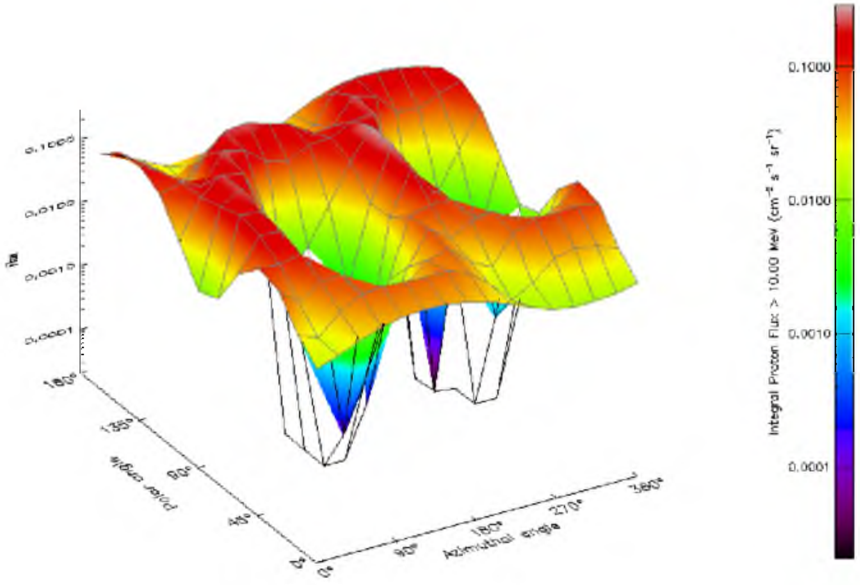

Figure 2.6: Anisotropic flux map for trapped protons for ISS at 380km and 51.6° inclination generated in SPENVIS [25].

Trapped protons occur in a single belt decreasing in flux with altitude starting at 800 km. The protons have energies below 400 MeV, with a broad energy distribution at around 150 MeV to 200 MeV. The trapped protons originate at different energies from capturing of solar particles, proton diffusion, and decay of Albedo neutrons. Albedo neutrons are secondary particles from the interaction of GCRs with Earth's atmosphere [26]. The free neutrons decay, with a half-life of about ten minutes, into protons.

Manned flights in LEO below most of the trapped protons except in the South Atlantic Anomaly (SAA), where the belt dips down to lower altitudes caused by the difference in Earth's rotation axis from the magnetic axis shown in Figure 2.5 [8].

The SAA off the coast of Brazil follows the ranges in longitude from -80° to 20° and latitude of -60° to 0° [27]. The SAA impacts astronaut dose for orbits below 800km and inclinations below 40° equally to the dose from GCR. Since the ISS orbit is roughly 400km and 51.6° inclinations, the SAA contributes the most to astronaut dose at mid latitudes, whereas GCR dominates at high latitudes near the poles [8].

The most widely used model of the trapped radiation belts is the AP8 and AE8 model from the 1980s by NASA, released as the RADBELT software package [28]; these models are now being replaced by the AP9 and AE9 models. J. Vette originally developed the models in the 1960s from satellite data, which have undergone several iterations [29]. The models are based off of McIlwain's (B, L) coordinate system for Earth's magnetic field, which creates a coordinate system based on the magnitude of the magnetic field and L-shells that describe the magnetic field lines based on the number of Earth-radii at the equator. The flux varies with solar cycle, resulting in the AP8-Max and AE8-Max models for solar maximum and AP8-Min and AE8-Min models for solar maximum [30].

Several other models exist to calculate fluxes for the trapped radiation belts, including the CRRESPRO for protons and CRRESELE for electrons from the Air Force Research Laboratory [31]. Another model is the European Space Agency's (ESA) sponsored TRapped Radiation Environment Development (TREND), which developed the PSB97 model in SPENVIS as a low altitude model for below 600 km for protons and electrons from the SAMPEX telescope [12]. Figure 2.7 shows a comparison between the models for integral and differential flux for each of the models of the trapped proton and electron radiation belt. Each model is based on different data sets with different energy ranges, thus each model has different minimum and maximum energies, as shown in Figure 2.7. The AP8 and AE8 models cover a larger energy spectrum compared to other models; however, the mid-energy spectra obtained with the CRRESPRO and CRRESELE models are underestimated. Solar minimum shown in the AP8 min spectrum has a larger flux and thus higher astronaut dose at lower altitudes than solar maximum AP8 max, due to the increased altitude of the radiation

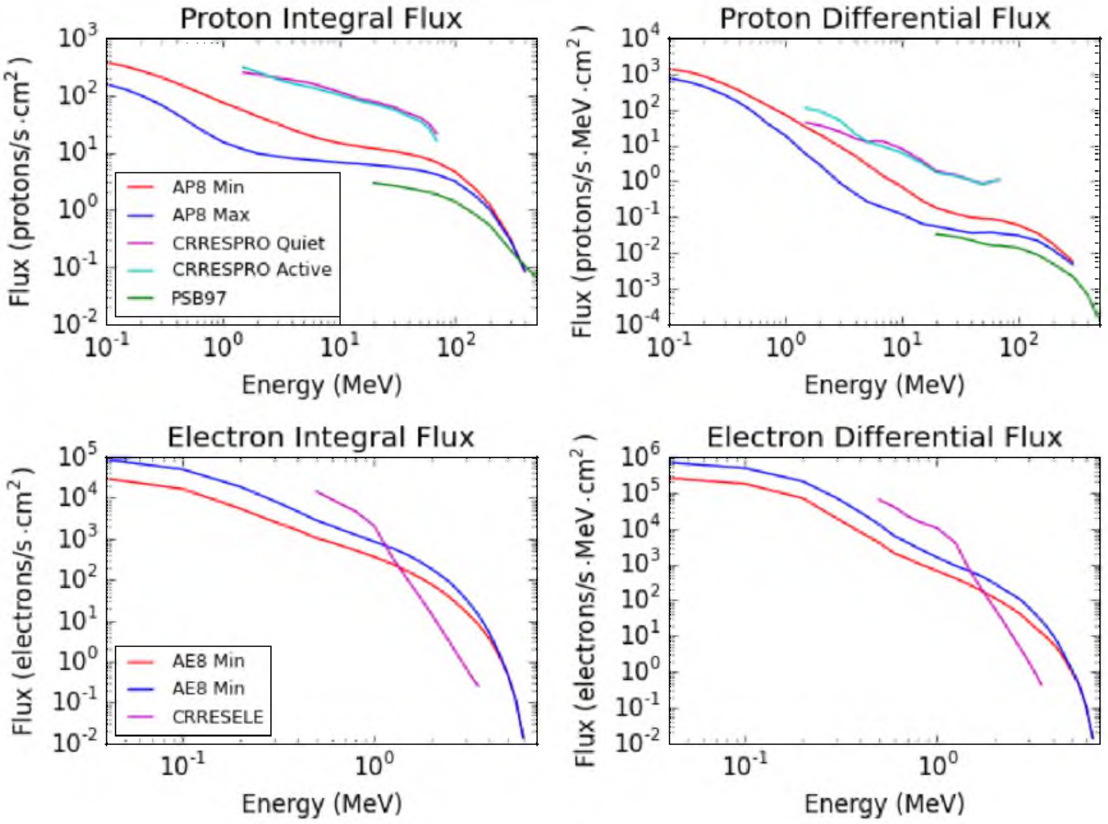

Figure 2.7: Comparison of trapped belt models showing integral and differential fluxes for protons and electrons at an 380 km altitude and 51.6° inclination for the ISS, data from SPENVIS [25].

belts during solar minimum from the increased particle fluence from the Sun. The CRRESPRO active and Quiet overestimate the flux, due to the smaller covered energy spectrum, shown in Figure 2.7. The electron flux for all the models is higher than the proton flux, due to the large flux in the electron-trapped radiation belts; however, since the spacecraft hull easily shields electrons, the electrons result in less radiation dose than the proton belts.

2.5 Biological Effects of Radiation

Radiation passing through the body can cause genetic effects, radiation carcinogenesis [32], acute radiation syndrome from high dose SPEs incapacitating crew [33], cataracts from radiation to the lens of the eye, late central nervous system effects [34], cardiovascular disease [35], premature senescence, immune system dysfunction, and microlesions from HZE particles. Charged particles including HZE directly deposit energy within matter, whereas neutrons, X-rays, and gamma rays are indirectly ionizing. As passing radiation interacts with matter, the particles interact, causing secondary radiation, including neutrons, Bremsstrahlung radiation, beta particles, and other smaller charged particles, each of which attributes to the total dose [36].

Heavy ions, alpha particles, beta particles, and other charged particles are directly ionizing radiation. The particles passing through cells ionize orbital electrons from atoms, which in turn release more energy away from the track. The energy deposited along the track length is called Linear Energy Transfer (LET). The greater the ion charge or kinetic energy, the higher the energy deposited along the track. Thus heavy Z-ions deposit high LET through their path length, resulting in greater cell damage [37]. The deposited energy breaks Deoxyribonucleic Acid (DNA) strands by breaking the electron bonds between chains. Beta particles cause single strand breaks due to the single charge; however, HZE or alphas have more energy, causing breaks across both strands. Strand breaks within DNA may lead to cancer or genetic changes; however, the risks from charged particles, especially HZE ions, are not as well understood compared to gamma and X-rays [38].

The effects of radiation are stochastic when they occur later in life, or nonstochastic when they occur quickly as a response to high radiation exposure. Nonstochastic effects are mostly deterministic effects with a threshold radiation dose and include Cerebro-Vascular Syndrome, Gastrointestinal Syndrome, Hematopoietic Syndrome, and skin burns. Long-term deterministic effects include cataracts with a clinically associated threshold 2 Gy of acute dose and 5.5 Gy long term low-LET radiation. High doses to the skin result in cancer and noncancerous late effects from cell death, including dermal vasculature [39].

Stochastic effects include genetic changes and cancer. Radiation exposure has been positively correlated to most solid cancers in organs with fast dividing cells such as lymphoid organs, bone marrow, gonads, intestines, and thyroid gland; and whole body dose has been linked to leukemia [40]. Due to the stochastic nature of cancer, both mortality rates and excess incidences are considered when determining guidelines for radiation exposure for cancer [39].

Radiation exposure is measured by absorbed dose and equivalent dose. Absorbed dose is the mean energy ($d\bar{\varepsilon}$) deposited per mass (dm) of trespassed tissue and can be expressed in differential form as follows:

$$D = \frac{d\bar{\varepsilon}}{dm} \tag{2.5}$$

The SI unit of dose is the Gray (Gy), one joule of energy deposited per kilogram of tissue, which is equal to 100 rads. Since each type of radiation has different ionizing potential, the equivalent dose weights the absorbed dose by its effect on tissue. The equivalent dose (H_T) is the sum of all the doses ($D_{T,R}$) multiplied by the weighting factor (w_R) for the relative biological effectiveness of each particle, shown as follows:

$$H_T = \sum_R w_R D_{T,R} \tag{2.6}$$

Equivalent dose is measured in Sieverts (Sv), which is one Joule per kilogram, equal to 100 Roentgen equivalent in man (rem) [41]. The International Commission on Radiation Protection (ICRP) has associated weighting factor for each type of radiation type; these values, however, have changed over the past years, depending on the ICRP report: ICRP-60, ICRP-92, or ICRP-103 [41,42]. Table 2.2 shows a comparison of the weighting factors from ICRP-60 and ICRP-103.

All federal agencies are required to comply with the Occupational Safety and Health Administration (OSHA) regulations under Presidential Executive Order 12196, thus NASA classifies astronauts as ionizing radiation workers with set limits. NASA follows the National Council on Radiation Protection and Measurements (NCRP Report 98 and 132) "Guidance on Radiation Received in Space Activities" [32]. Limits are set for a maximum increased lifetime cancer risk of 3%, which is higher than standard radiation worker limits. Table 2.3 shows the exposure limits for astronaut organs, and Table 2.4 shows the recommended career limit for males and females for less than a 3% excess risk for cancer [43].

NASA requires crewmembers' radiation exposure to be As Low As Reasonably Achievable (ALARA). For the ISS, the maximum 30 days dose is .25 Sv and Annual dose of .50 Sv [44]. NASA plans EVAs when the radiation levels are lower, as when avoiding solar storms and passing through the South Atlantic Anomaly (SAA).

Table 2.2: Weighting factors for equivalent dose by particle based on ICRP-60and ICRP-103 standards [41,42].

Radiation Type	ICRP-60 Weighting Factor	ICRP-103 Weighting Factor
Photons	1	1
Electrons, Muons	1	1
Protons, Charged Pions	2	2
Alpha Particles, Fission Fragments, HZE	20	20
Neutrons	<10 keV 5 10-100 keV 10 100 keV-2 MeV 20 2-20 MeV 10 > 20 MeV 5	$w_R = \begin{cases} 2.5 + 18.2e^{-[\ln(E_n)]^2/6} & \mathrm{E}_n < 1\mathrm{MeV} \\ 5.0 + 17.0e^{-[\ln(2E_n)]^2/6} & 1\mathrm{MeV} \leq \mathrm{E}_n \leq 50\mathrm{MeV} \\ 2.5 + 3.25e^{-[\ln(E_n)]^2/6} & \mathrm{E}_n > 50\mathrm{MeV} \end{cases}$

Table 2.3: Organ exposure limits for astronauts.

Exposure Time	Bone Marros (Gy-Eq)	Lens of the Eye (Gy-Eq)	Skin (rem)
30 days	.25	4.0	150
Annual	.5	200 rem	300
Career	.25	400 rem	600

Table 2.4: Astronaut career exposure limits.

AGE	NCRP-132 (Sv)		NCRP-98 (Sv)	
	Male	Female	Male	Female
25	.7	.4	1.5	1.0
35	1.0	.6	2.5	1.75
45	1.5	.9	3.2	2.5
55	3.0	1.7	4.0	3.0

CHAPTER 3

NUMERICAL METHODS USED TO MODEL RADIATION TRANSPORT IN SPACE ENVIRONMENT

3.1 Introduction

Radiation transport through materials is analyzed using several different mathematical methods; either using deterministic or Monte Carlo approaches. Deterministic methods solve for particle transport by various numerical methods such as NASA's BaRYoN TRaNsport (BRYNTRN) and NASA's High Charge Z and Energy TRaNsport (HZETRN) code, which are now integrated to an On-Line Tool for the Assessment of Radiation in Space (OLTARIS) [4]. Three-dimensional Monte Carlo codes solve radiation transport by using an event generator and tracking the possible statistical interactions. Monte Carlo codes include High Energy Transport Code-Human Exploration and Development for Space (HETC-HEDS) [45,46], FLUktuierende KAskade (FLUKA) [47], Monte Carlo N-Particle code (MCNP) [7], SHIELD, Particle and Heavy Ion Transport code System (PHITS) [48], and GEometry And Tracking version 4 (GEANT4) [49]. The deterministic and Monte Carlo methods applications show good agreement for similar spectra and geometry configuration within 5-10% from secondary particles like mesons, electrons, and gamma rays; however, HZETRN underestimates low-energy neutrons below 1 MeV. Studies of STS-91 and other missions for CR-39 and TLD dosimetry data show good agreement within 15% to HZETRN transport models [50].

Each application is explained in detail below, including advantages and disadvantages along with applicability to modeling space radiation. Modeling radiation transport through large areas such as spacecraft requires long computational times. Most of the codes except MCNP, PHITS, and GEANT4 are single-thread codes running a single calculation at a time. Thus this thesis addresses the need for an improved application that can quickly simulate radiation transport accurately in the space radiation environment.

3.2 Deterministic Methods for Radiation Transport

BRYNTRN solves the Boltzmann equation to transport high-energy baryon nucleons along a fixed path. The Boltzmann transport equation describes the distance traveled for a particle through material based on the proton stopping power $S(E)$, neutron total cross section σ_n, proton total cross section σ_p, elastic and nonelastic differential cross sections $f_i(E, E')$in terms of energy E, and flux $\phi_j\,(x, E')$ in a given location x and energy E, as follows [50]:

$$Protons: \left[\frac{\partial}{\partial x} - \frac{\partial}{\partial E} S\,(E) + \sigma_p\,(E)\right] \phi_p\,(x, E) = \sum_j \int_E^{\infty} f_{pj}\,(E, E')\phi_j\,(x, E')\,dE' \quad (3.1)$$

$$Neutrons: \left[\frac{\partial}{\partial x} + \sigma_n\,(E)\right] \phi_n\,(x, E) = \sum_j \int_E^{\infty} f_{nj}\,(E, E')\phi_j\,(x, E')\,dE' \quad (3.2)$$

The application calculates secondaries from fragmentation caused by the collision of charged particles with the nucleus of an atom, resulting in the nucleus breaking apart. The total cross section for interactions within the application is found by summing several empirical formulas at four energy groups instead of using large experimental cross-sectional databases, as other applications. For example, fragmentation cross sections are calculated by using Rudstam formalism [51]. Light fragment yields are from Bertini's MECC7 calculations [50], with the heavy fragment yield from empirical formulas verified with experimental data from the Heckman group at Lawrence Berkeley Laboratory [52].

HZETRN code integrates the Galactic Heavy Ion Transport code (GCRTRN) and the BRYNTRN code into a single package to solve the Boltzmann Equation with straight ahead approximation and continuous slowing down [3]. HZETRN has been verified for SPEs, GCRs, and the trapped radiation belts to analyze dose and dose equivalent [53]. The code solves light particles ($A \leq 4$) and heavy particles ($A \geq 4$) using two different algorithms, which have been improved in current versions for better convergence and faster simulations [53–55].

3.3 Monte Carlo Methods

Monte Carlo Methods create a statistical sample of a complex problem for which a direct solution is unattainable. Stan Ulam first suggested the method on March 11th, 1947 in a handwritten letter to Robert Richtmyer suggesting a possible statistical approach to solve the neutron diffusion equation [56]. Nicholas Metropolis suggested the name Monte Carlo because of Stan Ulam's uncle, who borrowed money, saying, "just had to go to Monte Carlo." Ulam explained in his letter a method in which neutron's individual paths are modeled statistically while undergoing the processes of scattering, absorption, fission, and leakage in a spherical core of fissionable material. The end behavior of the neutrons is calculated by taking a large enough statistical size of all possibilities to reach a distribution. Initially a neutron is randomly given a velocity and position by use of random numbers. Next the neutron is tracked a distance until undergoing an interaction. The neutron's probability of undergoing each interaction is weighted, giving an interaction of either scattering with an angle, absorption within the media, leakage from the media, or fission releasing several new neutrons that are then tracked. Each neutron is then tracked through sequential materials until either the neutron has scattered below a tracked energy or out of the given geometry. Similarly, all particles, including leptons, mesons, baryons, hadrons, and high-z ions, are modeled in Monte Carlo following all possible interactions.

Monte Carlo requires a set of pseudo-random numbers, which form a list of numbers started from a random seed. The set of random numbers can be recreated by starting from the same seed, yet form a random distribution of numbers. Bad selection of random numbers can create a biased result in Monte Carlo with a false distribution, especially if the numbers are predominantly distributed over a high or low region. A random number is fed into a series of probability distribution functions (PDFs), which, given a large enough number of realization, will converge to a statistical solution representative of the function. The method requires a PDF describing each possible interaction, including probability for elastic scattering, inelastic scattering, Compton Effect, scattering angle, Photoelectric Effect, pair-production, mean free path, energy distribution, absorption, fission, etc.… The results of each interaction are totaled in bins to create a statistical sampling.

Two common methods are used to find the PDF: Direct Inverse Transformation Method and Rejection Method. The direct inverse method uses one random number in a range of zero to one. The distribution is calculated by normalizing the equation, then finding the CDF by integrating over the interval and then inverting. If the function cannot be integrated or inverted, the rejection method is used which finds the maximum value of the PDF, then randomly finds a point within a box of the domain, and then checks to see if the point is acceptable. The rejection method requires two random numbers.

Monte Carlo codes such as GEANT4, GEometry And Tracking version 4, from CERN, use a series of probability functions that model all the possible interactions. Then a random number feeds into the probability functions to see all the possible outcomes. Over a large number of particles, a pattern begins to emerge, representing a predicted pattern.

Many different codes implement Monte Carlo methods to transport radiation covering various energy ranges and particles as shown in Table 3.1; most are implemented in Fortran running as a sequential code. The codes have been extended to transport heavy ions, allowing for the simulation of radiation environment in space through spacecraft, each with different physics models of nuclear

Table 3.1: Comparison of Monte Carlo Codes used to Model the Space Radiation Environment

Code	Developers	Particles Transported	Maximum Energy	Language / Threading
MCNP	Los Alamos National Lab, USA	protons, neutrons, muons, photons, pions, and HZE ions	100 GeV	Fortran / MPI and OpenMP
HETC-HEDS	Oak Ridge National Lab and NASA, USA	protons, neutrons, muons, photons, pions, and HZE ions		Fortran / Sequential
FLUKA	INFN and CERN, Italy	61 particles and photons	1 GeV	Fortran / Sequential
SHIELD	JINR and NIR, Russia	any (A,Z) nuclei, nucleons, pions, kaons, antinucleons, and muons	1 TeV	Fortran / Sequential
PHITS	JAEA, Japan	protons, neutrons, mesons, nuclei, electrons, and photons	200 GeV	Fortran / OpenMP
GEANT4	CERN and GEANT4 Collaboration, International	protons, neutrons, muons, photons, pions, HZE ions, and other subatomic particles	Over 1 PeV	C++ / POSIX Threading, MPI, and TOPC

interactions. Each code transports particles up to varying energies. GEANT4 and FLUKA transport particles up to energies over 1 PeV, thus the codes are more effective for high-energy GCR. Only Phits, MCNP, and GEANT4 allow for multithread applications, thus the other codes require splitting large simulations into smaller runs with different random number seeds and merging the results at the end.

3.3.1 Monte Carlo N-Particle Code (MCNP)

MCNP started at Los Alamos National Lab from Group X-6 in 1977 as an amalgamation of earlier codes using Monte Carlo methods written in Fortran, since then undergoing several revisions. MCNP5 added MPI and OpenMP support in 2005 for implementation in high-performance computing clusters, thus greatly reducing computational time for large simulations. MCNPX was a spinoff project for specialized work including accelerators. The newest version MCNP6 combined MCNPX and MCNP5 into a single code [57]. MCNP transports radiation and calculates criticality, unlike the other Monte Carlo codes listed.

MCNP requires an input file with three blocks: a cell card block, surface card block, and data card block. Volumes and surfaces form cells to describe geometries in a Cartesian coordinate system with user-defined materials. MCNP6 uses the ENDF/B-VI nuclear libraries for cross section data. The input file can specify sources as isotropic, planar, or volumetric as specific energies, spectrum, or energy distribution. Particles are tallied in cells or grids using tally cards allowing for surface current, surface flux, cell flux, track-length, energy deposition, fission energy, and pulse height scoring [58]. Since all input data for a simulation are contained within one file, each simulation requires creating a uninque long input file. For the input file, VISED and McCad convert Computer Aided Drafting (CAD) drawings into MCNP input files [59], thus allowing quick implementation of spacecraft geometries from CAD drawings. MCNP allows for fast simulations due to parallelism by OpenMP and MPI.

3.3.2 High Energy Transport Code-Human Exploration and Development of Space (HETC-HEDS)

HETC-HEDS is an extension of High Energy Transport Code (HETC), developed at Oak Ridge National Laboratory during the 1970s written in Fortran for particle cascades [45]. The original transport code HETC only transported protons, neutrons, muons, and pions; however, HETC-HEDS adds heavy nuclei transport, nucleus-nucleus cross sections, and heavy ion interactions collision module [60]. HETC-HEDS is a single thread application that uses combinatorial geometry similar to FLUKA to define geometries by combining basic shapes. Simulations of fragment production and energy loss with HETC show close agreement to experimental data from HZE ions particle accelerator data; however, the code does not transport neutrons below 20 MeV and cascade photons or dexxcitation gammas, thus requiring transportation in another code such as MCNP [46]. Thus HETC requires multiple steps for modeling and single-thread computation.

3.3.3 FLUktuierende KAskade (FLUKA)

FLUKA is a collaboration between INFN and CERN that transports sixty different particles and photons from TeV to keV, including HZE ions. FLUKA is written in Fortran and uses the combinatorial geometry package to describe complex geometries. The greatest advantage for FLUKA over other applications is a python interface named FLAIR providing a GUI for creating input files and analyzing data. FLUKA is a sequential code running a single process, thus not as fast as other codes; however, FLAIR can create multiple simultaneous runs of the simulation using different random number seeds and then combine the data after runtime with postprocessing.

Johannes Ranft started the FLUKA Monte Carlo code between 1962-1967 as a code to design shielding for high-energy proton accelerators. The code has since undergone three major fundamental changes, and modernization. A. Ferrari and A. Fassò at INFN started the third generation in 1987 by transforming the code to multipurpose code capable of transporting multiple particles. During this iteration, the collaboration added heavy particle generation and transport. In 1997, S. Vanini added an interface allowing FLUKA to read GEANT4 geometry called FLUGG [61]. The code contains three-dimensional mesh scorers for particle fluence, yields, and energy deposition; however, the user cannot add any functionality or custom scorers to the code and does not propagate as many particles as GEANT4.

3.3.4 SHIELD

Sobolevsky and Barashenkov developed the SHIELD code in 1970 to transport high-energy particles to 1 TeV through complex targets using Monte Carlo methods. SHIELD was first developed at the Joint Institute for Nuclear Research (JINR) with further development from the Institute for Nuclear Research of the Russian Academy of Science (INR RAS). An atomic nuclei transport code was added to SHIELD in 1997, allowing for the transport of HZE ions for accelerators and space applications [62]. SHIELD accounts for energy loss due to ionization, 2-3 particle decays along paths, and neutron transportation using the twenty-eight-group ABBN data library for neutron transport. SHIELD allows for arbitrary chemical and isotopic composition within the geometry. The code uses the many stage dynamical model (MSDM) generator from Russian nuclear codes, the Dubna cascade model below 600 MeV, the quark-gluon string model (QGSM) above 10 GeV, an extension of QGSM for intermediate energies, and the Fermi Breakup Model for de-excitation of nuclei [62]. SHIELD only propagates particles up to 1 TeV, thus it cannot transport high-energy

GCRs and is a single thread application unable to take advantage of modern computational abilities.

3.3.5 Particle and Heavy Ion Transport Code (PHITS)

PHITS is based on NMTC/JAM [63] Monte Carlo Code written in Fortran with support for OpenMP threading. PHITS uses Evaluated Nuclear Data Libraries (ENDF) and the Japanese Evaluated Nuclear Data Library (JENDL) up to 20 MeV, LA150 library up to 150 MeV, and the JAM and JQMD models for high-energy particles and reactions only up to 200 GeV, which is a significant limitation for modeling high-energy GCRs. The code simulates particles in two categories: transport processes including gravitational and magnetic fields, and collision processes of particles with nuclei. PHITS calculates ionization processes such as interaction with electrons in a material as charged particles transport processes, calculating the energy loss in an external field during a trajectory [48].

Sato et al. created simulations of an imaginary vessel similar to the SPACEHAB module and compared the code with spectra from the Bonner Ball Neutron Detector (BBND) inside the SPACEHAB module on the Space Shuttle during STS-89 and STS-91. From the simulated spectra, the group predicted dose and equivalent dose, which showed good agreement with the experimental measurements for organs except for the stomach, because it ignored directional radiation distribution effects [64]; however, PHITS has not been compared as extensively as FLUKA, HETC-HEDS, or GEANT4 for simulating the space environment. PHITS allows for parallelism using OpenMP, which allows for multithreading on a single node; however, PHITS cannot take advantage of large computational clusters to reduce runtime without splitting runs into smaller runs and combining results at the end.

3.3.6 GEometry And Tracking version 4 (GEANT4)

GEANT4 provides a powerful tool set in C++ to model the radiation transport of radioactive sources through Monte Carlo Methods from which users may build custom applications. The tool set includes detailed physics models for all possible electromagnetic interactions, hadronic process including neutron and ion interactions, decay of excited nuclei, and radioactive decay with secondary products. GEANT4 contains multiple ways to record data from particle tracks and steps of interactions from which users can pull any particle information, including user-defined scorers. The G4PrimitiveScorer allows for easy macro file, based scoring within meshes, including multiflux, energy deposit, dose deposit, hits, and energy filters. G4SensitiveDetectors provides the same tool set for a defined geometry volume. Data can be output in custom, user-defined formats or as Root, a data analysis toolset from CERN, data files [49]. GEANT4 has been implemented with multithreading and MPI, allowing for easy implementation in a high-performance computing cluster.

The DESIRE project compared GEANT4 against Los Alamos experimental data and existing SHIELD-HIT and BRYNTRN code using the older G4BIC, G4LEAD, and G4LEPPC physics lists [65]. The study compared each physics list against experimental neutron yield data from a proton beam of 113 MeV and 256 MeV striking aluminum, beryllium, carbon, and iron. Since each model uses a combination of data-driven and theoretical models, all three physics lists resulted in slightly varying neutron yields at different energies that were model dependent. In comparison with SHIELD-HIT, the G4BIC model performed best with error less than the deviation in space radiation fluence.

In NASA's BRYNTRN code, the project constructed a 1-D slab geometry with shielding of 10g/cm^2 aluminum and 15 g/cm^2 measuring the neutron fluence. Then they created similar geometry in GEANT4 using a large-diameter cylinder with thickness of the shield and a large beam source with small scoring area. The simulations between GEANT4 using the G4BIC showed close agreement with the BRYNTRN code. G4BIC uses the Binary Cascade model for interactions discussed later, and forms the basis for the QBBC physics list model used in the current work [65]. Thus GEANT4 has been well validated for the simulation of the space environment.

3.4 Space Radiation Transport Software and Information Systems

3.4.1 Multi Layered Shielding Simulation Software (MULASSIS)

MULASSIS is a software application based on the GEANT4 framework funded by the European Space Agency (ESA). The software application simplifies running simulations using GEANT4 by allowing for simple User Interface (UI) commands and macro files for running of simulations without the need to write a custom application. MULASSIS simplifies geometry as one-dimensional planar layers or spherical shells with user-defined materials by elemental or isotropic composition with associated density. The software uses the General Particle Source to define either a point source or spherical shell of any energy or particle type definable in GEANT4. MULASSIS allows for the choice of several different hadronic and EM processes, including low-energy EM processes [5].

The software contains automated scorers selectable by UI or macro, including fluence, total ionizing dose, pule height spectrum, and Nonionizing Energy Loss (NIEL) for silicon materials, which can output data as histograms or comma separated values (CSV). Besides output of scorers, MULASSIS integrates with OpenGL allowing for the visualization of geometry, tracks, and secondaries. The software has been integrated into ESA's web-based SPENVIS environment for easy execution [5]. However, SPENVIS is limited to 1-D slab geometries, thus cannot simulate full-sized spacecraft.

3.4.2 GEANT4 Radiation Analysis for Space (GRAS)

GRAS is a software application also funded by ESA based on GEANT4, which extends the capabilities of MULASSIS, to three-dimensional geometries and additional scorers and options. All functionality in GRAS is also selectable by UI interface and macro file similar to MULASSIS and is available through SPENVIS. In GRAS geometry is selectable as GDML 3-D models or single layers, similar to MULASSIS. The software also allows for user-selectable physics list based on FTFP_BERT, QGSP_BIC, QGSP_BERT, QBBC, or custom physics lists with selectable EM processes, standard, or low-energy [6].

Analysis of data in GRAS is done by an analysis module accessible by UI commands. GRAS can score total ionizing dose (TID); NIEL; dose; equivalent dose based on ICRP-60, ICRP-90, or ICRP-103 standards; primary or secondary particle fluence; pulse height; LET spectra; and track length. All scorers can be applied to any volume with data output as histograms, tuples, csv, or simple text output. The analysis module is portable to other applications, allowing for easy implementation into user codes [6]; however, GRAS is limited to single thread based on earlier versions of GEANT4 not allowing for multithreading. Thus GRAS does not take advantage of modern computational capabilities.

3.4.3 Space Environment Information System (SPENVIS)

SPENVIS is a web-based tool and information system sponsored by the ESA and Belgian Institute for Space Aeronomy that integrates tools for trajectory generation, space radiation environment models, spacecraft charging, magnetic field, meteoroids and debris, MULASSIS, GRAS, and other GEANT4 tools. SPENVIS generates spacecraft trajectories using an orbit generator, which allows for creating multiple segments with mission-based start data and duration. The trajectories may be specified as elliptical, hyperbolic, geostationary, interplanetary, two-line element (TLE), trajectory file, or geographical coordinate grid for Earth or other planets. The system uses the generated ephemeris in the radiation environment models to generate spectra and fluxes for particles [31].

The information system generates spectra using NASA’s AP-8, AE-8, AP-9, and AE-9; AFRL CRRESPRO and CRRESELE; the SAMPEX/PET PSB97 model; SPE models for ESP total fluence, worst case events, and the King SPE model; and GCR using the CRÈME-86, CRÈME-96, ISO-15390, and Nymmik model. After generation of the particle spectrum, the GEANT4 tools in SPENVIS generate macro input files for particle sources including normalization values. The system then applies the spectrum to deterministic codes such as SHIELDOSE or EQFLUX code to estimate solar cell damage and NIEL along with Monte Carlo shielding simulation using GRAS and MULASSIS. The SPENVIS website integrates additional GEANT4 tools to build macro files, create geometries in GDML, model planet magnetic fields in Magnetocosmics and Planetocosmics, and model sector shielding [12]. SPENVIS generated the ephemeris data and spectrum input files for this thesis.

3.4.4 Cosmic Ray Effects on Micro Electronics (CRÈME) Website

The CRÈME website integrates the existing CRÈME-86 and CRÈME-96 models with trapped radiation models and GEANT4 Monte Carlo simulations for total ionizing dose and single event effects. The website uses the improved Nymmmik CREME-96 model to generate GCR flux along with a new model for albedo neutrons. The website integrates GEANT4 simulations for 1-D slab geometries and is built upon the Plon framework, which is written in Python [19]. The CRÈME database website provided comparison spectra for this thesis.

3.4.5 On-Line Tool for the Assessment of Radiation in Space (OLTARIS)

OLTARIS is the successor to the SIREST website, a web-based tool for simulating radiation based on HZETRN2005 and NUCFRG2 codes. OLTARIS uses a Ruby on Rails website core with a MySql database running on an Apache server. On job run, OLTARIS executes the computations on a Sun Grid computational cluster passing the data by Perl and Ruby scripts to the code running in Fortran [4].

An OLTARIS run requires five basic elements: radiation environment, material properties, geometry, radiation transport, and detector response function. The radiation environment is defined based on mission parameters as one of four different environments: a historic SPE or linear combination of SPE, free space GCR, lunar surface, or Earth orbit [4]. The radiation environment module was used for comparison of spectra to SPENVIS in this thesis.

Predefined materials, elemental composition, or chemical composition define each material in OLTARIS with NUCFRG2 and subroutines from earlier HZETRN2005 calculating the cross-section for each material. NUCFRG2 calculates the cross-section for heavy ions using the abrasion-ablation geometric model in which an incoming nucleus shears off part of the target nuclei based on impact parameters; however, NUCFRG2 inaccurately calculates the odd-even effect, because NUCFRG2 ignores quantum mechanical effects such as shell structure. The odd-even effect is where experimental observations show an increased probability of even-numbered nucleons over odd numbered. Nucleon and light ion cross sections are based on empirical models and semiempirical parameterizations [4].

The user defines geometry in OLTARIS as either slab thickness for each of the shielding material in a stack, as spherical shells of material distributions, or by creating vehicle thickness distributions from CAD applications. Ray tracing creates the thickness distributions by starting from a central point inside the vehicle, usually within a person, and tracing the rays outwards through the different layers of shielding. Thus a ray starts by passing through a thickness of tissue, air, shielding materials, and eventually the spacecraft hull. A user can use any number of rays from 42 to 10,000 as long as the rays represent close to equal solid angle representation of the shielding. A human phantom is available for placing within the structure to represent whole body dose based on astronaut orientation within the craft [4].

OLTARIS creates boundary flux conditions for particles based on the mission definition and chosen space radiation environment models, including Badhwar-O'Neill or Matthia for GCR, AP-8 and AE-8 for trapped radiation, and several historical SPE events. Then OLTARIS transports radiation from the boundary condition using HZETRN2005 through the geometry either as a slab computing fluxes or fluence at material boundaries or as thickness distributions for an array of depths in the user-selected materials. From the end boundary fluxes, the response function module calculates totals for scored quantities in each layer and for thickness distributions integrates the total quantity over all the rays for a total quantity. OLTARIS calculates differential flux, dose in several different target materials, TLD-100 dose, LET in several materials, and effective dose for astronauts by combining from the thickness distributions with a human phantom the dose tallies with a weighting factor. All data are then outputted through the website for user analysis [4].

CHAPTER 4

DEVELOPMENT OF A HIGH-PERFORMANCE COMPUTING SPACE ENVIRONMENT MODELING APPLICATION IN GEANT4

This chapter describes a newly developed high-performance GEANT4-based application to model space radiation interactions through a spacecraft. As described in the previous chapter, current tools are designed as a sequential code requiring extensive postprocessing to combine smaller runs. In order to develop a model in GEANT4, it is required to develop and combine several mandatory classes that describe the geometry, physics processes, particles creation, and scoring. Figure 4.1 shows the steps in GEANT4 to create simulations of a spacecraft in the space radiation environment. Each of the steps are described in an individual section, including the development of a new GEANT4 application.

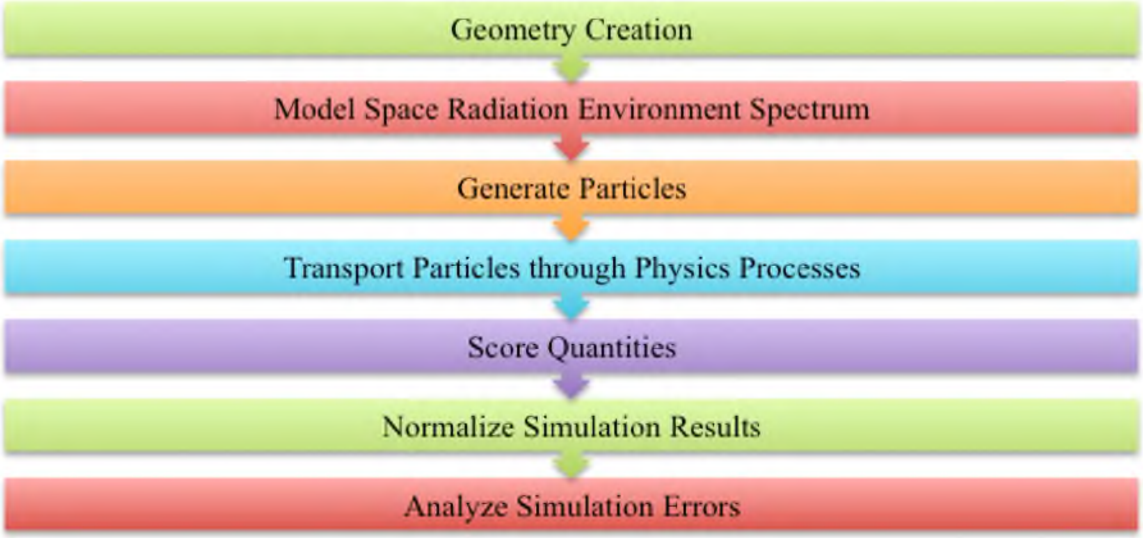

Figure 4.1: GEANT4-based process of modeling space radiation environment through a spacecraft to predict astronaut dose.

4.1 Geometry Creation

Models of geometry in GEANT4 are created as Constructive Solid Geometry (CSG) or as Boundary Representations (BREP) by using basic shapes to create a solid volume. Available solids include box, cylindrical section, conical section, parallelepiped, trapezoid, sphere, torus, polycones, ellipsoidal, tetrahedral, extruded polygon, or tessellated solid. Solids may be combined using Boolean operations to form complex shapes. Geometries may be defined by hardcoded C++ definition in the detector construction class or defined by using Geometry Description Mark-Up Language (GDML) [66].

GDML is an extension of XML language, which uses tags to describe various components. GEANT4 integrates a GDML parser that reads and writes GDML files, which can also be read from the CERN ROOT analysis package. GDML supports the basic GEANT4 solid shapes, Boolean operations of volumes, replicated volumes, and basic mathematical operations. A geometry volume is described by four attributes: the solid, the material, the logic volume, and the physical volume. All volumes are placed within the world volume, which is the outer extent of the geometry model. Attaching a solid volume with a material creates a logic volume, which is then placed inside another logic volume with position and rotation to form a physics volume, thus creating a hierarchal geometry structure of mother volumes and daughter volumes. For example, for the Apollo Command Module, the GDML creates a world volume and within it is placed the command module centered within the volume and rotated upwards, see Appendix A for complete examples [67].

A XML Schema Definition (XSD) file declares available legal elements, tags, and rules, which must be declared first in the file. The GDML XSD defines the following element blocks: <define>…</define> block declares constants, positions, and rotation; <materials>…</materials> block declares materials as either elements, mixtures, isotopes, or compounds; <solids>…</solids> block declares the solid shapes, replicated volumes, and Boolean operations; <structure>...</structure> block defines the geometry tree with logical volumes and physics volumes along with placement and rotation within the geometry; and <setup>…</setup> block defines the top volume. On runtime, the GDML parser based on the SAX parser XML engine verifies the file against the schema and creates a physical representation of the geometry in memory. The GDML parser can also output hardcode geometry as a GDML. The GDML Parser in GEANT4 is C++ based, whereas the GDML Parser in ROOT is Python based on PyROOT [67].

GDML offers the unique ability to load a geometry file on runtime, thus the developed application uses GDML geometry definition. The application implements the GDML parser through the SpaceDetectorConstruction class and its messenger class. The class contains methods for parsing the geometry file, setting the read and write file, and a ConstructSDandField method required in multithread GEANT4. Before initialization, the SetReadFile messenger class sets the geometry file, which is read on initialization with one copy of the geometry per node. Then a copy of the ConstructSDandField method is created for each thread by parsing the file for scoring sensitive detectors by using the auxiliary information tag with SensDet type, as shown below.

```
<auxiliary auxtype=”SensDet” auxvalue=”ICRU13”/>
```

To create a geometry file, the spacecraft or detector geometry is decomposed into small segment shapes with complex shapes created by Boolean operations. The following explains the creation of part of the Apollo Command Module geometry, see Appendix A for complete example. The file starts by declaring the XML version and GDML XSD schema location. Next the define block declares constants, positions, and references.

```
<define>
   <position name=”CM_Central_Position” unit=”cm” x=”0” y=”0” z=”-120.65”/>
</define>
```

By placing the positions and references in the define block, alterations to locations within the spacecraft or detector are significantly easier then looking for hard-coded blocks within code. After the define block, the materials block defines all elements used in the geometry, followed by the definition of materials, compounds, and isotopes from the elements, as shown below for hydrogen and aluminum.

```
<materials>
   <element Z=”1” formula=”H” name=”Hydrogen”>
      <atom value=”1.00794”/>
   </element>
   <material Z=”13” formula=” ” name=”Aluminum”>
      <D value=”2.70”/>
      <atom value=”26.98”/>
   </material>
</materials>
```

Then the solid block defines all the geometrical shapes used within the geometry, followed by the structures block defining the geometrical hierarchy. All objects are first declared as solids, then placed in a logic volume with material. Each physics volume is then placed within the surrounding physics volume until eventually reaching the highest level, which is placed within the world volume, as shown for the Apollo Command Module below. First the GDML creates a universe box of ten meters cubed, followed by the polycone structure of the central Apollo Command Module heat shield. Then within the structures block, the logic and physics volumes are constructed and placed within the Universe volume.

```
<solids>
     <!--Create solid shapes.-->
   <box name=”UniverseBox” lunit=”m” x=”10” y=”10” z=”10”/>
 <!--Central Heat Shield and Structure -->
```

```
 <polycone name=”Central_Heat_Shield” startphi=”␣0” deltaphi=”360” aunit=”degree
     ” lunit=”cm”>
     <zplane z=”0” rmax=”195.58” rmin=”0”/>
     <zplane z=”177.8” rmax=”99.07” rmin=”0”/>
     <zplane z=”178” rmax=”57.15” rmin=”0”/>
     <zplane z=”241.3” rmax=”45.73” rmin=”0”/> </polycone>
</solids>
<structure>
     <!--Create physics universe volume and place inside substructers.-->
<volume name=”LV_Universe”>
   <materialref ref=”Vacuum”/>
   <solidref ref=”UniverseBox”/>
      <physvol>
        <volumeref ref=”LV_Central_Heat_Shield”/>
        <positionref ref=”CM_Central_Position”/>
      </physvol>
      </volume>
 </structure>
```

After completion of geometry file, all geometries are checked for overlaps using the GEANT4 check overlaps function or by using the DAWN visualization package in conjunction with the DAVID application to identify any geometry overlaps. Any volume that overlaps another volume or daughter volume that exceeds the mother volume causes stuck particles on execution and must be corrected.

4.2 Model Space Radiation Environment Spectrum

The SPENVIS information system created the input spectra files for simulations. To create accurate models of the radiation environment, SPENVIS requires mission time period and precise trajectory data, since a small change in location results in a big difference in trapped radiation belt flux. SPENVIS used two-line elements and trajectories paths to accurately generate ephemeris data and create spectra for each mission period based on the selected models in the Radiation and Sources Module within SPENVIS, see Chapters 5 and 6 for details for the ISS and Apollo missions. Then SPENVIS's GEANT4 Tools Definition of Source Particle module created input spectrum files for the radiation environment, one macro file per particle type. Since GRAS, MULASSIS, and SPENVIS implement a spectrum file for each radiation environment with an accompanying source definition macro, the same methodology was used to create two macro files for runtime [12].

4.3 Generating Radiation Particles

GEANT4 contains two methods of creating particles either using the particle gun or the General Particle Source (GPS). The GPS creates particles of various types, including ions, radioactive isotopes, protons, electrons, muons, pions, and other subatomic particles of varying energy, by using macro files at runtime. The user selects the energy as a monoenergetic distribution, a linear energy distribution, power law distribution, exponential distribution, or an energy spectrum given by histogram points of energy and differential flux shown in Table 4.1 with the particle's created

Table 4.1: Possible energy distribution within GPS, with the particle's energy y, initial energy E_0, and constants a, B, and α.

Distribution	Mathmatical Model
Mono-Energetic	$y = E_0$
Linear Distribution	$y = aE + B$
Power Law Distribution	$y = aE^{\alpha}$
Exponential Distribution	$y = Ae^{E/E_0}$
Energy Spectrum	

energy y, initial energy E_0, and constants a, B, and α. The GPS default energy unit is MeV with default energy of 100 MeV and intensity of one particle/cm^{2}s [68].

The application uses the GPS since it was initially designed specifically for space applications and because of the flexibility of particle creation, energy, source type, and position by macro file [69]. The GPS can create a source as a point, beam, plane, surface, or volume source as a sphere, ellipsoid, cylinder, or paraboloid surface or volume. The source can have angular distribution of isotropic, cosine-law, planar-wave, accelerator beam focused to a point, or user-defined. The particle generation is created using two macro files for the application. The gps.mac file defines the source type as a spherical surface, sets the radius, sets the location in Cartesian coordinates, and sets the surface area for normalization, see Appendix B for an example. The application used a spherical surface source bigger than the spacecraft volume that easily replicates the isotropic space radiation. Then a particle file from SPENVIS defines the particle type from proton, neutron, electron, to HZE particle along with a biased energy spectrum defining the flux. Since the energy spectrum for space is vast, energy biasing increases the probability of low and high energy particles being generated improving statistics with less particles [12,69]. The particle file defines the source with a cosine law distribution to accurately create an isotropic surface source, since an isotropic source on spherical surface source creates a biased distribution [12, 70]. SPENVIS generates within the particle file a spectrum and angular normalization factor to normalize the radiation flux.

4.4 Transporting Particles through Physics Processes

Creating an accurate model of radiation transport through a spacecraft requires accurate models of all applicable physics interactions for charged particles, neutrons, and electromagnetic interactions; otherwise, the computations may result in low statistical errors yet have inaccurate results for the actual dose and energy deposition. GEANT4 contains seven major categories of particle interactions processes to model radiation transport, including: electromagnetic, hadronic, transportation, decay, optical, photo-lepton-hadron, and parameterization [71].

The application developer selects physics processes by the mandatory user class within the code of G4VUserPhysicsList or by GEANT4 prepackaged physics lists. The G4VUserPhysicsList allows developers to pick and choose the interactions and transportation processes for greater speed in simulation; however, developers can miss needed processes or create issues with physics process delegation to threads in multithread applications. Therefore, the GEANT4 collaboration now recommends the use of prepackaged physics lists, which provide developers a choice of already built and tested lists of processes that include all needed interactions [71].

In the GEANT4 physics engine, each particle is transported through the physics processes at three points: "At Rest Do It", "Along Step Do It", and "Post Step Do It" [49]. Each particle is then tracked through the geometry, undergoing the given processes at the three points. For example, at rest the particle would undergo radioactive decay, along step photons would undergo photoelectric effect or Compton scattering, and poststep the particle energy loss would be computed.

GEANT4's electromagnetic processes contain many different interactions besides the main ways ionizing photons interact with matter, such as Photo-electric effect, Compton Scattering, and Pair Production. Table 4.2 shows the basic possible electromagnetic physics processes for each particle, with the corresponding GEANT4 class [71]. The three main photon interactions with matter are photoelectric effect, pair production, and Compton Scattering. In the photoelectric effect, a photon strikes an electron in an atom with energy greater then the binding energy, thus emitting the electron as a photoelectron. The free photoelectron then has the energy of the photon minus the work energy of the metal, which is the binding energy of the electron. The energy of emitted photoelectron E_e is dependent on the incoming energy of the photon f, Planck's constant h, and the work energy W for the metal:

$$hf = E_e + W \tag{4.1}$$

In pair production a photon above 1.022 MeV in the electric field of a heavy nucleus becomes an electron/positron pair. The positron will travel a short distance until annihilating with another electron, creating two photons of .511 MeV.

$$\gamma \rightarrow e^{+} + e^{-} \tag{4.2}$$

In Compton scattering, a charged particle such as an electron inelastically scatters an incoming photon, transferring some of the energy to the photon, thus the photon loses energy increasing in wavelength [72]. Equation 4.3 shows the Compton shift in photon wavelength λ, where h is Planck's constant, m_e is the mass of the electron, c is the speed of light, and θ is the scattering angle.

$$\lambda' - \lambda = \frac{h}{m_e c}(1 - \cos\theta) \tag{4.3}$$

In GEANT4, these processes and others shown in Table 4.2 are contained in different combinations as prepackaged electromagnetic process lists with a default list of G4EmStandard Physics.

Table 4.2: Complete list of GEANT4 physics processes for electromagnetic interactions with different particles [73].

Particle	Physics Processes	GEANT4 Class
Photon	Gamma Conversion	G4GammaConversion
	Photo-electric Effect	G4PhotoElectricEffect
	Compton Scattering	G4ComptonScattering
	Rayleigh Scattering	G4RayleighScattering
	Pair Production	G4GammaConversionToMuons
Electron/Positron	Ionisation and Delta Ray Production	G4eIonisation
	Bremsstrahlung	G4eBremsstrahlung
	Multiple Scattering	G4eMultiple Scattering
	Positron Annihilation into Two Gammas	G4eplusAnnin
	Positron Annihilation into Two Muons	G4AnnihiToMuPair
	Positron Annihilation into Hadrons	G4eeToHadrons
Muon Processes	Ionisation and Delta Ray Production	G4MuIonisation
	Bremsstrahlung	G4MuBremsstrahlung
	e+ e- Pair Production	G4MuPairProduction
	Multiple Scattering	G4MuMultipleScattering
Hadron/Ion Processes	Ionisation	G4hIonisation
	Ionisation for Ions	G4ionIonisation
	Ionisation for Heavy Exotic Particles	G4hhIonisation
	Ionisation for Magnetic Monopole	G4mplIonisation
	Multiple Scattering	G4hMultipleScattering
	Bremsstrahlung	G4hBremsstrahlung
	e+ e- Pair Production	G4hPairProduction
Charged Particles	Coulomb Scattering	G4CoulombScattering or G4ScreenedNuclearRecoil
Polarized Electrons and Gamma Beams	Compton Scattering of Polarized Gamma Beam	G4PolarizedCompton
	Pair Production by Polarized Gamma Beam	G4PolarizedGammaConversion
	Photo-electric by Polarized Gamma Beam	G4PolarizedPhotoElectricEffect
	Bremsstrahlung of Polarized Electrons and Positrons	G4ePolarizedBremsstrahlung
	Ionisation of Polarized Electron and Positron Beam	G4ePolarizedIonisation
	Annihilation of Polarized Positrons	G4eplusPolarizedAnnihilation
X-rays and Optical Photons	Synchrotron Radiation	G4SynchrotronRadiation
	Transition Radiation	G4TransitionRadiation
	Cerenkov Radiation	G4Cerenkov
	Scintillations	G4Scintillation

The standard electromagnetic physics list has four additional options. Option one is faster because of simplified step limitation for multiple scattering and ionisation; however, the electron transport is not as accurate. Option two applies experimental electromagnetic data to simulations with disabled "ApplyCuts." Option three is the most accurate but slowest do to alternative more precise models of Compton scattering, Rayleigh scattering, and multiple scattering step limitation [71]. Also three other lists of note for simulations are G4EmLivermorePhysics based on experimental data sets from Livermore National Labs, G4EmDNAPhysics for low-energy studies of DNA microdosimetry, and G4EmPenelopePhysics based on the low-energy Penelope2008 models for electrons, positrons, and gammas [74].

Particles interact with matter by elastic scattering, inelastic scattering, fission, charged particle emission, and radiative capture. Elastic scattering occurs when a proton, neutron, alpha particle, or HZE ion collide with an atom, imparting some energy to the atom. In the collision of the particle and atom, the momentum and the total kinetic energy are conserved between the two. Elastic scattering is the main mechanism for particle energy loss and stopping in radiation shielding materials, and the particles will undergo many interactions along the path to slow down, especially for high-energy particles. Additionally, a neutron may elastically scatter by potential elastic scattering or resonance elastic scattering. In potential elastic scattering the neutron is scattered by the short-range strong nuclear force. In resonance elastic scattering, the neutron is absorbed by the target nucleus, forming a compound nucleus, which immediately reemits the neutron. For example, a neutron in resonance elastic scattering with an oxygen atom creates an excited oxygen-17 compound nucleus, which decays back into a neutron and oxygen as shown:

$$n + {}^{16}_{8}O \rightarrow {}^{17}_{8}O^{*} \rightarrow n + {}^{16}_{8}O \tag{4.4}$$

If the collision between the particle and nucleus does not conserve kinetic energy, the collision is inelastic. Inelastic scattering occurs at specific energies usually for electrons, photons, neutrons, or hadrons. In neutron inelastic scattering, the incoming neutron is captured in the nucleus followed by emitting energy to de-excite the atom, which reduces the total kinetic energy. In order for the neutron or other particle to be captured and scattered inelastically, the neutron or particle energy must match one of the higher excited states for nucleons in the nucleus. For example, a neutron n, collides with an atom X, atomic number Z, and mass number A will create a compound nucleus X^{*}. The compound nucleus will then emit a neutron, losing some of the total kinetic energy as a gamma ray. The gamma ray de-excites the nucleus.

$$n + {}^{A}_{Z}X \rightarrow {}^{A+1}_{Z}X^{*} \rightarrow n + {}^{A}_{Z}X + \gamma \tag{4.5}$$

If the nucleus absorbs the neutron without reemission of a neutron, the process is called radiative capture as shown:

$$n + {}^{A}_{Z}X \rightarrow {}^{A+1}_{Z}X^{*} \rightarrow {}^{A+1}_{Z}X + \gamma \tag{4.6}$$

In charged particle emission, the compound nucleus decays by emitting either a proton p or alpha particle α to loss energy, as shown in the following two equations.

$$n + {}^{A}_{Z}X \rightarrow {}^{A+1}_{Z}X^{*} \rightarrow p + {}^{A}_{Z-1}X + \gamma \tag{4.7}$$

$$n + {}^{A}_{Z}X \rightarrow {}^{A+1}_{Z}X^{*} \rightarrow \alpha + {}^{A-3}_{Z-2}X + \gamma \tag{4.8}$$

Neutrons may also cause heavy atoms to split through fission. If the neutron adds enough energy beyond a critical energy to the nucleus to elongate the spherical nucleus, the charge in the nucleus becomes asymmetric, causing two differently sized lobes to form. The electrostatic repulsion between the lobes causes the atom to split into two smaller nuclei ${}^{A_1}_{Z_1}X$ and ${}^{A_2}_{Z_2}X$ of different sizes, as shown [72]:

$$n + {}^{A}_{Z}X \rightarrow {}^{A+1}_{Z}X^{*} \rightarrow {}^{A_1}_{Z_1}X + {}^{A_2}_{Z_2}X \tag{4.9}$$

These particle interactions with matter in GEANT4 are modeled using cross section data sets for low-energy particles and theoretical atomic models for high-energy particles. Figure 4.2 shows the models used for each energy range. GEANT4 contains multiple models for each energy range, depending on the application. For high-energy particle collisions above 20 GeV, GEANT4 uses either the Quark-Gluon String (QGS) model or the Fritiof (FTF) string model for theoretical hadron-hadron and hadron-nucleus interactions. Both models describe hadron and nuclear elastic and inelastic scattering at high energies, along with secondaries production [75]. At energies below 10 GeV, GEANT4 uses one of two cascade models: Bertini or Binary cascade model. The Binary cascade model is more theoretical; however, both equally simulate initial hadron and nuclear interaction, creating secondaries with an excited nucleus. Next, GEANT4 applies an evaporation routine of either a precompound model or a Bertini cascade to de-excite the remaining nucleus. The Chiral Invariant Phase space (CHIPS) model reabsorbs remaining slow-moving particles into the nucleus. The cross sections contain data on inelastic scattering, elastic scattering, fission, and radiative capture that originated from the GHEISHA hadronic fortran code [76].

For neutrons below 20 MeV, GEANT4 uses the optional high-precision neutron process based on data sets from ENDF/B-VI. Older hadronic processes used Low Energy Parameterized (LEP) and High Energy Parameterized (HEP) models originally from GHEISHA for long-lived particles that fitted theoretical models with experimental data, which has been removed in current GEANT4.10.0

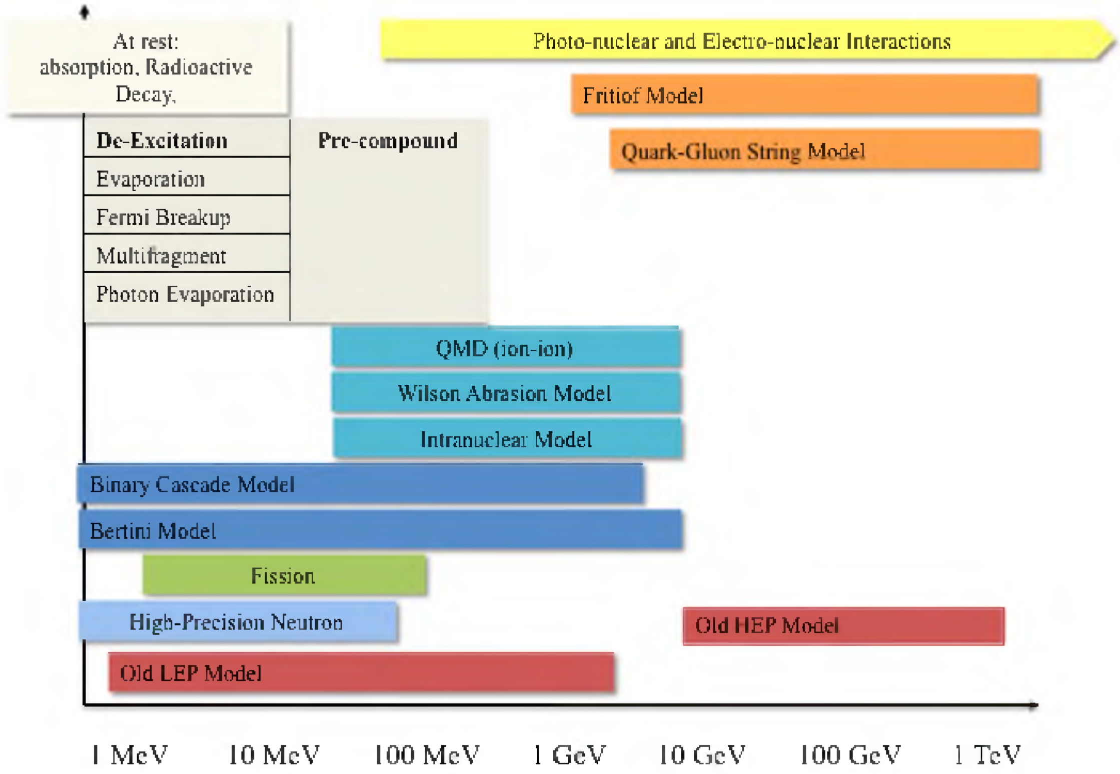

Figure 4.2: Physics models by interactions in GEANT4 versus energy. Several models overlap for different energy ranges such as Binary Cascade Model and Bertini Model or Fritiof and Quark-Gluon String Model [73].

[71,73]. Figure 4.2 shows physics processes for a given energy range, notice several different models fit each energy range. Detailed information about each model and process is found in the GEANT4 Physics Reference Manual [73].

Each prepackaged physics lists include different combinations of these models to describe interactions across all energy ranges of interest. GEANT4.10 contains fewer physics lists than previous versions, with several older versions being removed such as CHIPS packages and LHEP models [73]. The prepackaged lists can use six different optional electromagnetic physics lists by using the G4PhysListFactory with an argument: option 1 (_EMV), option 2 (_EMX), option 3 (_EMY), option 4 (EMZ), G4EmLivermorePhysics (_LIV), and G4EmPenelopePhysics (_PEN). On runtime, GEANT4 outputs the physics list name used, list of processes, and energy range of each process. Table 4.3 shows the available physics lists in GEANT4.10 with a short description.

FTFP_BERT model uses FTF model for energies above 4 Gev and Bertini cascade model for hadrons below 5 GeV, used by HEP detector at CERN [78]. FTFP_BERT_HP is the same as

Table 4.3: Available pre-packaged physics lists in GEANT4.10 with descriptions [77].

Pre-Packaged List	Description
FTF_BIC	Fritiof Binary Cascade
FTFP_BERT_HP	Fritiof-Bertini Model w/ High Precision Neutron
FTFP_BERT_TRV	Fritiof-Bertini Model changing Inelastic Thresholds
FTFP_BERT	Fritiof-Bertini Model (String Model)
FTFP_INCLXX	Fritiof-Bertini Model and Intranuclear Cascade
FTFP_INCLXX_HP	Fritiof-Bertini Model and Intranuclear Cascade w/ High Precision Neutron
LBE	Low Background Experiment w/ High Precision Neutron
QBBC	Combination BIC, BIC-Ion, BERT, CHIPS, QGSP and FTFP models
QGS_BIC	Quark Gluon and Binary Cascade from QGSP_BIC
QGSP_BERT_HP	Quark Gluon and Bertini Model w/ High Precision Neutron
QGSP_BERT	Quark Gluon and Bertini Model Cascade
QGSP_BIC_HP	Quark Gluon and Binary Cascade w/ High Precision Neutron
QGSP_BIC	Quark Gluon and Binary Cascade
QGSP_FTFP_BERT	Quark Gluon, Fritiof, and Bertini Model
QGSP_INCLXX_HP	Quark Gluon and Intranuclear Cascade w/ High Precision Neutron
Shielding	Used for neutron penetration and ion-ion collisions.

FTFP_BERT with the high-precision neutron cross section libraries for neutrons below 20 MeV, which slows down the simulation time. The shielding physics list is based on FTFP_BERT_HP with neutron cross sections from JENDL and heavy ion interactions from Quantum Molecular Dynamics (QMD) model [79].

QGSP_BERT uses the Bertini model up to 9.5 GeV, the Fritiof model between 9.5-25 GeV, and the QGS model for higher energies above 20 GeV. The QGSP_BIC model is similar to QGSP_BERT using quark-gluon string theory to model high-energy particles, but uses Binary Cascade models and G4Precompound model at lower energies. The QGSP_BIC_HP is the same as QGSP_BIC with high-precision neutron cross-section libraries below 10 GeV. The proceeding physics lists use the EMStandardPhysics list for electromagnetic physics. [76]

The QBBC physics list uses the BIC, BIC-Ion, BERT, QGSP, and FTFP models for higher precision in hadron-ion and ion-ion interactions [80]. Vladimir Ivanchenko developed QBBC for space applications, radiation biology, and radiation protection. Chavy-Macdonald et al. used the QBBC physics list for simulations of the ISS within GRAS due to improved performance in space applications [81]. The DESIRE study used the older LHEP_BIC_HP [82–84], which has been replaced with the QGSP_BIC_HP model.

For modeling space applications, four potential physics list were chosen: QGSP_BERT_HP, QGSP_BIC_HP, Shielding, and QBBC selectable on runtime as a command line argument. The HP (High Precision) versions were selected, since they accurately model neutron transport from 10GeV down to thermal range, whereas the defaults do not. All four lists contain needed interactions for the energy range and are recommended for space and shielding applications. Apostolakis et al. suggest that the QGSP_BERT_HP list is slower than QGSP_BIC_HP [76]. According to spallation data in space energy range of up to 100 GeV, the QGSP_BIC better matches experimental data for low-energy protons and neutrons, whereas QGSP_BERT better matches higher energy collisions [80]. Thus QBBC should better match data due to the combination of low-energy BIC models, mid-energy BERT models, and high-energy QGSP and FTFP models. Both BERT and BIC models match computational results for proton fluxes through an aluminum target from CREME96 [20].

QGSP_BERT_HP and QGSP_BIC_HP contain G4DecayPhysics for decay interactions; however, they do not include radioactive decay processes. Thus the G4RadioactiveDecayPhysics list was added for computation of decay of radioactive isotopes, which were temporarily disabled in GEANT4 10.0.0-10.0.2 due to a bug in GEANT4 data libraries. QBBC and Shielding physics list already contain radioactive decay physics.

4.5 Score Quantities

The toolkit silently transports particles, thus requiring the user to implement one of three scoring methods: command-based scoring using a scoring mesh, sensitive detector to register hits, or a user-defined scorer. The command-based scorer uses a scoring mesh as a series of boxes or cylinders to which any of the primitive scorers can be attached. Primitive scorers are basic scorers within GEANT4 for energy deposition, dose, track length, flux, or current. The sensitive detector can be used with a hits collection or the multifunctional detector and primitive scores. The Construct Sensitive Detector and Field method attaches the sensitive detector to a geometry logic volume to score particles within the given volume. The event-based scorer allows users to record any physics quantity, including entire tracks; however, it requires users to program their own data-writing methods and can create very large data sets when recording large number of particles [77].

The command-based scoring creates a parallel world in the geometry with a three-dimensional mesh to record physics quantitates using the primitive scorers. The user defines by command line or macro file the scoring mesh as a box by specifying half width of the box in x, y, and z along with the number of bins along each axis. The mesh may be rotated and placed anywhere within the geometry by command line. The scorer may score multiple quantities with one filter per scorer. The scorer dumps quantities out individually as a single file in CSV format or in custom format [77].

The scoring mesh and sensitive detector may use any of the GEANT4 primitive scorers, including track length, energy deposit, dose deposit, current, flux, cell flux, the minimum kinetic energy of secondary particle at generation, number of secondaries, number of particles steps within cell, and total charge of particles stopped in volume; however, GEANT4 does not contain any built-in scorers for equivalent dose. Each scorer may use one filter, including charged particle filter, neutral particle filter, particle species filter, kinetic energy filter, and a particle with kinetic energy filter.

The application implemented the command-based scorer and multifunctional detector, which registers a primitive scorer to the sensitive detector. Any of the primitive scorers may be implemented with the application by changing the scorer in the Detector Construction class; currently implemented are an energy deposit scorer, dose deposit scorer, and three new equivalent dose scorers based on ICRP 60, 92, and 103 reports. The new equivalent dose scorers consist of three new function files with associated headers. Each scorer file modeled after the GEANT4 dose scorer and GRAS equivalent dose scorer implements three required virtual methods: initialize method invoked at beginning of event, end of event method invoked at end of each event, and process hits method. In the process hits class, the method calculates the dose by finding the energy deposited divided by the mass as the dose scorer, then it gets the particle name and kinetic energy to calculate the particle-weighting factor. The particle-weighting factor is calculated following the method outlined earlier in Table 2.2. The process hits method then calculates the equivalent dose by multiplying the dose by particle-weighting factor.

4.6 Normalizing Scored Simulation Results to Real World

The number of particles in a simulation does not match the real number of particles passing through the volume in space. Thus each scored quantity must be multiplied by a normalization factor to normalize the data. The real scored value X_r is equal to the scored quantity X_s multiplyed by the real number of particles within the geometry N_r divided by the number of particles in the simulation N_s [85].

$$X_r = X_S \frac{N_r}{N_s} \tag{4.10}$$

The Normalization factor N_r shown in equation 4.11 is dependent on the number of particles within a given energy range n_1 (energy spectrum normalization factor), the angular distribution of the particles from the source n_2 (angular normalization factor), and the surface area of the source S.

$$N_r = n_1 n_2 S \tag{4.11}$$

The energy spectrum normalization factor is the number of particles from the source passing through the geometry within a given energy range. If the source is monoenergetic, the normalization factor is equal to the flux. For linear, power law, and exponential energy distributions, the normalization factor is dependent on the minimum and maximum energy E along with the constants A and B given to the GPS energy distribution as shown in Table 4.4. For an energy spectrum, the normalization factor is the minimum integral fluence minus the maximum integral fluence [12].

Table 4.4: Energy normalization factor for each energy distribution giving the number of real world particles within each energy distribution.

Energy Distribution	Normalization Factor
Mono-energetic	$n_1 = I\left(E_0\right)$
Linear	$n_1 = \left[\frac{A}{2}E^2 + BE\right]_{E_{\text{min}}}^{E_{\text{max}}}$
Power Law	$n_1 = \left[\frac{A}{\alpha+1}E^{\alpha+1}\right]_{E_{\text{min}}}^{E_{\text{max}}}$
Exponential	$n_1 = \left[-AE_0 e^{-\frac{E}{E_0}}\right]_{E_{\text{min}}}^{E_{\text{max}}}$
Energy Spectrum	$n_1 = \left(F\rvert_{E_{\text{min}}}^{\infty} - F\rvert_{E_{\text{max}}}^{\infty}\right)$

The angular distribution factor describes the directional distribution of particles from the source. For a Monte Carlo simulation with a spherical surface source, particles pass inwards from the surface; therefore, the angular distribution factor is dependent on current through the source instead of surface flux when normalizing results, see Chapter 2 for detailed description of current, flux, and fluence. Since radiation passing through space is uniform, equation 4.12 derives the isotropic fluence $\phi_{4\pi}$ from the spatial fluence $\phi(T, \theta, \omega)$ with solid angle (azimuthal) ω, oblique angle θ, and kinetic energy T in units of particles/(MeV cm^2 sr) by integrating over the solid angle 0 to 2π and oblique angle -1 to 1:

$$\phi_{4\pi}\left(T\right) = \int\limits_{0}^{2\pi} d\omega \int\limits_{-1}^{1} \phi\left(T\right) d\left(\cos\theta\right) = 4\pi\phi\left(T\right) \tag{4.12}$$

The total current $j\left(T\right)$ through the surface source crossing into the spacecraft follows a cosine law distribution.

$$j\left(T\right) = \int\limits_{0}^{2\pi} d\omega \int\limits_{0}^{1} \phi\left(T\right)\cos\theta d\theta = \pi\phi\left(T\right) \tag{4.13}$$

Since the current given by equation 4.13 is ¼ the isotropic fluence given by equation 4.12, the current through the spherical surface source is ¼ the integrated isotropic flux [86].

$$j\left(T\right) = \frac{1}{4}\phi_{4\pi}\left(T\right) \tag{4.14}$$

If the cosine source is reduced from 0 to 2π to a smaller angle to improve the number of particles passing through the area of interest, the angular distribution factor is multiplied by the sine of the angle shown in Table 4.5. For a point source similarly to a Cosine Law distributed source, the particle fluence is assumed to be omnidirectional. Thus the fluence is integrated over the solid angle 0 to 2π.

Table 4.5: Angular distribution normalization factors for GPS particle direction biasing.

Angular distribution	Normalization factor
Cosine Law Biasing	$n_2 = \frac{1}{4\pi}\int_0^{2\pi} d\phi \int_{\theta_{\min}}^{\theta_{\max}} \cos\theta \sin\theta d\theta = \frac{1}{4}\left(\sin^2\theta_{\max} - \sin^2\theta_{\min}\right)$
Point Source	$n_2 = \frac{1}{4\pi}\int_0^{2\pi} d\phi \int_{\theta_{\min}}^{\theta_{\max}} \sin\theta d\theta = \frac{1}{2}\left(\cos\theta_{\min} - \cos\theta_{\max}\right)$
Parallel beam	$n_2 = 1$

If the source is not directionally integrated with a solid angle, i.e., in the units of steradians, there is no need to divide by 4π. For a parallel beam, the particles are parallel, thus the angular distribution is equal across the entire beam.

For example, assuming a source with fluence F in particles/cm^{2}sr, spherical source with surface area S and radius R, Cosine Law distribution from 0 to 2π, and number of simulated particles N_s, the normalization factor would be given by using equation 4.11 combined with the energy distribution equation 4.15 and the angular distribution equation 4.16.

$$n_1 = \left(F|_{E_{\min}}^{\infty} - F|_{E_{\max}}^{\infty}\right) = F - 0 = F \tag{4.15}$$

$$n_2 = \frac{1}{4\pi}\int_0^{2\pi} d\phi \int_0^{\pi/2} \cos\theta \sin\theta d\theta = \frac{1}{4} \tag{4.16}$$

The surface area of a spherical source is calculated by:

$$S = 4\pi R^2 \tag{4.17}$$

Thus the normalization factor N_r is given by:

$$N_r = n_1 n_2 S = F\pi R^2 \tag{4.18}$$

Combining the previous three equations, the real dose D_r is given from the scored dose D_s in the simulation by:

$$D_r = D_s\frac{N_r}{N_s} = D_s\frac{F\pi R^2}{N_s} \tag{4.19}$$

4.7 Simulation Errors

Precision in a Monte Carlo simulation gives a measurement of how close the simulated data is to the mean scored value, usually measured as the standard deviation and relative error of the data. In GEANT4, most applications measure the root mean square (RMS) error as a measurement of precision. As the number of iterations increases, the standard deviation decreases, giving a more precise simulation; however, the precision of Monte Carlo simulation may not reflect the actual truth (accuracy) if the problem parameters do not match realistically. The accuracy is how close a measurement matches up to the real value. A measurement may be precise but not necessarily accurate, as that measurement can be far from the actual number. For example, in radiation measurement a longer count might give a higher peak thus better precision; however, the measurement of that peak can be far from the actual real energy value. Similarly in Monte Carlo Simulations a result may have good statistical significance with low error, but the results maybe far from the real value. Thus models should be verified with experimental results [7].

In a simulation, the total $\bar{x}$ for any tally (average) is given by equation 4.20, which sums up all the individual results x over the interval of i=1 to N divided by the number of particles N:

$$\bar{x} = \frac{1}{N}\sum_{i=1}^{N} x_i \tag{4.20}$$

The standard deviation of the results is then calculated by finding the difference between the tally total and each point squared given by

$$S^2 = \frac{\sum\limits_{i=1}^{N} (x_i - \bar{x})^2}{N-1} = \bar{x^2} - \bar{x}^2 \tag{4.21}$$

which can be simplified in terms of the difference between the tally total squared and the average of the square of each result given by

$$\bar{x^2} = \frac{1}{N}\sum_{i=1}^{N} {x_i}^2 \tag{4.22}$$

The variance of the results given by Sx is calculated by the square of the standard deviation divided by the number of tallies N, as shown:

$${S_{\bar{x}}}^2 = \frac{S^2}{N} \tag{4.23}$$

The relative error in a calculation for a tally is given by the variance divided by the tally:

$$R \equiv \frac{S_{\bar{x}}}{\bar{x}} = \left[\frac{\sum_{i=1}^{N} {x_i}^2}{\left(\sum_{i=1}^{N} x_i\right)^2} - \frac{1}{N}\right]^{1/2} \tag{4.24}$$

The lower the error, the more reliable the results, with error below 10% being reasonable. See Table 4.6, which shows the reliability of a tally based on the relative error [7]. When the relative error is above 10%, the variation across the tally is so large that statistically the result is unreliable since the actual value can be within a very large range. As the relative error decreases, the variation in tally decreases, resulting in a smaller range for the actual value.

Table 4.6: Significance of the relative error in terms of tallies reliability. [7]

Range of Relative Error	Quality of the Tally
.5 to 1	Garbage
.2 to .5	Factor of a few
.1 to .2	Questionable
<.10	Generally reliable except for point detector
<.05	Generally reliable for point detector

Another important factor is the Figure of merit (FOM), which should remain constant over the run. If the FOM varies with time, the model is diverging instead of approaching a solution. FOM is calculated by taking the inverse of the relative error squared, R, times the computational time T:

$$FOM \equiv \frac{1}{R^2 T} \tag{4.25}$$

The Figure of merit relates the time for a relative error over computational time. After the FOM is found for a model, the relative error after a time is given by

$$R = \frac{1}{\sqrt{FOM \cdot T}} \tag{4.26}$$

which gives the error after a given computational time T. The time needed to reach a relative error R by a Figure of merit is obtained from

$$T_f = \frac{1}{R^2 FOM} \tag{4.27}$$

Since the number of particles simulated and runtime are linear and dependent, a test run with a small number of particles P_0 gives an initial runtime T_0 that is proportional to a final larger number of particles P_f and longer runtime T_f, shown in

$$\frac{P_0}{T_0} = \frac{P_f}{T_f} \tag{4.28}$$

Thus combining equation 4.27 and equation 4.28, the total number of particles needed to reach a given statistical significance is as follows:

$$P_f = \frac{T_f P_0}{T_0} = \frac{P_0}{T_0 R^2 FOM} \tag{4.29}$$

4.8 GEANT4 Multithreading and MPI

The latest version, GEANT4.10 includes new multithreading event parallelism following the POSIX standards. The developed application integrated the new G4Multithread Runmanager, which creates multiple thread-splitting events. Parallelism is achieved by all the threads equally splitting the number of events while sharing data-intensive information such as the complete geometry and physics cross sections. In order to maintain thread safety and avoid conflicting simultaneous memory access, each individual thread generates its own particle generator, event actions, step actions, and sensitive detector through a new Action Initialization class that was implemented within the code [87].

The events may be split across threads only if the pseudo random number generator (PRNG) is unique for each thread with a different random seed; however, in order to obtain reproducible data, the PRNG must result in the same sequence of random numbers independent of the number of threads from the same starting random seed. Thus GEANT4 uses a new parallel PRNG generator based on the CLHEP library by CERN to generate random numbers, with each thread being given a starting seed and each thread computing its own random number [87].

Koichi Murakami (KEK) implemented and maintains a series of MPI library for GEANT4 that uses event-level parallelism. The G4Runmanager is replaced with a G4MPIManager, and the UI session is replaced with G4MPISession. The G4MPIManager loads a full simulation into each node, and then the G4MTRunManager creates threads for each node. The G4MPISession controls simulations across the nodes sending and receiving commands. The G4MPIManager creates a unique random number seed for each node, which then each node uses to create a random seed list [88].

The application implemented multithreading and MPI by using event parallelism, breaking the total number of particles between the threads and nodes equally. A MPI master broadcasts the simulation to each node along with a unique random seed for each node. Figure 4.3 shows how the simulation is split into multiple threads by the MPI Master reading the initial geometry and creating a random seed list. Then the master sends the data to each to node, which creates one set of geometry and physics processes shared by all threads on the node. Each node then creates threads and unique random numbers per thread from the received seed list from the MPI Master. Each thread then creates its own particle generator, event action, stepping action, and sensitive detector, after which the thread initiates a run iterating an event particle loop, equally splitting the events across all nodes and threads. At the end of the event run, the thread results are merged by node, and then using MPI send and receive the master merges the results shown in Figure 4.4.

The application was first converted to multithread by implementing the G4MTRunManager in place of the G4RunManager with a build option to determine if multithreading is enabled in GEANT4. Then a function was added into the code to automatically determine the number of cores available and set the number of threads equal to the number of cores. Next the event class, primary generator, and run action classes were moved to a new action initialization class. When a simulation is started, the action initialization class generates a unique copy of the event class,

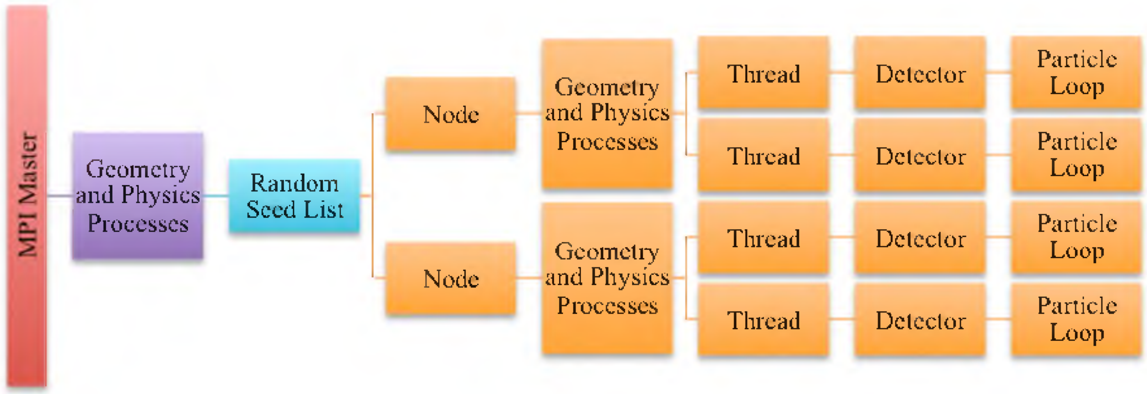

Figure 4.3: Procedure for splitting a simulation across multiple threads and nodes.

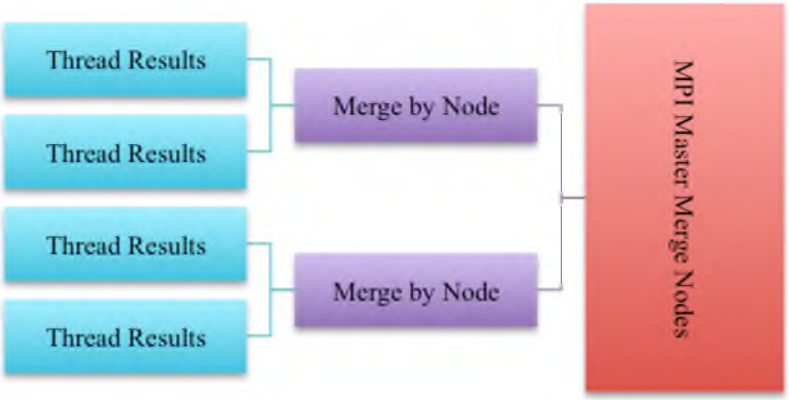

Figure 4.4: Procedure for merging results from threads back to master node.

primary generator, and run action for each thread, while sharing the physics processes and geometry. Also in the Detector Construction class, a Construct Sensitive Detector and Field class was added, implementing the sensitive detector. When the application initializes, each thread receives a copy of the sensitive detectors to store data in local memory, thus requiring an additional class be added into the run action and run classes to merge the data between threads. The merge method allocates local memory and then merges each one of the threads to the local run iterating over the number of detectors.

Converting the application to MPI required adding a new build option with flags to switch between MPI and non-MPI mode in the application and a CMake option. The CMake option for MPI finds the MPI compiler, links to the MPI Libraries and G4MPI Libraries on the cluster, and changes the build flags for MPI to on. The space application implementation is unique in that the application has been built to compile as MPI or non-MPI with the same application, allowing for easier development and cross-platform compatibility.

Next in the main space.cc application a build option flag was added, SPACE_BUILD_MPI, that, when on, adds the G4MPImanager and G4MPIsession header files to be used and when off builds using the default G4 UI. When the MPI build option is on, the application passes command arguments to the G4MPIManager instead of parsing the commands and passing to the standard G4 UI. The G4MPImanager was added to the main file along with starting the G4MPIsession manager. The G4MPImanager initializes the MPI session, gets the number of nodes, creates a master seed for each node for the number of nodes, and sends a copy of the simulation to each node using MPI send. The G4MPIManager includes functions to check status, send batch files to each node, and pass UI commands. On beamOn, the total number of events are divided by the number of nodes equally, and each node executes a beamOn, splitting the number again equally among threads. The G4MPIManager polls nodes to check for completion.

The next step required adding a merge function to the Run Action class on end of run action. Since data from the run can either be a scoring mesh or a hits map from the sensitive detector, two merging functions are required. The G4MPIRunMerger class combines the hits map from each node by sending each array of data one by one from nodes and adding to the master nodes hits map. The G4MPIScorerMerger merges scoring meshes together by iterating over each one of the mesh elements and the selected primitive scorers.

4.9 Results from Performance Testing on Ember Computer Cluster

A simulation using the Apollo Command Module with protons of 20 GeV in an isotropic spherical surface source of 7m tested the application. One million particles was chosen as being reasonable to run on one thread within a given number of time, yet large enough to test large runs. The number of particles vs. runtime was fairly linear, except the load time was a greater part of the total run time for the small number of particles shown in Figure 4.5, thus a million particles would scale similarly to larger particle run time.

Next the loading of the nodes was investigated to determine optimal loading by running a simulation for the ISS with one million particles, timing the results for five runs and averaging the times shown in Table 4.7. Using two nodes showed increased performance over a single node; however, the application may load simulations in two ways: either as one simulation per node with twelve threads or using MPI to create two simulations per node, one on each of the two processors (socket) with six threads. Typically in a high-performance computing environment creating one simulation per socket gives increased performance, since each socket has its own cache and memory. However, since each thread iterates its own event loop with minimal need to access the shared memory, loading one simulation per node instead of per socket achieved the best performance.

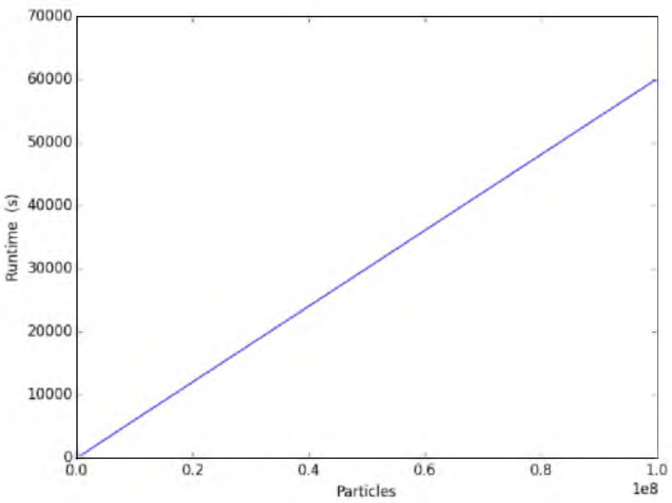

Figure 4.5: Runtime in seconds vs. number of particles for simulation of Apollo Command Module using multithread GEANT4 on Ember cluster with two 2.8 GHz Intel Xeon Westmere processors with 12 threads.

Table 4.7: Comparison of run time for varying node loading methods on Ember cluster with dual socket six core nodes of 2.8 GHz Intel Xeon Westmere processors for one million simulated particles in multithread and MPI GEANT4.

Node Loading	Real Time (s)
1 node 12 threads	238.6
2 nodes, 4 sockets, 6 threads	193.1
2 nodes, 12 threads	137.1

The Apollo simulation of one million particles was run for varying number of threads on the Ember cluster at the Center for High Performance Computing (CHPC). Each node has a total of 12 cores but allows for hyperthreading. Thus the number of threads was varied from 1 to 24 to find the runtime and speedup by finding the average of five runs shown in Table 4.8. The speedup is a ratio of the runtime for a single thread divided by the runtime for multiple threads:

$$S = \frac{T_{\text{single-thread}}}{T_{\text{multiple-threads}}} \tag{4.30}$$

Speedup for the simulation is linear, with number of threads showing strong scaling until reaching the twelve cores, after which the performance gain with hyperthreading is less per additional thread; however, hyperthreading still increased performance by a small factor.

The number of nodes was then changed from 1 through 16, 20, and 32 nodes using the same Apollo simulation with one million particles averaging across five runs, shown in Table 4.9. The speedup was linear with the number of nodes, which shows the system has fairly strong scaling as the speedup is close to the additional number of nodes and threads. However, the speedup was not

Table 4.8: GEANT4 runtime and speedup by number of threads for simulation of 1 million protons through fullsized Apollo command module model of 15.8 m^3 on Ember cluster at CHPC.

Threads	Runtime (s)	Speedup	Threads	Runtime (s)	Speedup
1	3100	1	13	305	10.1
2	1560	2.0	14	298	10.4
3	1045	3.0	15	290	10.7
4	782	4.0	16	286	10.8
5	630	4.9	17	266	11.7
6	525	5.9	18	247	12.6
7	454	6.8	19	243	12.8
8	395	7.8	20	241	12.9
9	352	8.8	21	239	13.0
10	347	8.9	22	237	13.1
11	339	9.1	23	232	13.4
12	317	9.8	24	228	13.6

Table 4.9: Runtime and speedup by number of nodes and threads for simulation of 1 million protons through fullsized Apollo command module model of 15.8 m^3 on Ember cluster at CHPC.

Nodes	Threads	Runtime (s)	Speedup	Nodes	Threads	Runtime (s)	Speedup
1	12	225.6	1	10	120	29.3	7.7
2	24	136.4	1.6	11	132	29.8	7.6
3	36	86.1	2.6	12	144	27.1	8.3
4	48	66.8	3.4	13	156	22.6	10.0
5	60	53.4	4.2	14	168	21.9	10.2
6	72	46.2	4.9	15	180	20.2	11.2
7	84	40.4	5.6	16	192	19.8	11.3
8	96	34.0	6.6	20	204	12.6	18.9
9	108	30.9	7.3	32	216	8	28.5

equal to the number of nodes due to the extra costs of network communication and duplicating the simulation. A higher number of particles would show a speedup closer to the number of nodes. Figure 4.6 shows the runtime vs. threads, the runtime vs. nodes, speedup vs. threads, and speedup vs. nodes for the Apollo simulation.

Since the correlation for speedup vs. number of nodes to the data was close to one, the speedup was linear, showing strong scaling with nodes. Thus larger simulations with a higher number of particles would easily be solved with an increase in number of nodes. The time for loading of simulations and merging of run was minimal compared to the time to run a larger number of particles in an event loop. The merge function successfully merged the data between datasets, which was compared with manually adding up all the data from each node for each scorer.

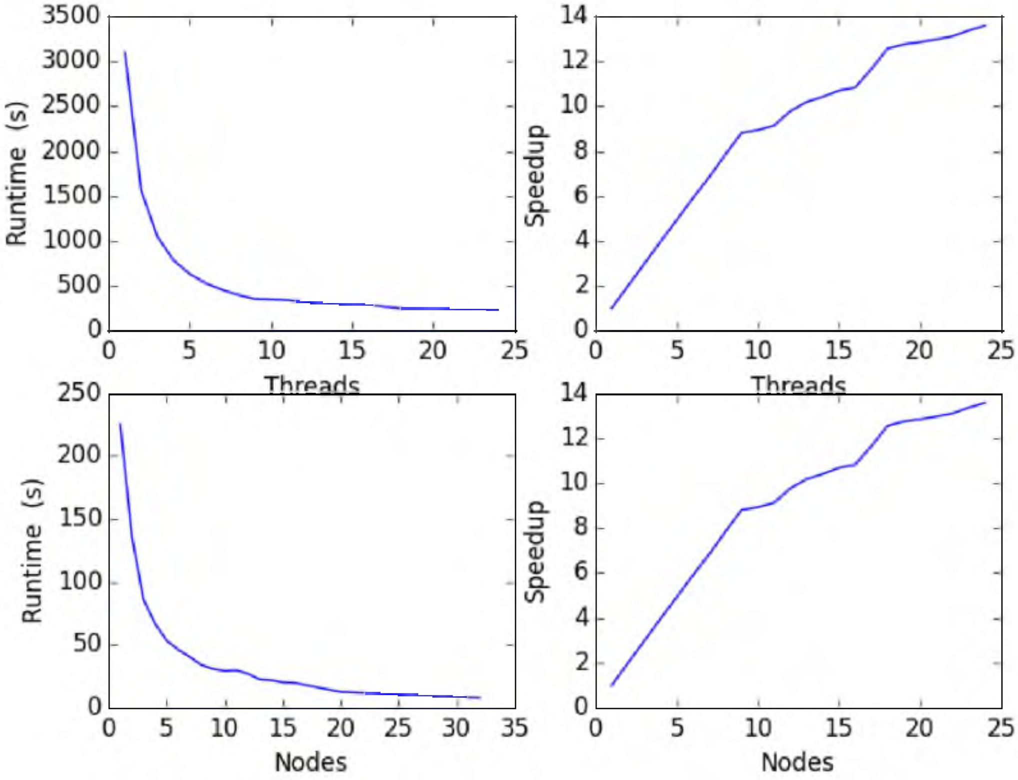

Figure 4.6: Performance runtime and speedup versus number of nodes and threads on Ember Cluster through fullsized Apollo command module model of 15.8 m^3 with 20 GeV Protons and one million particles.

CHAPTER 5

DOSIMETRY IN SPACE

5.1 Radiation Detector Types

Radiation is measured by observing its interaction with matter. Detectors have two main goals: collect as much radiation as possible deposited within the detector and convert the deposited energy into a readable signal. Radiation detectors function differently depending on the type: gas-filled, scintillation, or semiconductor detector. Gas-filled detectors contain a gas in a high electric field between an anode and cathode; the gas easily ionizes as radiation passes through the gas, depositing charge on the electrodes. Gas-filled detectors come in several different types depending on the voltage region of the detector, see Table 5.1 for a detailed comparison of the detectors [89]. In a scintillation detector, incoming ionizing radiation strikes a solid such as a crystal, liquid, or a gas producing photons of light. The scintillation material absorbs the radiation and luminesces. For example in a lanthanum-bromide detector, the detector is a crystal of La-Br_3, which luminesces with incoming radiation. A photomultiplier tube collects the light from the scintillation medium at the photocathode, creating a photoelectron that is amplified through each dynode by the high electric field until reaching the anode collection point. Semiconductor detectors, solid-state, are usually made of silicon or germanium. Incoming radiation creates a series of holes and electrons within the semiconductor structure that is carried to the anode and cathode, creating a current. Semiconductors have high-energy resolution, perform well in a vacuum, create a pulse proportional to incoming voltage, and are not affected by a magnetic field, but semiconductors have poor efficiency.

Thermoluminescent dosimeters (TLD) use a crystalline structure. When ionizing radiation strikes the crystal's electrons, the electrons jump from the valence band to either conduction band in ionization or exciton band forming an exciton [89]. The formed electron hole pair will migrate across the lattice until reaching a "trap" formed by impurities or lattice imperfections. The electrons remain in the trap for long periods of time at low temperatures. As the TLD is heated in a reader under a controlled atmosphere of gas, the electrons return to the valence band, releasing light, thermoluminescence. The reader counts the number of photons released. The process of heating and annealing returns the TLD structure to original, allowing for reuse. TLDs are commonly made

Table 5.1: Comparison of gas filled detectors with characteristics [89].

Detector	Ionization Chamber	Proportional Counter	Geiger-Muller Counter
Region	II- Ionization Region	III- Proportional Region	IV- Geiger-Muller Region
Output	Counts and spectra are possible in this region with pulse height proportional to energy.	Counts and spectra are possible in this region with pulse height proportional to energy.	Only provides number of counts, spectra are not possible because an ionization causes an avalanche of charge independent of energy.
Amplifier	Yes	Yes	No, avalanche of charge creates a strong signal that doesn't need an amplifier.
Voltage	<1000 V	800-2000 V	500-2000 V
Dead-time			High Dead time of 200-300ms
Electric Field	Weak enough where no charge multiplication occurs within the detector, thus only strongly ionizing radiation detected with the detector.	Strong enough where a single electron-ion pair creates secondaries proportional to energy.	Very strong that single electron-ion pair creates avalanche.

out of $CaSO_4$(Mn) or LiF. Space applications typically use TLD-100s made of LiF that contain 92.6% ^{7}Li and 7.4 % ^{6}Li, which, due to the high lithium neutron cross-section, can detect neutrons.

Solid-state nuclear track detectors (SSNTDs) such as plastic nuclear track detectors (PNTD) are made of cellulose nitrate, polymers, or Lexan polycarbonate. With high enough LET, the particles break the molecular bonds of the polymer, forming damage trails. Higher LET leaves a longer damage trail with the total number of tracks giving the flux. The process of etching analyzes PNTDs by soaking in a NaOH alkaline solution, which dissolves the tracks, leaving a pit at the surface visible with an optical microscope. PNTDs cannot detect electrons and have a minimum threshold LET of 5 keV/µm for detection, with an unknown sensitivity for pions and kaons. Also PNTDs cannot distinguish tracks lengths from 250-300 keV/µm due to the extremely short track lengths [90].

5.2 Dosimeters in Space Applications

Radiation Area Monitor (RAM) and Crew Passive Dosimeter (CPD) use TLDs and PNTDs to measure radiation levels through passive dosimetry. RAMs are placed throughout the spacecraft, whereas each astronaut carries a CPD for individual dosimetry. On the shuttle missions RAMs were swapped out each mission, whereas on the ISS they are swapped out regularly along with CPDs and returned to Earth on a capsule [91]. NASA also uses CR-39 PNTD's made of stacked sheets of .6 mm polymer arranged in mutually orthogonal orientations aboard manned spaceflights [92]. Other passive dosimeters used with little effect include photographic nuclear emulsions, bubble detectors, activation foils, and fission foils. Bubble detectors use a superheated fluid, which forms bubbles along the radiation path.

Tissue Equivalent Proportional Counter (TEPC) is a gas proportional counter, which measures the radiation entering in a 2μm diameter volume of tissue. The detector volume is approximately 6.3 in^3, surrounded by tissue-equivalent plastic [93]. The current produced in the proportional counter is directly related to the energy of the incoming particle, thus giving the LET spectrum, which combined with the ICRP-60 quality factor gives the astronaut dose. The Johnson Space Center's TEPC (JSC-TEPC) during the Space Shuttle mission provided data to validate current space radiation environment models. The instrument is a cylinder 5.08 cm long and 5.08 cm in diameter, with 1.9 mm thick tissue-equivalent plastic filled with a very low-pressure propane gas of 4 Torr [94]. The detector connects to a 256-channel analog to digital converter (adc) with sensitivity of .2-1250 keV/micrometer. The detector measures the linear energy spectrum each minute with absorbed dose every 2-20 seconds depending on the dose rate [90]. The TEPC measures a pulse height distribution with each pulse height corresponding to the linear energy of the incoming radiation, thus TEPC results vary within 10% of the real LET spectrum measured by other detectors [95]. The spectrum varied along shuttle path with an increase in dose as the shuttle passed the SAA. The TEPC measured through the shuttle path predominantly SPEs near the poles, predominantly GCR near the equator due to Earth's magnetosphere, and the SAA as the shuttle passed through the anomaly. Figure 5.1 shows the ISS TEPC, which is an updated version of the JSC-TEPC.

Charged Particle Directional Spectrometers (CPDS) combine semiconductor detectors in layers, with scintillation detectors measuring the flux of radiation along with secondary particles. CPDS contains a stack of lithium-drifted silicon detectors arranged in stacks, a Cerenkov detector, and a scintillation detector. The CPDS on the ISS is made of 13 separate detectors, shown in Figure 5.2 [91]. The A detectors are 1 mm thick lithium-drifted silicon. The Position Sensitive Detectors (PSD) are .3 mm thick silicon. The B detectors are 5 mm thick lithium-drifted silicon detectors. The C detectors (Cerenkov detectors) are a 1 cm thick sapphire crystal connected to a photomultiplier

Figure 5.1: ISS Tissue Equivalent Proportional Counter, used by permission Space Radiation Analysis Group, Johnson Space Center, NASA [11].

tube [96]. A plastic scintillator mantle surrounds the entire assembly with four photomultiplier tubes, whose output is summed in pairs. The A1 and A2 detectors work in coincidence as triggers for the detector, with each detector functioning in pulse-height mode to record the spectrum. The telescope collects coincidence data and data from each detector every 10 seconds with a 4096 channel ADC. NASA flew CPDSs on several space shuttle missions [97] and currently flies the CPDS inside the ISS in habitable areas with two CPDSs mounted externally at orthogonal angles on the truss to measure anisotropy [8].

CPDS detectors in space are being replaced by Radiation Assessment Detectors (RAD) based on the Mars Science Laboratory RAD. The RAD contains a charged particle detector (CPD) and a fast neutron detector (FND). The CPD consists of three silicon solid state detectors and an energy-resolving bismuth germanium oxide (BGO) detector to measure charged particle spectroscopy with a plastic scintillator and an anticoincidence plastic scintillator detector. The FND consists of a boron plastic scintillator connected to a photomultiplier tube [98].

Newer semiconductor pixel detectors based on the Timepix from CERN Medipix2 Collaboration provide the first small portable active detectors for deployment in space. The Radworks Project in the Space Radiation Analysis Group at Johnson Space Center deployed the detectors on the ISS in the Radiation Environment Monitor (REM). Each unit contains a silicon semiconductor sensor mounted by solder bumps to a Timepix 256 x 256 pixels chip [99]. Each unit is the size of a USB thumb drive and interfaces onboard the ISS by USB to existing laptops. The Timepix detector

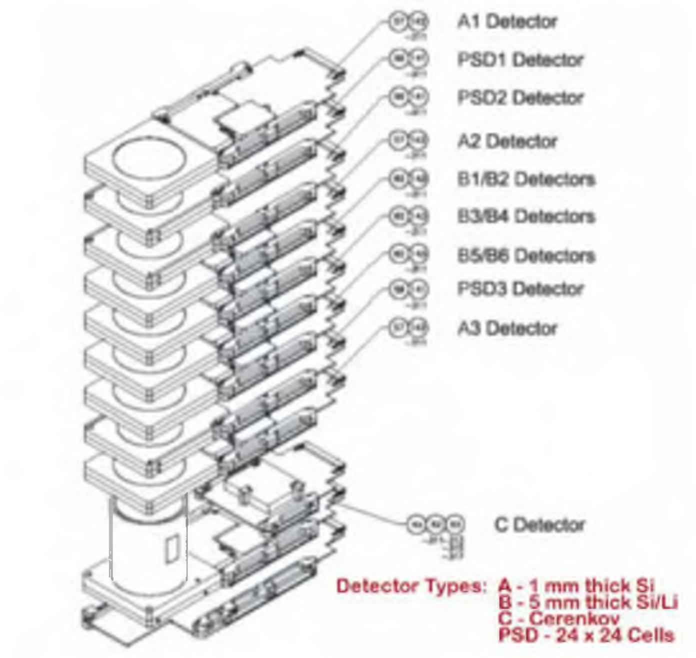

Figure 5.2: Charged Particle Directional Spectrometer (CPDS) diagram showing individual layers of the detectors, used by permission Space Radiation Analysis Group, Johnson Space Center, NASA [11].

was also deployed on Exploration Flight Test 1 (EFT-1) of the Orion space capsule in the Battery-operated Independent Radiation Detector (BIRD) for verification with RAM passive dosimeters. The detector is currently being integrated into a new Hybrid Electronic Radiation Assessor (HERA) as a distributed monitoring system for the Orion space capsule, which will integrate several REM detectors in various locations with active data download to mission control [100].

5.3 Requirements for Radiation Dosimeters in Space Missions

Radiation dosimeters onboard space missions must measure a varied spectrum of radiation from GCR, SPE, and radiation belts with a large energy spectrum. Space radiation detectors follow three constraints: detectors must be safe for the crew, with constraints on high voltage power supplies or polymer materials outgassing; equipment must be small and light-weight to avoid high launch costs yet robust enough for launch with minimal needed spare parts or electrical power; and detectors must detect a huge variety of particle species with a very large range of fluxes [8]. Even two different astronaut crew members within a craft can receive significantly different fluxes as much as by a factor of two within the same spacecraft shielding due to the anisotropic flux distribution [18], requiring individual crew dosimetry. Thus space agencies use varied types of detectors together to create an overall measurement of the radiation environment.

NASA requires monitoring of each crewmember's radiation exposure by a personal dosimeter under Medical Operations Requirement Document (MORD), requiring wearing dosimeters at all times, including during extravehicular activities (EVAs). MORD requires measuring human tissue absorbed dose, radiation environment inside the spacecraft, and exterior radiation environment during EVAs [44]. To achieve this, the Space Radiation Analysis Group (SRAG) at Johnson Space Center develops, maintains, and implements radiation detectors onboard all spacecraft, as well as providing operational support to flight controllers and crew. Under SRAG direction, the crew deploys RAMs at designated fixed points on the ISS with four to six in each module and three or four in each ISS node, all replaced just before switching crews. The RAMs measure integral absorbed dose and average radiation quality factor. Active radiation monitoring provides real-time differential radiation spectrum data to crewmembers and ground controllers to reduce radiation exposures to as low as reasonably achievable (ALARA). Active systems give an estimate to internal organ dose and LET spectrum, downlinking LET spectrum data approximately every minute to ground control, or more often as needed. Active systems are moved within the modules to survey exposure at different areas and programmed to trigger radiation alarms when exceeding a threshold. SRAG records detailed time differential particle fluxes by particle on ISS downlinked at least daily. The MORD also requires neutron exposure monitoring, which may yield 10%-30% of dose to astronauts. Each crewmember's record contains detailed biodosimetry data in their medical records maintained by SRAG and the Human Spaceflight Program.

Passive dosimeters such as TLDs or SSNTDs are ideal for spaceflight due to their small size, low mass, no power consumption, and reliability; however, passive dosimeters must be returned to the Earth for measurement postmission through labor-intensive analysis with the disadvantage of no real-time data or differential flux. Of these, TLDs are the most widely used contained in CPDs and RADs for individual crew monitoring and official crew record. CPDs use a single TLD, whereas RADs may use multiple arranged in stacks or pockets with CR-39s. NASA used the CR-39 PNTDs to characterize the LET spectrum onboard the ISS [8, 101]. Currently SRAG combines TEPC and TLD data along with the characterized LET spectrum to calculate absorbed dose for each astronaut.

Space-based passive dosimeters are similar to their Earth-based counterpart TLDs and PNTDs; however, on Earth the dosimeters can quickly be processed in a lab to record dose measurements and annealed to return to use, unlike in space, where astronauts must wait until a return capsule can return the dosimeters back to Earth often months later. The KFKI Atomic Energy Research Institute in Hungary developed an onboard reading system for TLDs on the ISS, creating a small unit with heater, photomultiplier tube (PMT), and microprocessor control unit with removable flash memory storage [102]. The TLD reader heats the thermoluminescent material and records the emitted photons with the PMT, allowing astronauts to read TLDs and reuse in space instead of returning to Earth;

however, SRAG still analayzes all NASA astronaut dosimetery on Earth.

The Utah Nuclear Engineering Program (UNEP) has two TLD readers for measuring TLD passive dosimeters. Both heat the TLD in nitrogen gas to a temperature and count the number of photons released by the TLDs. In UNEP to read each TLD, first the nitrogen gas is turned on to the detector. Next the TLD is placed in the sample holder shown in Figure 5.3. Next the start counting button is depressed, and the reader resets the counter and begins to heat the TLD as simultaneously the PMT measures any photons released from the TLD. The number of counts of photons is then displayed on the reader counter, giving the flux. TLDs are calibrated by placing several sample TLDs in a particle accelerator at several different fluxes and energies to develop a response curve, which is then applied to the measured counts from the TLDs to create a dose measurement.

Active dosimeters on Earth are very similar to their space-based counterparts; however, some space-based detectors such as the CPDS are arranged in series of detectors to create a telescope, giving angular resolution of radiation direction. Active detectors provide real-time LET spectra, dose, and dose equivalent measurement. With newer detectors, active detectors are becoming more compact, require less energy, and are more robust, making them a more ideal solution for time-dependent needed spectrometry, especially during SPEs. Space-based active detectors are more compact and require less energy for operation. Table 5.2 shows a comparison of passive and active detectors for applications, including their types, advantages, disadvantages, and uses for radiation monitoring [8].

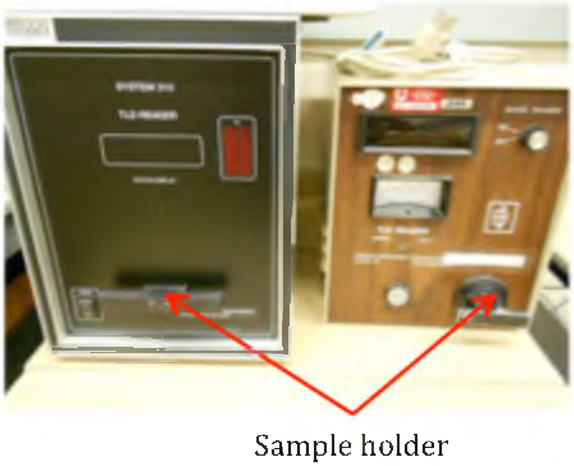

Figure 5.3: Utah Nuclear Engineering Program TLD readers showing location of sample holder, counting screen, and temeperature scale.

Table 5.2: Comparison of Passive to Active Detectors

Detector	Types	Advantages	Disadvantages	Uses
Passive Detectors				
TLD	TLD-100 TLD-600 TLD-700	• High sensitivity • Small size and mass • Portable • Reusable • Sensitive to many different particles including neutrons	• One-time reading before heating. • Requires TLD reader. • No time differential flux data • No LET spectrum • No Particle Species Information • Labor Intensive	• CPD • RAM • Flux • Dose • Radiation-Workers • Area-Monitoring
SSNTD or PNTD	CR-39 Cellulose Nitrate Lexan	• High sensitivity • Small size and mass • Portable • Sensitive to many particles • LET Spectrum	• One-time reading • Requires chemical processing • No time differential flux data • Labor Intensive • Chemical Outgassing	• CPD • RAM • Flux • Dose • LET Spectrum
Active Detectors				
Gas Filled Proportional Counters	TEPC	• Sensitive to many particles • LET Spectrum • Time dependent information • Tissue Equivalency • Downloadable data to ground	• Requires high-voltage • Larger size with extra mass • Electronic component failure • Requires constant calibration • Longer Dead Time for high flux	• Differential Flux Spectra • LET Spectrum • Dose • Area-Monitoring
Solid State Detectors	Si-Detectors CPDS DOSTEL RRMD Liulin RAD REM	• Sensitive to many different particles including neutrons • LET Spectrum • Time dependent information • Angular Distribution Resolution • Higher Resolution • Downloadable data to ground	• Requires high-voltage • Larger size with extra mass • Electronic component failure • Requires constant calibration	• Differential Flux Spectra • LET Spectrum • Dose • Area-Monitoring
Scintillation Detectors	CPDS RAD	• LET Spectrum • Time dependent information • Downloadable data to ground control.	• Requires high-voltage • Larger size with extra mass • Electronic component failure • Requires constant calibration	• Differential Flux Spectra • LET Spectrum • Dose Area-Monitoring

5.4 Dosimeters Onboard Apollo Missions

The Apollo missions used several different types of detectors: Nuclear Particle Detection System (NPDS), Van Allen Belt Dosimeter (VABD), three Personal Radiation Dosimeters (PRD), a Radiation Survey Meter (RSM), and each astronaut carried four thermoluminescent detectors (TLDs). The NPDS and VAPD sent telemetry data to Earth for collection, the PRD and RSM were read twice daily by astronauts to the ground [9]. The NPDS is a charged particle counter measuring protons in four energy bins between 10-170 MeV and alphas in three energy bins between 42-318 MeV [103]. The VABD is an aluminum-walled ionization chamber; aluminum was chosen over tissue-equivalent plastic because of flammability concerns. The PRD was a 7.1 cm^3 tissue equivalent ion chamber with visual read-out of accumulated dose. The PRD fit inside each crew member's coveralls and was 5.46 in^3. The TLDs were lithium fluoride packaged with nuclear emulsions, neutron dosimetry foils, and particle track foils. TLDs were analyzed in a lab after completion of the mission. The RSM was a 10 cm^3 tissue-equivalent ion chamber with readout used to determine radiation levels throughout the capsule. In case of a SPE, the crew would have used the RSM to survey across the capsule for the lowest radiation level to find the safest shelter location [9].

5.5 Dosimeters Onboard International Space Station

The International Space Station radiation environment is monitored by active and passive dosimetry. For passive dosimetry, each crewmember onboard the ISS carries a crew personal dosimeter (CPDs), and each module has radiation area monitors (RAMs). Active dosimetry includes a mixture of different instruments: TEPC, CPDS, REM, and RAD detectors. The first TEPC onboard ISS started operation in October 2000, operating continuously except for its history of failures. Currently onboard are the operational TEPC and a backup unit. NASA deployed the Intra-Vehicular CPDS (IV-CPDS) in March 2001, measuring ISS internal charged particles until it failed in 2006. NASA currently estimates radiation exposure from charged particles based on historical IV-CPDS data to estimate current exposure. The ISS Program approved second-generation replacements for the IV-CPDS, RADs, an Intra-Vehicular TEPC (IV-TEPC), and three Extra-Vehicular TEPCs (EV-TEPC), which are in deployment.

Also flown on ISS were two different Si-telescope-based spectrometers: Dosimeter-telescope (DOSTEL) from Germany and Real-time Radiation Monitoring Device (RRMD-III) from Japan. [8]. DOSTEL uses two 315μm-thick passivated implanted planar Si-detectors (PIPS) with a sensitive area of 692 mm^2 and a gap distance between detectors of 15 mm. DOSTEL detects LET spectrum between .1-200 keV/μm. DOSTEL flew aboard several space shuttle missions and Euromir-97 [104].

Doke group at Tsukuba Space Center developed the RRMD-III using three 50 μm-thick position-sensitive Si-detectors (PSDs) in a stack configuration with a gap distance of 5 mm and an active area of 4 cm^2. RRMD-III measures LET spectrum from .2-400 keV/μm. The three detectors work in coincidence mode with the top and bottom serving as triggers, and the middle detector measures energy deposition, giving angular resolution of 3.22° [105].

The MATROSHKA phantom torso and head from the ESA measures the radiation depth dose distribution to organs inside a simulated anthropomorphic tissue-equivalent polyurethane and skeleton structure. The phantom is .37 x .37 x .39 m with thirty-three tissue-equivalent slices 25 mm thick and a mass of 32 kg. The phantom has four radial perpendicular channels and holes for detectors. Astronauts in space exchanged CR-39s and TLDs detectors placed throughout the phantom in tissue-equivalent containers. A Russian-designed Liulin Si-detector telescope placed within one of the perpendicular tubes measures energy deposition spectrum, dose rate, and particle flux at different depths [106]. The TLDs and CR-39s read on the ground give LET spectrum and absorbed dose deposition. The ESA found critical organ locations for the model from an x-ray CT scan 3D model that was converted into a numerical voxel model applied to an ICRP reference man. Dose rates across the phantom are calculated from the TLD point sources using inverse distance weighting method [107].

5.6 Development of GDML Detector Models for GEANT4

Three different detector models were developed in GDML for GEANT4 based on previous studies: ICRU Phantom Sphere, CPD, and JSC-TEPC, which can be added to any spacecraft geometry by inserting a link to the detector GDML file within the spacecraft GDML file. The GDML for each detector contains a line to change the placement of the detector, the needed materials for the detector, each geometric component, and nested physics volumes with the GDML auxiliary field for sensitive detector to attach the associated sensitive detector on load time.

The International Commission on Radiation Units (ICRU) defines an ICRU phantom sphere as 30 cm diameter tissue-equivalent sphere [108]. The density of the sphere is 1 g/cm^3, with a mass composition of 76.2% oxygen, 11.1% carbon, 10.1% hydrogen, and 2.6% nitrogen to simulate tissue. The sphere mimics the radiation deposited within an individual for absorbed dose, which then by applying standards from ICRP weighting factors gives equivalent dose to an individual. In Monte Carlo simulations, the ICRU sphere creates an easy way to measure dose and energy deposition in a standard defined phantom medium. The GDML file creates a sphere of radius 15cm filled with the tissue equivalent material.

The Crew Personal Dosimeter (CPD) contains 32 cylinders of 5 mm diameter by 1 mm thickness TLD-100 material embedded in a 4.5 cm by 3.5 cm Lexan holder [109]. Using picture analysis from photographs of a CPD and a few published dimensions, LogerPro software by Vernier computed the size and location within the Lexan of the TLDs by creating a scale for each pixel and measuring the number of pixels across, shown in the GDML model Figure 5.4. The GDML creates TLD-100s of 92.14% Lithium-6 fluoride and 7.26% Lithium-7 fluoride material with a density of 2.64 g/cm^3, ignoring the small percentage of doping Mg and Ti. Six hydrogen, three carbon, and three oxygen atoms form each molecule of the Lexan material with a density 1.2 g/cm^3. The GDML first creates the Lexan solid and a single TLD solid. Then using loops in GDML creates 32 TLD volumes, placing them within the Lexan as physics volumes, shown in Figure 5.4.

The JSC-TEPC design was used on the space shuttle and ISS until 2009. The model was developed from available documentation of the JSC-TEPC [110] and documentation on the newly designed TEPC [111]. The model is a 5.1 cm inside diameter cylinder 5.1 cm long. The outside casing of the TEPC is a vacuum chamber of assumed Stainless Steel-303 2 mm thick. Inside the casing is A-150 plastic with density of 1.127 g/cm^3. Table 5.3 shows the chemical composition of each material in the TEPC model [112]. The detector contains propane gas of chemical composition C_3H_8 at a pressure of 15 Torr, which was calculated to density of 3.62x10^{-5} g/cm^3 at 20° Celsius as follows:

$$\rho = \frac{P \cdot MW}{RT} \tag{5.1}$$

The TEPC model is made of four tubes in the GDML: interior propane, tissue-equivelent plastic cylinder, vacuum cylinder, and the casing of stainless steel with each layer nestled as a physics volume within the outer layer shown in Figure 5.5.

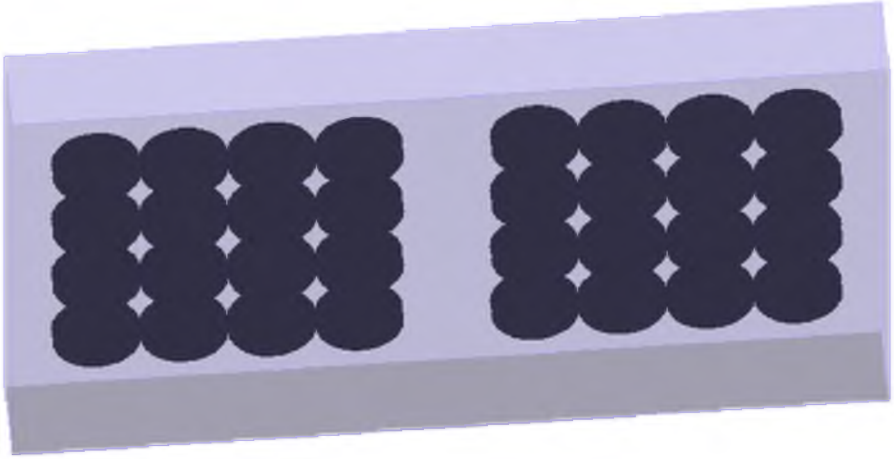

Figure 5.4: GEANT4 GDML model of CPD with 16 TLD-100s mounted in a Lexan holder.

Table 5.3: Composition of TEPC materials by element and fractional composition.

A-150 Plastic		Stainless Steel 303	
Element	Fractional Composition	Element	Fractional Composition
Hydrogen	10.2%	Nickel	9%
Carbon	76.8%	Chromium	18%
Oxygen	5.9%	Iron	69.81%
Nitrogen	3.6%	Fluorine	1.7%
Calcium	1.8%		

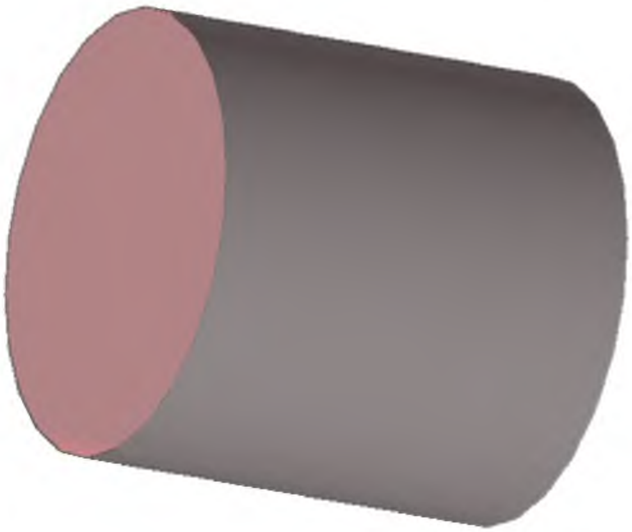

Figure 5.5: GEANT4 model of TEPC showing the exterior casing of stainless steel.

5.7 Comparison of Simulated Energy Deposition within Detectors

A simulation was run for each detector for the worst week spectrum from SPENVIS of worst case solar proton flux from the CREME96 database for 180 hours starting on October 19th, 1989 at 13:00 UT from the GOES satellite. The simulation ran ten million protons using a spherical surface source with Cosine Law distribution from 0 to 2π. The source surface was .2 m in diameter for all three detectors, slightly bigger than the ICRU Sphere Phantom. The normalization factor was calculated using equation 4.18 as $5.6\text{x}10^8$. The simulations ran on the Center for High Performance Computing CHPC Ember cluster with 24 threads running one CPU-hour.

The results shown in Table 5.4 show a significantly higher energy deposit in the ICRU due to significantly higher number of particles passing through the detector because of the larger volume of the detector. Figure 5.6 shows a comparison of the energy deposition within the three detectors versus the proton energy, whereas Figure 5.7 shows the normalized energy deposition obtained by

Table 5.4: Energy deposited, dose, and number of particles scored for TEPC, ICRU sphere, and CPD detector simulations in GEANT4 using 10,000,000 particles proton flux for worst case SPE model from SPENVIS [12].

Detector	Energy Deposited (GeV)	Dose (Gy)	Number of Particles Scored	Error	FOM
TEPC	6.4×10^{1}	2.7×10^{-3}	1.25×10^{4}	0.0110	7.10
ICRU Sphere	3.7×10^{5}	4.2×10^{-6}	2.81×10^{6}	0.0021	188
CPD	1.5×10^{2}	4.7×10^{-4}	3.83×10^{2}	0.0628	0.127

dividing each bin by the maximum energy deposition within a bin. Figure 5.6 shows the ICRU as most efficient, followed by CPD and TEPC models. The CPD was the smallest detector, thus the number of particles passing through the detector should be the least in energy deposition; however, since the TLDs are denser than the gas within the TEPC, more energy was deposited in the CPD. Each of the detectors had a different response curve, with the ICRU spheres being most sensitive in low energy range, whereas the TEPC showed the most uniform energy deposition by proton energy. Since the ICRU sphere scored significantly more particles in the simulation, the ICRU sphere creates a more practical detector within simulations.

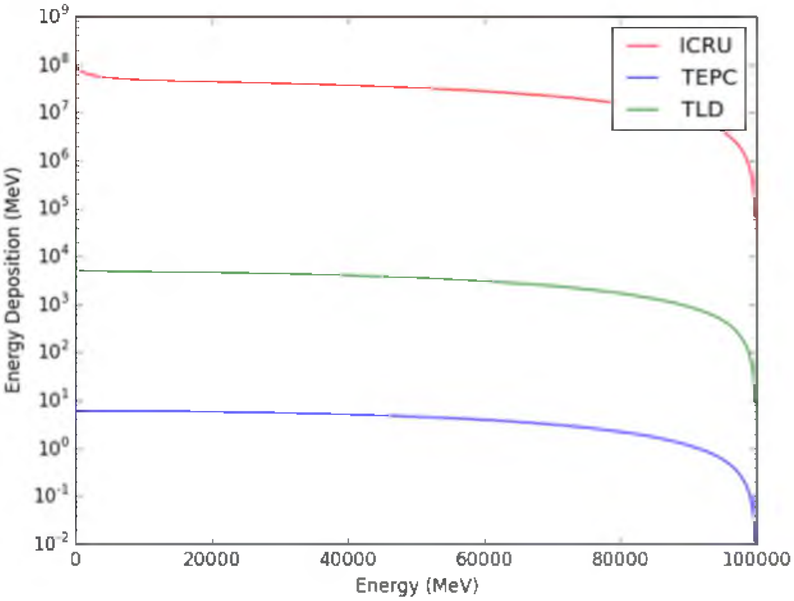

Figure 5.6: Energy deposition in GEANT4 within ICRU, TEPC, and TLD detector models versus proton energy.

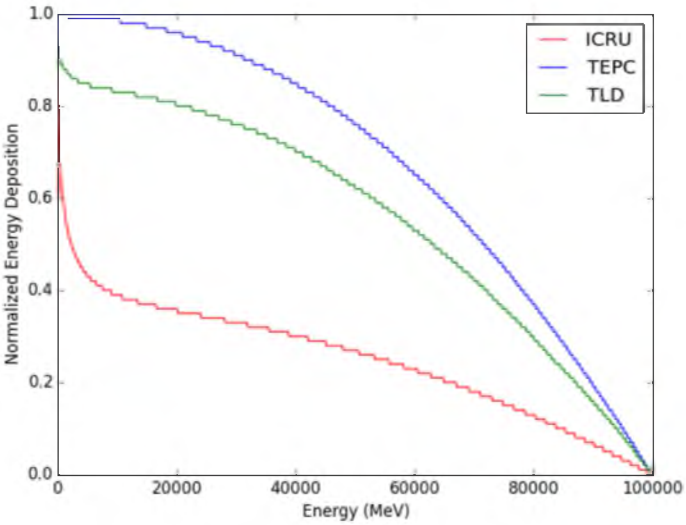

Figure 5.7: Normalized energy deposition in GEANT4 within ICRU, TEPC, and TLD detector models versus proton energy.

CHAPTER 6

GEANT4 MODELING OF THE RADIATION EXPOSURE TO THE INTERNATIONAL SPACE STATION

6.1 Dose Estimation by Simulation of the ISS Radiation Environment (DESIRE) Project

The "Dose Estimation by Simulation of the ISS Radiation Environment" (DESIRE) project created the first large-scale published simulations of the ISS [2]. The study estimated radiation doses for astronauts within the Columbus Module of the ISS for SPEs, GCRs, and trapped radiation belts during both solar maximum and solar minimum using full-sized GDML models of the module with varying geometry and ISS models. Tori Ersmark painstakingly created for the project detailed geometrical models of the ISS from hardcopy drawings of the ISS, since there are currently only inconsistent methods for converting Computer Aided Drawings (CAD) to GEANT4 geometry [84]. The study created three basic models of the Columbus module and ISS in the 14A configuration with a mass of 352 metric tons and 350 separate geometry volumes.

The DESIRE study simulated dose for the Columbus module only, the Columbus module with a truncated geometry, and the Columbus module with a full-sized ISS geometry. The full ISS geometry correctly simulates possible secondary radiation generation from the full structure that enters the Columbus module. However, the larger the geometry, the longer the run time due to the increased volume requiring a higher number of particles to traverse the geometry to reach the detectors and deposit energy within scorers. The larger the volume, the lower the probability of the particles entering the scoring volume, thus the truncated geometry mimics secondary production from the ISS structure while reducing the simulated volume.

Each habitable module of the ISS was created of symmetric cylinders with an inside containing a box of diagonal dimension that is 50 cm less than the diameter of the cylindrical module filled with air. To approximate the correct mass of the module, the volume from cylindrical sphere to interior box was made of aluminum with a density to give the correct module mass. Ersmark then fitted each module with hatch openings for connecting modules. Three other modules had a different design:

the Cupola module used a cylindrical exterior and interior, whereas the Soyuz and Progress have only a symmetric cylindrical structure inside the hull without an interior. The habitable modules also contained solar panels and payload platforms based on estimated masses [2].

The ISS model contains other modules, including the Pressurized Mating Adapters (PMAs) made of aluminum with a thickness to give the measured PMA's mass, truss segments, solar panels, radiators, and other components modeled of aluminum with the approximate size and mass simplified to a few volumes, see Figure 6.1.

Columbus model one is a simplified cylinder model consisting of 10 volumes with a mass of 4386 kg, 25% of real module mass, with an exterior hull of aluminum 2219 that contains 5% copper. A Meteoroid and Debris Protection System (MDPS) surrounds the hull, providing significant radiation shielding made of 1.6-2.57 mm aluminum 6061T6, 5.6 mm Kevlar, 5.3 mm NextTel 650, and with a 3.8-4.8 mm aluminum 2219 hull, shown in Table 6.1. Columbus model two has 23 volumes, with a correct total mass of 16,750 kg and hull mass of 3,004 kg. The model has a main cylindrical shape with slanted end cones. The interior of the module is rectangular, similar to other habitable modules with the volume between hull and rectangular area filled with aluminum to a density to match module mass [84].

The third most detailed Columbus model contains around 750 volumes with the correct mass of

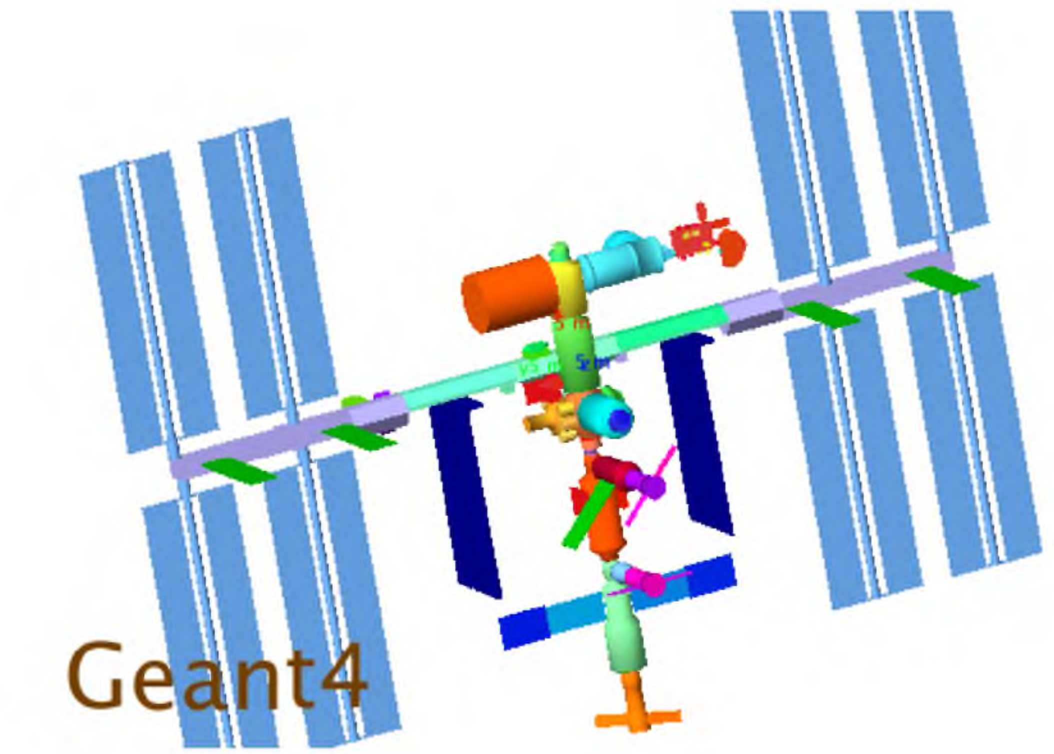

Figure 6.1: Complete ISS geometry model from Ersmark within new multithread GEANT4 application.

Table 6.1: Meteoroid and Debris Protection System (MDPS) for the ISS showing materials and thicknesses [113].

Material	Thickness (mm)
Aluminum 6061 T6 Interior	1.6-2.57
Kevlar	5.6
NexTel 650	5.3
Aluminum 2219 Hull	3.8-4.8

16,750 kg. The hull used the same material thicknesses of Columbus model 1; however, the total hull mass was less than the 3,004 kg due to not modeling structural interfaces, so Ersmark increased the thickness by 50% to match the correct hull mass. The interior contains 16 racks in the generally correct shape with a material estimated as a mixture of aluminum, steel, and plastic to give the correct module mass [84].

Within the Columbus module, the simulations used 15 ICRU spheres of 15 cm radius as the scoring volume. The spheres are arranged with a center sphere and four surrounding spheres longitudinally with three sets at port, starboard, and center, see Figure 6.2. For the Columbus module only, the source was a cylindrical surface of 4.3 m by 2.0 m diameter placed around the Columbus geometry. For the truncated geometry and full ISS geometry, the source was a sphere of radius in diameter larger than the geometry. The study ran simulations with each of the three Columbus geometries for SPEs, trapped protons, and GCR for solar maximum and minimum at different altitudes, requiring 464 CPU-days of computation.

The simulations using the Columbus 2 and Columbus 3 showed very similar results for dose rate well below the margin in error of the incoming radiation environment deviation and significantly less than the Columbus 1 model. Thus geometry of less detail with the correct total mass and hull structure validly simulates a spacecraft within the margins of error from the incoming spectrum. The truncated and full ISS geometry reduced the dose rate for the Columbus module with an additional slight decrease in dose rate for the full geometry, thus the truncated geometry can roughly approximates the full geometry. The project found an increase in dose rate with altitude as expected. Calculated dose rates for solar maximum and solar minimum for trapped proton and GCR showed good agreement with experimental data.

6.2 GEANT4 High-Performance Simulations of ISS

The first set of simulations compared the three physics lists: QGSP_BIC_HP, QGSP_BERT_HP, and QBBC using the Columbus 3 model with truncated geometry from the DESIRE Project by Tori Ersmark [82]. The simulations validated the three lists using an AP-8 spectrum from Solar Maximum between April 14th and August 2001, and were compared with published data from the ISS [104].

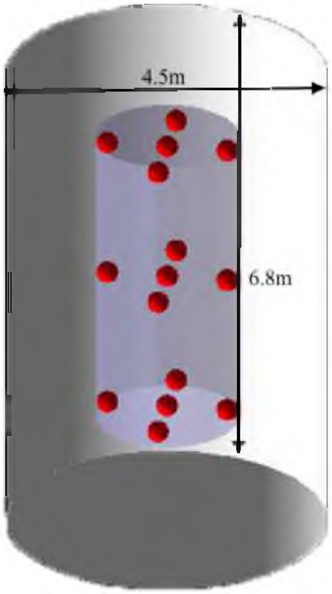

Figure 6.2: Columbus module from Ersmark in GEANT4 showing ICRU tissue equivelent spheres in red.

During Solar Maximum in 2001, the space station was at a higher altitude of about 400 km, which was higher than the simulated 380 km from the DESIRE Project. The next simulations compared the dose rate for the same Solar Maximum using all nine DESIRE Project geometry models: Columbus 1, 2, and 3 with no ISS (ISS0), truncated geometry (ISS1), and the full ISS geometry (ISS2). The final set of Solar Maximum simulations were run using AE-8 for trapped protons and GCR using the ISO 15390 model for the mission epoch. See Table 6.2 for a list of simulations with mission epoch, geometry model, radiation flux model, and computational time.

Next a series of simulations were run for Solar Minimum from April 1st through summer 2009. On April 1st, the ISS was boosted to its highest altitude during the time period, thus would have the highest dose rate from April through summer for comparison with the DOSIS experimental data and simulations by Chavy-Macdonald et al. [81].

The ISS simulations used three macro files to describe the run, see Appendix B for samples. A particle macro file defined the particle, energy spectrum, and normalization factor, which were created in SPENVIS for each radiation environment and time period. The first step in SPENVIS is to create spacecraft coordinate locations using the Coordinate Generator. Since the radiation flux varies with altitude and the ISS varies in altitude over time from 330 to 435 km at an inclination of 51.6°, the spectrum files were created using North American Aerospace Defense Command's (NORAD) Two Line Element sets (TLE) for more precise altitude and orbital parameters during

Table 6.2: List of ISS simulations with geometry model, mission epoch, and radiation flux model.

	ISS Model	Mission Epoch	Radiation Flux Model
Physics List Comparison • QBBC • QGSP_BIC_HP • QGSP_BERT_HP	Col3ISS1	April-July 2001	AP-8
Model Comparison	Col1ISS0 Col1ISS1 Col1ISS2 Col2ISS0 Col2ISS1 Col2ISS2 Col3ISS0 Col3ISS1 Col3ISS2	April-July 2001	AP-8
Solar Maximum	Col3ISS1	April-July 2001	AP-8, AE-8, GCR ISO 15390
Solar Minimum	Col3ISS1	June-September 2009	AP-8, AE-8, GCR ISO 15390
SPE	Col3ISS1	September 24th 2001	• ESP-PYSCHIC Total Fluence • ESP-PYSCHIC Worst Case • Rosenqvist • JPL • King

the time period. The station was at higher altitude during Solar Maximum in 2001 then in 2008 during the Solar Minimum shown in Table 6.3. TLE data contain two 69-character-long lines that describe a satellite's location surrounding the Earth. TLE contains all the information needed to describe the orbit of the satellite, including number, international designation, launch year, epoch of observation year and day, inclination, right ascension of ascending node, eccentricity, argument of perigee, and mean anomaly. The TLE data for the ISS were obtained from CelesTrak for NORAD Catalog Number 25544 for the first launched module ZARYA in 1998, shown in Table 6.3. The coordinates were generated for a period of 100 days and output resolution of 120 s.

After each set of coordinates was generated, the Radiation Sources and Effects module created the associated spectrum for trapped protons (AP-8 model), trapped electrons (AE-8 model), SPE (ESP-PYSCHIC Total Fluence, ESP-PYSCHIC Worst Case, Rosenqvist, JPL, and King models), and GCR (ISO 15390) model during the given time period and solar cycle. Then the Definition of Source Particle Tool under GEANT4 Tools created the spectrum files with normalization factors

Table 6.3: ISS Zarya TLE orbit data for simulations during different time periods, the first two lines are the TLE data with a synopsis of apogee, perigee, and inclination data below.

Solar Maximum April 14th 2001 TLE Data
1 25544U 98067A 01104.52673611 .00070402 00000-0 82389-3 0 8723
2 25544 51.5720 49.5298 0012466 275.4455 251.8416 15.60813637137132
Apogee Altitude: 402.50 km
Perigee Altitude: 394.17 km
Inclination: 51.59°
Solar Minimum April 1st 2009 TLE Data
1 25544U 98067A 09160.12255947 .00017740 00000-0 12823-3 0 24
2 25544 51.6405 348.2892 0009223 92.2562 9.3141 15.73542580604683
Apogee Altitude: 359.32 km
Perigee Altitude: 342.34 km
Inclination: 51.62°
Solar Particle Event on September 24th 2001 TLE Data
1 25544U 98067A 01267.15529505 .00057549 00000-0 70444-3 0 5075
2 25544 51.6391 310.7644 0007785 126.5522 329.6827 15.59781246162523
Apogee Altitude: 396.43 km
Perigee Altitude: 383.62 km
Inclination: 51.62°

with the option for linear energy biasing to improve statistics in extreme energy bins and increase number of scored particles. For the trapped spectra, the normalization factor was divided by 100 to get the fluence per day for μGy/day unit instead of the 100-day fluence. For SPE, the normalization factor from GEANT4 tools gives the total fluence for the event, so the factor was not changed. For GCR, the normalization factor is given in units of particles/cm^{2}s, thus needs to be converted into particles/cm^{2}day. A gps macro file defined a spherical source, radius for the sphere, and surface area of the source for normalization, which varied depending on geometry model. The surface area for the sphere was found by converting the radius into cm and using the equation below, since the current through the sphere is dependent on surface area in units of particles/cm^2 s.

$$A = 4\pi r^2 \tag{6.1}$$

Table 6.4 shows the spherical source radius for each geometry model with the calculated surface area. The last macro file ran the simulation by selecting the geometry file, executing the GPS and spectrum macro file, and running the number of particles.

The Center for High Performance Computing Ember and Kingspeak clusters ran simulations using 24 to 40 threads, respectively. The doses for all fifteen ICRU spheres were averaged along with the error measurements, and the standard deviation was calculated between the spheres.

Table 6.4: Spherical source radius and surface area by ISS geometry model.

ISS Model	Spherical Source Radius (m)	Surface Area (cm^2)
Columbus Only col1iss0 col2iss0 col3iss0	7	$6.16x10^6$
Columbus with Truncated ISS col1iss1 col2iss1 col3iss1	20	$5.03x10^7$
Columbus with Full ISS col1iss2 col2iss2 col3iss2	60	$4.52x10^8$

6.3 ISS Simulated Dose and Equivalent Dose

In the comparison of the three physics lists, Table 6.5 and Figure 6.3 show that all three physics lists resulted in similar dose rates and equivalent doses. The calculated quality factor was 4.9, significantly higher than the measured quality factor from DOSTEL and TEPC detectors onboard the ISS. The QGSP_BERT_HP list ran the slowest, with QBBC the fastest, thus the QBBC physics list was used for the rest of the simulations.

Table 6.6 and Figure 6.4 show a comparison of the simulated dose for different geometry models. The Columbus model 1 shows the greatest dose due to the smaller shielding density. The addition of the truncated or full ISS geometry reduced the dose due to the increased shielding for a large shielding angle similar to results from the DESIRE project [82, 83]; however, the variation between the two was within 10-15%, less than the standard deviation between locations within the module, thus confirming a truncated geometry can accurately describe the full station geometry without the needed detail. Columbus model 2 showed a lower dose rate than the more detailed Columbus model 3, probably from secondary particle generation by the additional shielding.

Table 6.5: Simulated dose for different GEANT4 physics lists for ISS Columbus Col3iss1 module with trapped protons during Solar Maximum in 2001.

Physics List	Dose (μGy/day)	Quality Factor	Equivalent Dose (μSv/day)	Relative Error
QBBC	71.13	4.9	347.44	0.84%
BIC	71.16	4.9	347.32	1.03%
BERT	71.96	4.9	349.16	1.03%

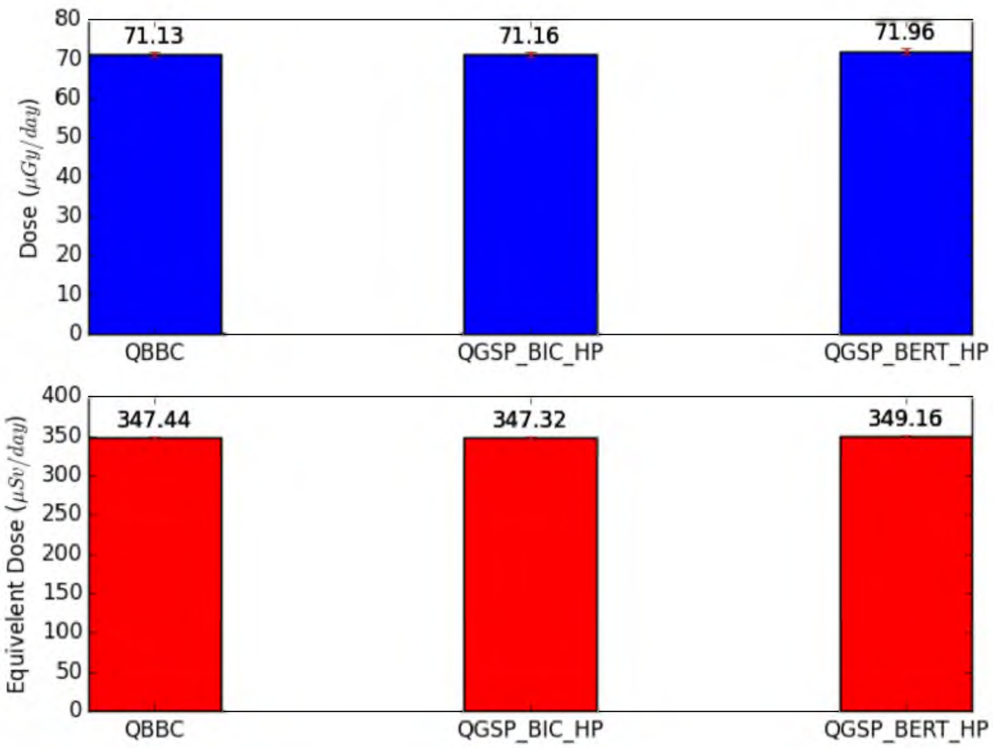

Figure 6.3: Comparison of GEANT4-computed dose for different physics lists using Col3iss1 model with protons during Solar Maximum in 2001.

Table 6.6: GEANT4-computed dose deposit within different geometry models for protons during Solar Maximum in 2001.

Geometry Model	Dose (µGy/day)	Quality Factor	Equivalent Dose (µSv/day)	Standard Deviation (µGy/day)	Relative Error	Particles
col1iss0	269.3	4.9	1323.8	11.3	0.36%	5x10^8
col1iss1	219.3	4.9	1078.0	21.1	0.80%	1x10^9
col1iss2	214.3	4.9	1052.5	43.6	2.38%	1x10^9
col2iss0	85.3	4.9	418.7	18.9	0.44%	5x10^8
col2iss1	59.3	4.9	290.8	6.6	0.93%	1x10^9
col2iss2	63.4	4.9	309.2	15.4	2.87%	1x10^9
col3iss0	88.9	4.9	436.8	28.3	0.52%	5x10^8
col3iss1	71.1	4.9	347.4	16.0	0.84%	1x10^9
col3iss2	70.8	5.0	351.5	25.6	3.16%	1x10^9

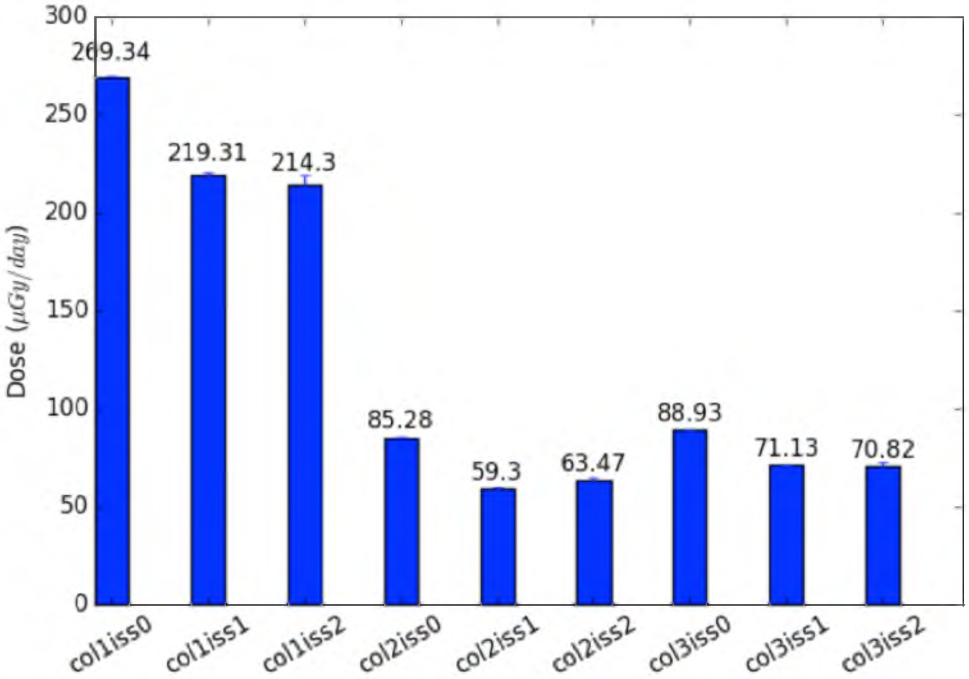

Figure 6.4: GEANT4-computed dose within different ISS geometries models of Columbus module with protons during Solar Maximum in 2001.

Figure 6.5 shows the GEANT4 simulation for Columbus Module 2 with truncated ISS geometry compared to earlier modeling by the DESIRE project and experimental data from DOSTEL experiment and TEPC data onboard the ISS. The SAA DOSTEL, SAA CR39+TLD, and SAA TEPC show equivalent dose rate while passing through the South Atlantic Anomaly. The Columbus Module 3 with truncated geometry tallied 71µGy/day versus the similar earlier work by Ersmark of 79 µGy/day; however, the simulation ran in 4 hours 36 min with a total 9.2 CPU days as opposed to over 40 computation days in the DESIRE project. The equivalent dose was significantly higher for current GEANT4 simulation than experimental results, due to the equivalent dose scorer overestimating the quality factor from incorrectly weighting secondary particles.

The simulation during Solar Minimum for trapped protons in 2009 resulted in a dose rate of 95.2 µGy/day, which fell within measured results from the DOSTEL experiment of 80 µGy/day and TEPC data of 157 µGy/day. Figure 6.6 shows a comparison of the GEANT4 simulation against the measured data from DOSTEL and TEPC and previous simulations by Chavey-McDonald, Ersmark, and ESA by sectoring [81]. Simulations for GCR shown in Figure 6.7 during the same period show close agreement with other studies, which is half the measured value from DOSTEL and TEPC; however, the quality factor for the simulation was 4.3, close to the DOSTEL quality factor of 4.4 and TEPC quality factor of 3.7.

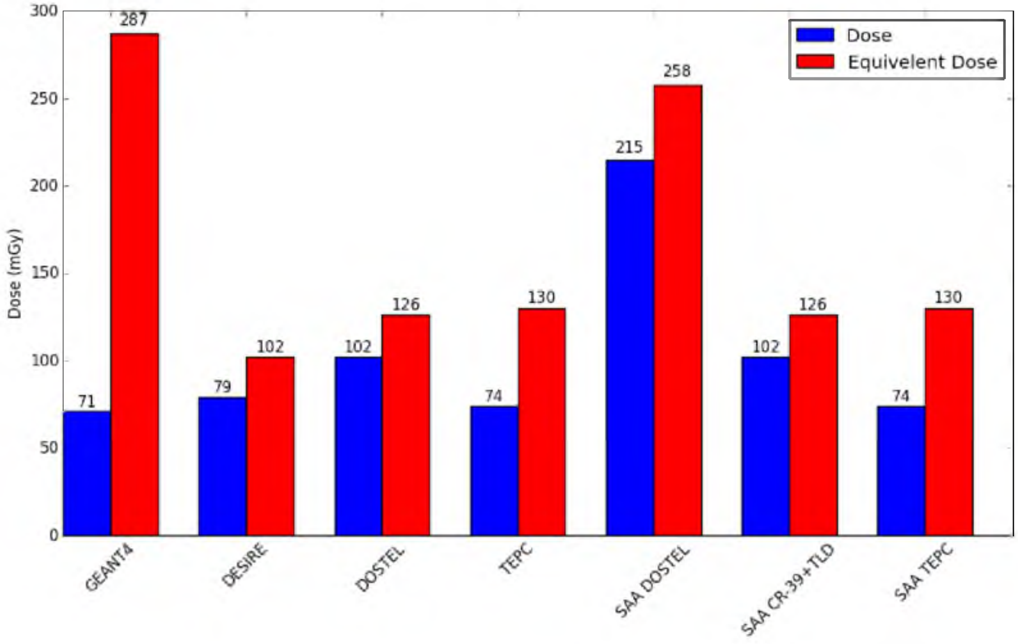

Figure 6.5: GEANT4-computed dose and equivalent dose for GEANT4 simulations versus DESIRE project simulation results and experimental data from DOSTEL, TEPC, and CR-39+TLD for Solar Maximum in 2001.

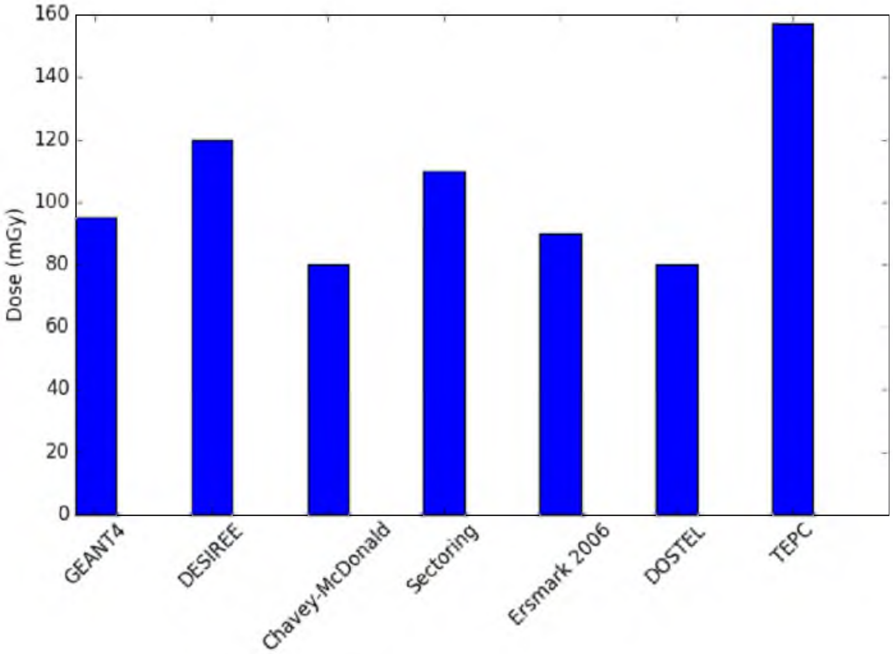

Figure 6.6: GEANT4-computed dose compared with simulations from the DESIRE project, Chavey-McDonald, Sectoring, and Ersmark and experimental data from DOSTEL and TEPC during Solar Minimum in 2009.

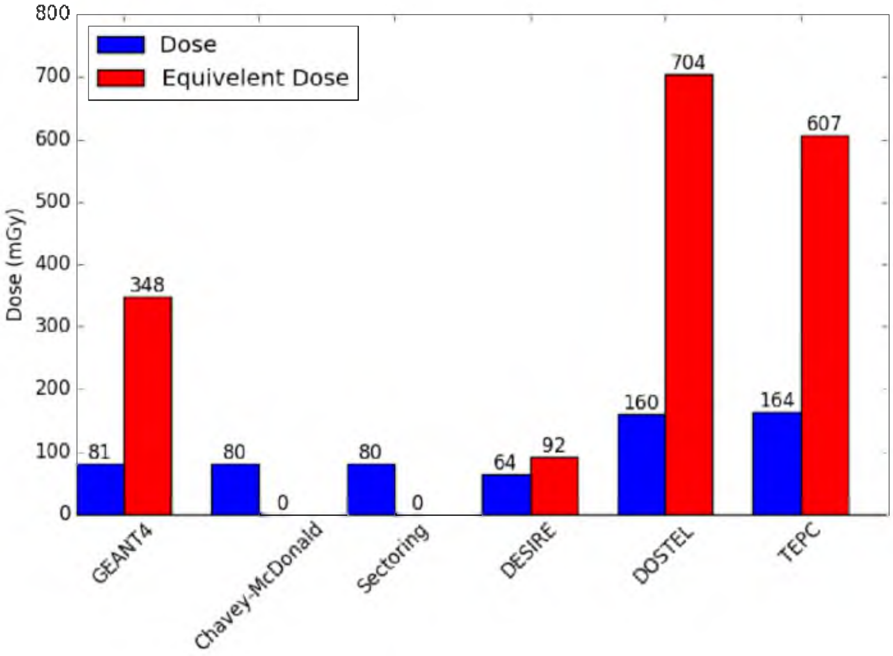

Figure 6.7: GEANT4-computed dose for GEANT4 simulations compared with simulations from the DESIRE project, Chavey-McDonald, Sectoring, and Ersmark and experimental data from DOSTEL and TEPC for GCR at 380 km.

CHAPTER 7

APOLLO MISSIONS

7.1 Introduction to Apollo Missions

The Apollo missions consisted of ten manned mission from October, 1968 to December, 1972, six of which landed on the moon [114]. The missions were from five to twelve days in length, longer than previous space missions, and the only time that mankind has left Low Earth Orbit (LEO), escaping Earth's protective magnetic field. The 363-foot Saturn V rocket powered by Rocketdyne F-2 and J-2 rocket motors launched the Apollo missions into space, which consisted of three stages: a lunar module, command module, and escape tower (see Figure 7.1).

After the third stage burn for Translunar Injection (TLI), the command and service module (CSM) would separate, rotate around, and dock with the lunar module, which then would separate from the third stage and continue on to the moon. The crew launched and lived in the command module for the Translunar flight. During the several days of lunar exploration, the mission commander

Figure 7.1: Saturn V rocket with Saturn V rocket, Command Module, and escape tower at Johnson Space Center, picture by author.

and lunar module pilot would take the lunar lander down to the moon's surface, while the command module pilot remained in orbit around the moon, thus each astronaut experienced a very different radiation dose [115]. The lunar lander had significantly less shielding than the CSM, with the greatest potential for dose during space walks on the lunar surface. Table 7.1 lists the different missions, launch date, duration, and mission description. The longest mission was Apollo 17, followed by Apollo 15, with the shortest mission being the failed Apollo 13.

During the trip astronauts were exposed to trapped radiation belts and increasing levels of GCR radiation as they traveled away from the Earth's magnetic field. Astronaut dose on each Apollo mission varied dramatically, depending on the trajectory and duration of the mission. Each mission had a different trajectory through the Van Allen Belt (VAB), varying the dose. To reduced dose from the VAB, the missions orbited in LEO where the radiation flux was minimal until Translunar

Table 7.1: List of Apollo missions with launch date, duration, and short description [114].

Mission	Craft	Launch Date	Duration	Description
7	Saturn 1B	10/11/1968	10d 20h 9m	Earth orbiting test of Block II CSM
8	Saturn V	12/21/1968	6d 3h 1m	Circumlunar flight and first manned flight of Saturn V. First humans to see backside of moon.
9	Saturn V	3/3/1969	10 d 1h 1m	First manned flight of lunar module, tested rendezvous and dock with CM. EVA test of portable life support system (PLSS).
10	Saturn V	5/18/1969	8d 0h 3m	Dress rehearsal of lunar landing descending to within 15.6km of surface without landing.
11	Saturn V	7/16/1969	8d 3h 19m	On 7/20/1969 landed on moon in Sea of Tranquility.
12	Saturn V	11/14/1969	10d 4h 36m	Landed on moon in Ocean of Storms after two lightning strikes on launch. 2 EVA's recovering portions of Surveyor for return to Earth.
13	Saturn V	4/11/1970	5d 22h 55m	Intended to land at Fra Mauro, aborted after oxygen tank exploded.
14	Saturn V	1/31/1971	9d 0h 2m	Landed Fra Mauro, two EVA's, first material science research in space
15	Saturn V	7/21/1971	12d 7h 12m	Landing at Hadley-Apennine, first "J-series" mission with 3 days on moon, first lunar rover, 3 EVA's.
16	Saturn V	4/16/1972	11d 1h 51m	Landed in Descartes Highlands, 3 Lunar EVA's
17	Saturn V	12/7/1972	12d 13h 52m	Landed at Taurus-Littrow, first night launch, 3 lunar EVAs

Injection (TLI), at which time the Apollo spacecrafts passed quickly through the radiation belts at inclinations greater than 30°, greatly reducing dose [9]. The GCR dose was relatively constant after leaving the Earth's magnetic field, dependent only on the duration of the mission. The greatest concern for missions were SPEs, since the missions occurred during Solar Maximum. A dedicated network of radio and optical telescopes, the Solar Particle Alert Network (SPAN), observed the Sun 24 hours a day to watch for SPE events. In case of a solar storm, the astronauts would follow emergency procedures, returning quickly to the added protection of the command module from the lunar surface and using detectors described in Section 5.4 to find the lowest dose location within the capsule. For the Apollo missions, the maximum operational dose was 50 rads to blood-forming organs and 400 rads to skin, which was significantly more than measured on any mission [9, 116]. Table 7.2 shows the recorded dose rate for each Apollo Mission; notice the order of magnitude higher dose for Apollo 14 mission.

This section explores the Apollo 11 mission, since it was the first mission to land on the moon, and the Apollo 14 mission due to the magnitude higher dose rate. For both missions, this chapter details simulations of trapped proton, trapped electron, and GCR dose, along with dose rates for potential SPEs. Also simulations of dose to organs within a human phantom were made for comparison.

7.2 GEANT4 Geometry Model of Apollo Command Module

North American Aviation built the Command Service Module, which consisted of the Command Module and Service Module. North American Aviation merged with Rockwell-Standard, which eventually was bought by Boeing. Unfortunately during the mergers, Boeing did not receive custody of the technical schematics for the CSM modules [117], thus only partial schematics and drawings

Table 7.2: Astronauts absorbed dose during Apollo Missions with duration and mean dose rate [8].

Apollo Mission	Duration (hours)	Absorbed Dose (mGy)	Mean Dose Rate (μG/day)
7	260.1	1.6	150
8	147	1.6	260
9	241	2	200
10	192	4.8	600
11	194	1.8	220
12	244.5	5.8	570
13	142.9	2.4	400
14	216	11.4	1,270
15	295	3	240
16	265.8	5.1	460
17	301.8	5.5	440

are available from NASA's technical database.

The Service Module (SM) is a cylinder with a diameter of 154" mounted below the crew compartment composed of an inner and outer concentric core divided into six bays consisting of mostly cryogenic tanks. One-inch aluminum honeycomb made up the outer shell with an additional .020" to .155" coating of cork for thermal protection [118]. The stainless steel honeycomb was made up of two 1.9 mm plates with a honeycomb cell of 5 mm and .02 mm thickness steel [119]. Since the Service Module (SM) only shielded radiation from the aft section of the Command Module, where the heat shield is thicker and provides more protection, the geometry models did not include the SM.

On launch, a boost protective cover of fiberglass and cork covered the Command Module (CM) to protect the craft from heat during launch due to aerodynamic drag. The boost protective cover weighed around 700 pounds, being ejected shortly after launch at an altitude of 295,000 feet, thus the model does not include the boost protective cover.

The Command Module (CM) weighed 5809 kg, with a total volume of 15.8 m^3 and pressurized volume of 10.4 m^3 made of an inner and outer shell. The inner shell was made of two aluminum plates with a honeycomb in between, and the outer shell of two steel plates with a honeycomb in between. In the middle of the shells is a 3.5lb/ft^2 low-density fibrous insulation TG15000. Outside the outer shell is an ablative heat shield. Up to 27 layers of Kapton coated with a thin deposit of aluminum and oxidized silicon monoxide served for thermal insulation, making up the outer layer of the craft. More Kapton (Mylar) was used on Apollo 17 than earlier crafts, with each craft varying in thickness. The CM consisted of three basic volumes with separate heat shields welded together: aft section, central crew compartment, and forward section. The forward section was protected by a heat shield that was jettisoned 295,000 feet before splashdown to expose the parachute gear [120, 121].

The stainless steel outer structure was PH14-8M0 alloy with a thickness of 2.7" at the aft head shield to a thickness of .9" at the forward access tunnel. The structure was made of two thin steel sheets of 1.9 mm sandwiching a steel honeycomb with a 5 mm diameter and .02 mm thickness steel honeycomb wall [119]. The inner structure consisted of a welded aluminum inner skin and outer face sheet sandwiching an adhesively bonded aluminum honeycomb core with thickness of 1.5" at the base to about .25" at the forward access tunnel. The aluminum honeycomb was similar to 3/16" aluminum 5052 with a lighter density of .0497g/cm^3 due to being a honeycombed structure. The inner sheet of the structure used Pyralin as a coating. The forward hatch is 30" in diameter covered with a half-inch of insulation and aluminum foil, which was probably Kapton [122]. The craft had 13" square windows with two side, two rendezvous, and a hatch window. The windows had an inner window of tempered silica glass 1/4" thick double panes separated by 1/10" and an outer window of amorphous-fused silicon single pane 7/10" thick [123]. The cockpit throughout also contains aluminum protection panels, aluminum equipment racks, cupboards, and control panels. The Aft Compartment contained 24 bays with 24 frames of tanks and equipment [120].

Aeronca Manufacturing Company of Middletown, Ohio made the heat shielding, thermal protection system (TPS). The aft portion of the TPS is 2" thick, and the forward portions are 1/2", with a total weight of 3,000 lbs. The TPS had several layers made of a pore seal ablative material, moisture barrier (white reflective coating), and thermal blanket of silver Kapton (Mylar). The TPS surrounding the craft used an ablative material Avco 5026-39G, which consisted of an epoxy-novalac resin reinforced with phenolic micro-balloons and quartz fibers. The Avco had a density of 31-35 lb/ft^3. The phenolic honeycomb matrix was bonded with HT-424 adhesive to the stainless-steel shell. The Avco ablator was caulked into the individual honeycomb cells with a hypodermic device [124].

The Command Module had a maximum diameter of 154" by 137" tall using a frustum shape with a blunt curved bottom. The curved bottom created a shockwave on reentry, which trapped a layer of compressed gas in front of and around the craft to protect from the heat of reentry. Thus for the geometry model, the frustrum shape of the craft was broken into four sections: central heat shield, aft heat shield, forward heat shield, and top hatch. Each consisted of multiple layers: Kapton, ablator, stainless steel plates and honeycomb, insulation, aluminum plates and honeycomb, interior, and equipment racks. Each material for the craft was added to the GDML file by chemical composition, see Appendix A.4 for the complete list of materials in the GDML. The stainless steel honeycomb and aluminum honeycomb were made by creating a solid material of the steel or aluminum alloy with a density that matched the honeycomb, since the shielding effect of the solid material with correct density would be similar to building the complete honeycomb made up of many individual components requiring large amounts of memory for the extra detail.

The Command Module used a polycone structure for the central heat shield combined with Boolean subtraction operation to a spherical bottom with a diameter of 154" to form the aft heat shield. The radius of the sphere for the aft heat shield was found by taking the height of the spherical section 20" and subtracting from the radius of the sphere. This was then solved by using right triangle geometry, with the radius (r) minus 20" representing one side of a triangle with half the 154" diameter representing the other shown in Figure 7.2 and Equation 7.1 below.

$$r^2 = \left(\frac{154}{2}\right)^2 + (r - 20)^2 \tag{7.1}$$

The polycone central heat shield extended to the top forward hatch, narrowing towards the top. The top hatch was made of a tube with the correct thickness for each layer placed inside a logic volume of the forward hatch. The forward heat shield was also made of a polycone that fit on top of the central polycone heat shield. The inside of the craft was filled with air along with either 15

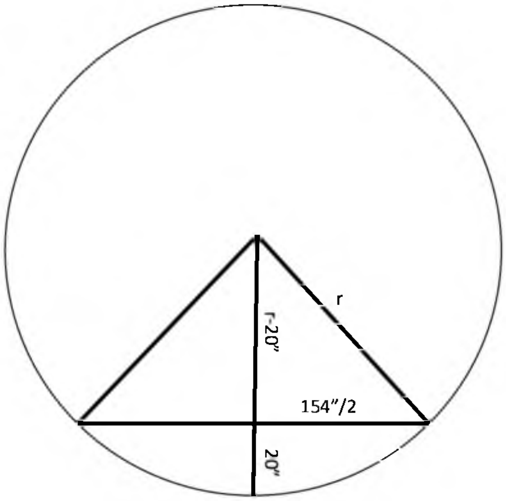

Figure 7.2: Geometrical representation used to calculate radius (r) of spherical aft heat shield of Apollo Command Module.

ICRU spheres equally spaced throughout the capsule as shown in Figure 7.3 or a human phantom as detectors, depending on the simulation.

Since details of the top forward heat shield and hatch were not available, picture analysis using LogerPro software was used to determine dimensions for the top hatch by defining known measurements in images of a CM at the Smithsonian and then measuring unknown dimensions with the software. The dimensions were input to a custom-built Excel worksheet, which created the physical volumes and logic volumes. The volumes were then copied into a GDML file with the materials. In GEANT4, the GDML file was tested using the geometry test to find overlaps, adjusting position references until no more overlaps were found (see Appendix A.4 and A.5 for complete Apollo Command Module Geometry files).

Since the exact dimensions and specifications of interior components were unknown, two models of the Apollo Command Module were built. The first model just contained the hull layers of the capsule and pressure vessel. The second geometry model added an equipment rack inside the interior of the capsule made of aluminum roughly 12" thick to more correctly model the added shielding from the racks, similar to the technique used in the Columbus 2 and 3 model. The mass of the Apollo CM 1 model was found using ASCIITree tool from GEANT4 in verbose 4 mode, which when the volume is drawn gives the calculated volume and mass of each volume, using the shape and material density of each volume. Apollo CM 1 had a mass of 1566.13 kg, which was far less then the 5809 kg of the actual CM; therefore, the Apollo CM 2 model added an equipment rack of aluminum with a density equal to the difference in mass divided by the volume of the equipment racks. Thus the Apollo CM 2 mass correctly matched the CM mass and extra shielding from the interior racks. Figure 7.3 shows

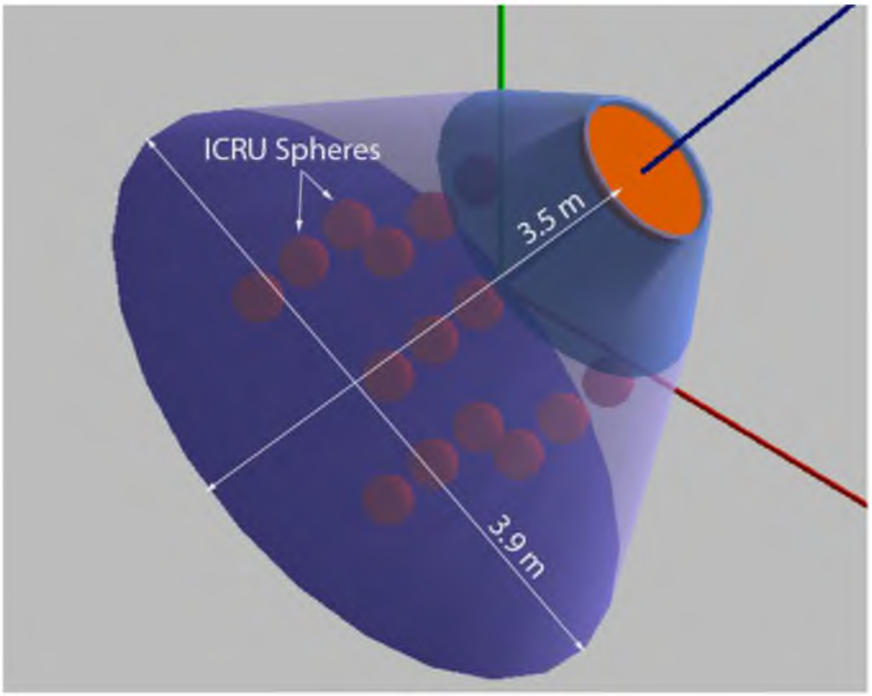

Figure 7.3: Apollo CM Module geometry in GEANT4 with 15 ICRU spheres inside.

the completed Apollo CM module geometry in GEANT4 with ICRU spheres inside.

7.3 Recreating Apollo 11 and 14 Trajectory

The Apollo spacecraft after launch orbited around the Earth for a brief period of around an hour to check systems before the Translunar Injection (TLI) burn. After vehicle checkouts, the Command Module fired the J-2 engine of the third stage for approximately 350 seconds, increasing the velocity to escape Earth's gravity and start a trajectory towards the moon [125]. Table 7.3 shows the Apollo mission TLI data with the necessary information for calculating the trajectory of Apollo 11 and 14 lunar transits, including the passage through the Van Allen Radiation belt [125–127]. The TLI data give required information to find the six orbital elements to describe the trajectory, including Semimajor Axis (a), Eccentricity (e), Inclination (i), Argument of Periapsis (ω), Time of Periapsis Passage (T), and Longitude of Ascending Node (Ω) [128].

The semimajor axis describes one-half the length of the major axis of an ellipse forming the orbit. The eccentricity describes the deviation from a circle and is the distance between foci divided by the major axis length. The inclination is the angle between the outward-projected Earth's equator and the spacecraft's orbital plane, with an inclination of 90° representing a polar orbit. The ascending node is the point when the spacecraft passes from the southern hemisphere to the northern hemisphere of the Earth for the spacecraft's orbit. Periapsis is the angle from the ascending node to the point

Table 7.3: TLI data for Apollo 11 and 14 missions from LEO.

	Apollo 11	Apollo 14
GET	2:50:13	2:34:33
KSC Date	7/16/69	1/31/71
GMT Date	7/16/69	1/31/71
KSC Time	12:22:13	18:37:35
GMT Time	16:22:13	23:37:35
Altitude (ft)	1,097,229	1,090,930
Altitude (nm)	180.581	179.544
Earth-Fixed Velocity (ft/s)	34,195.6	34,151.5
Space Fixed Velocity (ft/s)	35,545.6	35,511.6
Geocentric Latitude (deg N)	9.9204	-19.4388
Goedetic Latitude (deg)	9.983	-19.554
Longitude (deg E)	-164.8373	141.7312
Flight Path Angle (deg)	7.367	7.48
Heading Angle (deg)	60.073	65.583
Inclination (deg)	31.383	30.834
Descending Node (deg)	121.847	117.394
Eccentricity	0.97696	0.9722
Characteristic Energy (C3) (ft^2/sec^2)	-14,979,133	-18,096,135

closest in orbit to Earth, with the time of Periapsis giving the time of the spacecraft passing the point of Periapsis. The true anomaly defines the location with respect to perigee. The longitude of the ascending node is the degrees from Earth's zero longitude, which is the point where the prime meridian passes at midday during the Vernal Equinox [128].

From the TLI data, the radius of the Fischer Ellipsoid of 1960 is found by taking the equatorial radius of Earth (a), the polar radius of Earth (b), and the geocentric latitude (ψ) as shown:

$$R = \frac{ab}{\sqrt{(b\cos\psi)^2 + (a\sin\psi)^2}} \tag{7.2}$$

The radius vector of the Apollo mission at TLI is then the radius of the Fischer Ellipsoid plus the altitude. The perigee (R_p) and apogee (R_a) radii are found based on the flight angle (ϕ) and C, where C is given in terms of the Gravitational Constant (G), mass of Earth (M), radius vector (r), and velocity (v) as shown in the following equations:

$$\left(\frac{R_{a/p}}{r}\right) = \frac{-C \pm \sqrt{C^2 - 4(1-C)(-\cos^2\phi)}}{2(1-C)} \tag{7.3}$$

$$C = \frac{2GM}{rv^2} \tag{7.4}$$

The eccentricity of the orbit to the moon is then given by:

$$e = \sqrt{\left(\frac{rv^2}{GM} - 1\right)^2 \cos^2\phi + \sin^2\phi} \tag{7.5}$$

The true anomaly (n) of the orbit is then:

$$n = \tan^{-1}\left(\frac{\left(\frac{rv^2}{GM}\right)\cos\phi\sin\phi}{\left(\frac{rv^2}{GM}\right)\cos^2\phi - 1}\right) \tag{7.6}$$

The semimajor axis of the orbit is the average of the perigee and apogee radii. The orbital longitude (l) is given in terms of the TLI inclination point (l_{geo}) and geocentric latitude of TLI point (d_{geo}) from the TLI data.

$$l = \sin^{-1}\left(\frac{\sin l_{geo}}{\sin d_{geo}}\right) \tag{7.7}$$

The equatorial longitude (a) is found in terms of the orbital longitude (l) from equation 7.7 and inclination of the orbital plane (i).

$$a = \tan^{-1}(\tan l \times \cos i) \tag{7.8}$$

The argument of perigee (w) is the orbital longitude (l) minus the true anomaly (n).

$$w = l - n \tag{7.9}$$

The ascending node's geographic longitude is the geographic longitude of TLI minus equatorial longitude of TLI (a). The ascending node's celestial longitude (W) is the local sidereal time (lst) at geographic longitude at TLI time, found by adding the geographic longitude at TLI to the Greenwich Mean Sidereal time. The final orbital element is the time of perigee passing found by the TLI time minus the time between the true anomaly at TLI and the last perigee [128–130].

An Excel spreadsheet was created following the previous steps to calculate the six major orbital elements for Apollo 11 and Apollo 14 shown in Table 7.4. The spreadsheet then calculated the location of the spacecraft at five minute intervals during the first few hours while traveling through the

Table 7.4: Calculated major orbital elements for Apollo 11 and 14.

	Apollo 11	Apollo 14
Semi-Major Axis (m)	295359165	245245002
Eccentricity	0.977	0.972
Inclination	19.3°	-40.5°
Argument of Perigee	4.65 °	-55.41°
Longitude of Ascending Node	358.4°	302.9°
Time of Perigee Passage (GET)	16:19:31	23:34:49

trapped radiation belts, after which the spreadsheet calculated the spacecraft location at 30-minute intervals for the remaining duration of translunar transit for Apollo 11 and 14.

The location of the Apollo spacecraft is then found as a function of time (t) after TLI until reaching the moon as function of equatorial longitude and latitude by finding the true anomaly at the time point. To find the true anomaly at time (t), first the Mean Anomaly is found by multiplying the time by the true anomaly at TLI as shown:

$$M = t \times n \tag{7.10}$$

Then the eccentric anomaly (E) is found by iterating over each interval with the mean anomaly and eccentricity as shown:

$$E = M - e \sin E \tag{7.11}$$

The true anomaly at the point is given in terms of the eccentricity anomaly (E) and eccentricity (e).

$$n = cos^{-1}\left(\frac{\cos E - e}{1 - E\cos E}\right) \tag{7.12}$$

The orbital longitude (l) is then the true anomaly (n_t) plus the argument of perigee (w).

$$l = n_t + w \tag{7.13}$$

The equatorial longitude is then found by converting orbital longitude (l) and inclination (i).

$$a = \tan^{-1}(\tan l \times \cos i) \tag{7.14}$$

The celestial longitude is then the equatorial longitude plus the longitude of ascending node. The equatorial latitude is then found below [128–130].

$$d = \sin^{-1}(\sin(l) \times \sin(i)) \tag{7.15}$$

Next the equatorial latitude and longitude are converted to X, Y, and Z Cartesian coordinates,

$$X = (N + h)\cos\phi\cos\lambda \tag{7.16}$$

$$Y = (N + h)\cos\phi\sin\lambda \tag{7.17}$$

$$Z = \left[N\left(1 - e^2\right) + h\right]\sin\phi \tag{7.18}$$

N is the radius of curvature in the prime vertex.

$$N = a\left[1 - f(2 - f)\sin^2\phi\right]^{-1/2} \tag{7.19}$$

The flattening (f) is given by the IAU 1964 reference ellipsoidal of .0033529 along with the semi-major axis (a) of 6378160 m. The semiminor axis (b) is found by rearranging equation 7.20 for flattening to solve for b as shown in 7.21

$$f = \frac{(a-b)}{a} \tag{7.20}$$

$$b = a - af \tag{7.21}$$

The first eccentricity (e) is then [12]:

$$e = \frac{\sqrt{a^2 - b^2}}{a} \tag{7.22}$$

After calculating the location at the time of entering lunar orbit, the results were checked with an online database of moon location to verify correct longitude and latitude, and the latitude and longitude to Cartesian Coordinates transformations were checked with an online calculator to find the relative error in trajectory calculations shown in Table 7.5.

Since the relative errors for distance to Earth, latitude, longitude, and Cartesian coordinates were small at entering lunar orbit, the trajectories from the TLI data match closely to the actual flight paths. Figure 7.4 shows the trajectories of Apollo 11 next to the Apollo 14 trajectory; notice the change in starting Earth location and final moon position, which resulted in different paths through the VAB.

SPENVIS Orbit generator used the Cartesian trajectory coordinates with the upload trajectory file to generate ephemeris data for each mission to calculate radiation fluence. The trajectories were converted into a free trajectory file for SPENVIS by adding year, date, month, hour, minutes, seconds, and coordinates with tab delimitation and defining the coordinate system as Geocentric Equatorial Inertial System (GEI), see Appendix C for Apollo trajectory files [12].

Table 7.5: Calculated final location of Apollo 11 and 14 at moon for distance from Earth, latitude, longitude, and x, y, z coordinates compared with online lunar location databases with relative error.

	Apollo 11 Database	Calculated	Error	Apollo 14 Database	Calculated	Error
Distance (km)	$3.95\text{X}10^8$	$3.82\text{X}10^8$	3.20%	$3.84\text{X}10^8$	$3.94\text{X}10^8$	2.59%
Latitude °	2.36	2.27	3.59%	2.63	2.69	2.09%
Longitude °	174	175	0.23%	62.8	64.8	3.03%
X (km)	$-4.05\text{X}10^5$	$-4.05\text{X}10^5$	0.00002%	$1.52\text{X}10^5$	$1.52\text{X}10^5$	0.10%
Y (km)	$3.41\text{X}10^4$	$3.41\text{X}10^4$	0.003%	$3.23\text{X}10^5$	$3.23\text{X}10^5$	0.10%
Z (km)	$1.38\text{X}10^4$	$1.38\text{X}10^4$	0.007%	$1.81\text{X}10^5$	$1.82\text{X}10^5$	0.39%

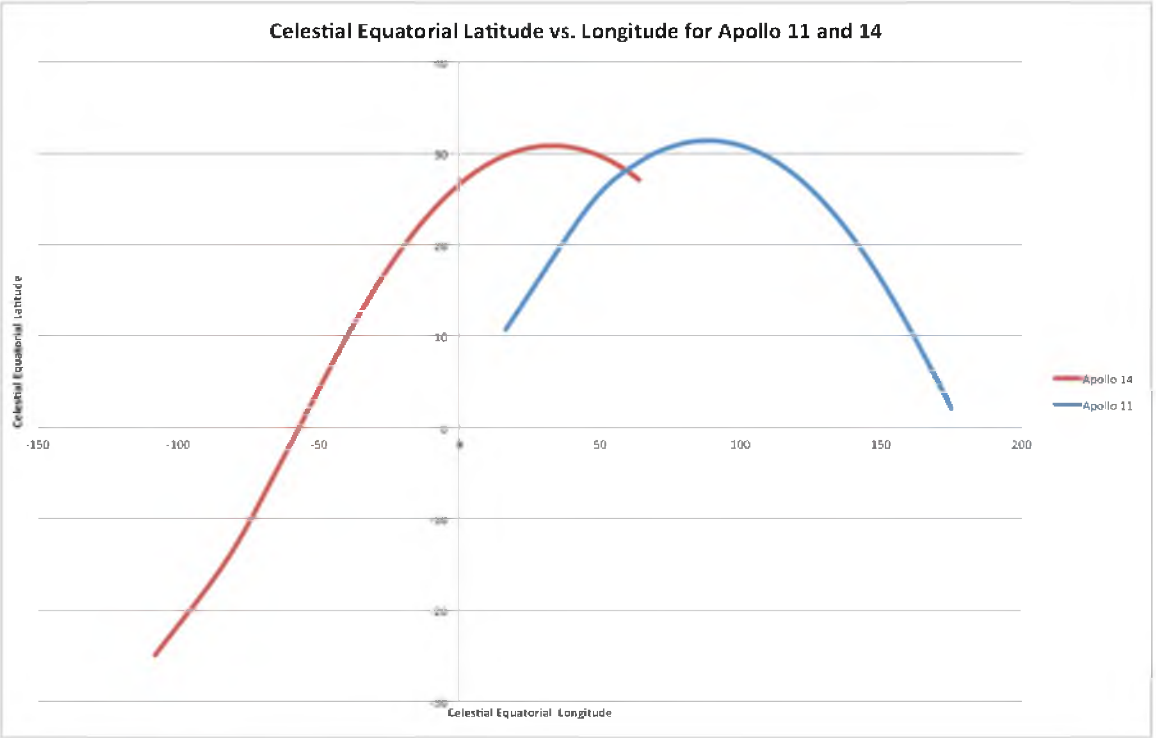

Figure 7.4: Apollo 11's and 14's lunar trajectory through VAB plotted as celestial equatorial latitude versus celestial equatorial longitude.

7.4 Space Radiation Spectra for Apollo Missions

In SPENVIS's Radiation Sources and Effects module, the AP-8 and AE-8 models generated the trapped proton and electron fluence. The fluence was trajectory dependent and only affected the spacecraft for the short outbound and inbound time of a few hours. Figure 7.5 shows a portion of the outbound Apollo 11 spacecraft trapped proton flux from AP-8 in GEO coordinates for nine hours after TLI. The highest dose shown was very brief, with flux reducing greatly with distance.

Figure 7.6 shows the total proton fluence for Apollo 11 and 14 from the AP-8 model versus proton energy in MeV. Apollo 14 had a higher low-energy proton fluence, which is easily attenuated, and a lower high-energy fluence, thus the trapped proton dose is lower for Apollo 14 then Apollo 11. Figure 7.7 shows the electron fluence for Apollo 11 and 14 from the AE-8 models. The electron fluence for Apollo 14 was greater than Apollo 11; however, the Apollo hull easily stopped electrons, resulting in very little dose to Apollo astronauts.

Since the Sun was in Solar Maximum during Apollo 11 in 1969 and Apollo 14 in 1971, the Nymmik et al. model in SPENVIS was used to generate the GCR fluence for particles from hydrogen through iron during the mission epoch and solar cycle. The coordinates used were for free space at one astronomical unit, since after leaving the Earth's magnetic field the GCR dose would be the highest and constant. SPENVIS outputs flux for GCR in particles/cm^{2}s, thus the normalization

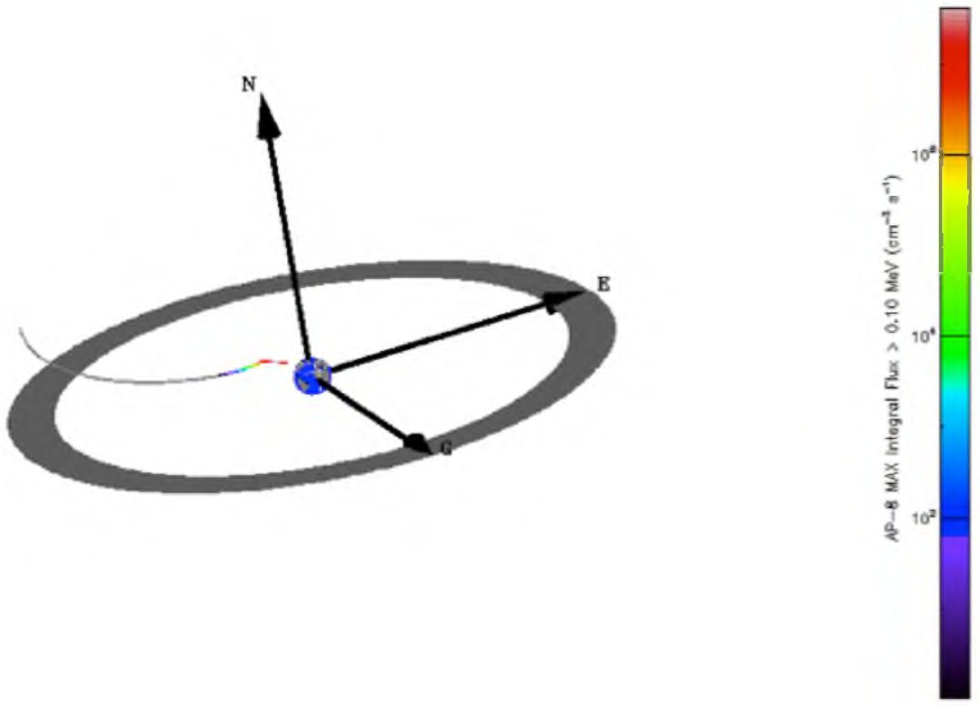

Figure 7.5: Apollo 11 trajectory in GEI Coordinates from Earth through the trapped radiation belt with proton integral fluence from AP-8 model from SPENVIS [25].

factor was multiplied by the total mission duration in seconds to find the total mission fluence for the craft. Figure 7.8 shows the integral flux and Figure 7.9 shows the differential flux for selected ions from hydrogen through iron. Both show very similar fluxes for all isotopes, with a slight increase for low-energy hydrogen ions for Apollo 14. Hydrogen ions had the highest fluence, thus largest contribution to dose. GCR results for both missions result in comparable dose rates; however, since Apollo 14 was a longer mission, the total dose is higher.

The Apollo missions occurred during solar cycle twenty Solar Maximum, which is shown in Figure 7.10 by the number of sunspots versus date, with the peak in 1969 [131]. The probability of a SPE is higher during Solar Maximum, thus the Apollo missions were more likely to experience a SPE. On August 4th, 1972, one of the largest recorded SPE occurred, knocking out long-distance communications on Earth, which was in the time period between the Apollo 16 and 17 missions. The flare resulted in about 70% of the total fluence during solar cycle 20 [132]. A lunar mission during the extremely large anomalous event would have resulted in doses beyond mission limits, resulting in radiation sickness. The only detected SPE by instrumentation during the program was

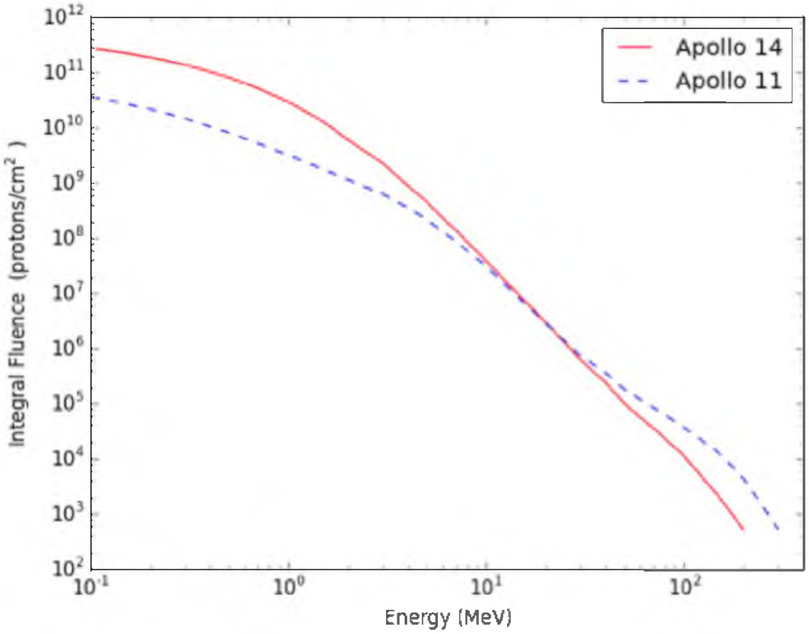

Figure 7.6: Calculated Apollo 11 and 14 trapped protons integral fluence from AP-8 model.

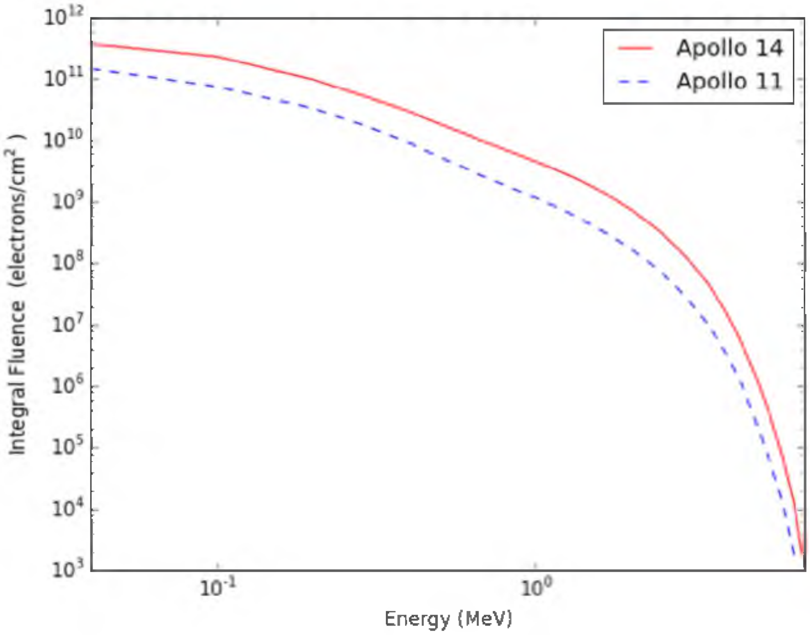

Figure 7.7: Calculated Apollo 11 and 14 trapped electrons integral fluence from AE-8 model.

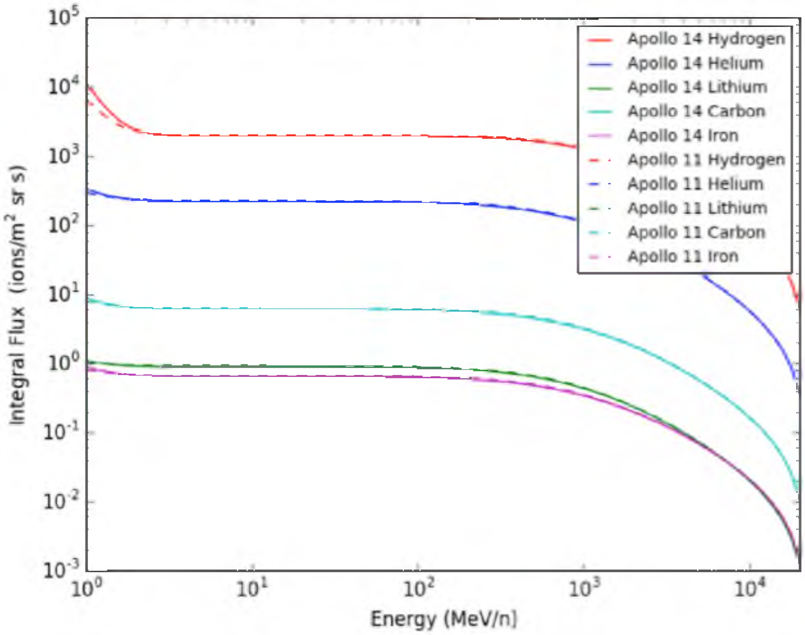

Figure 7.8: Calculated integral flux for selected GCR ions through iron for Apollo 11 and 14 missions.

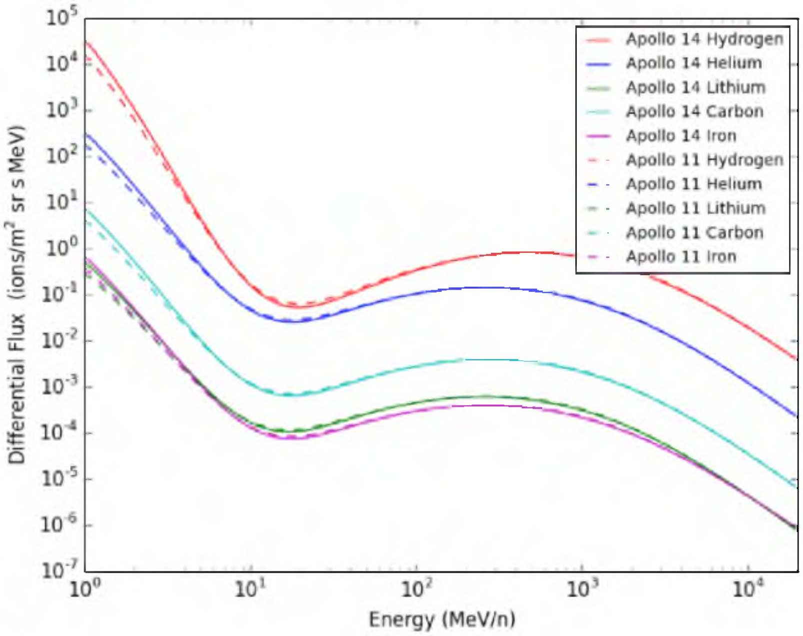

Figure 7.9: Calculated differential flux for selected GCR ions through iron during Apollo 11 and 14 missions.

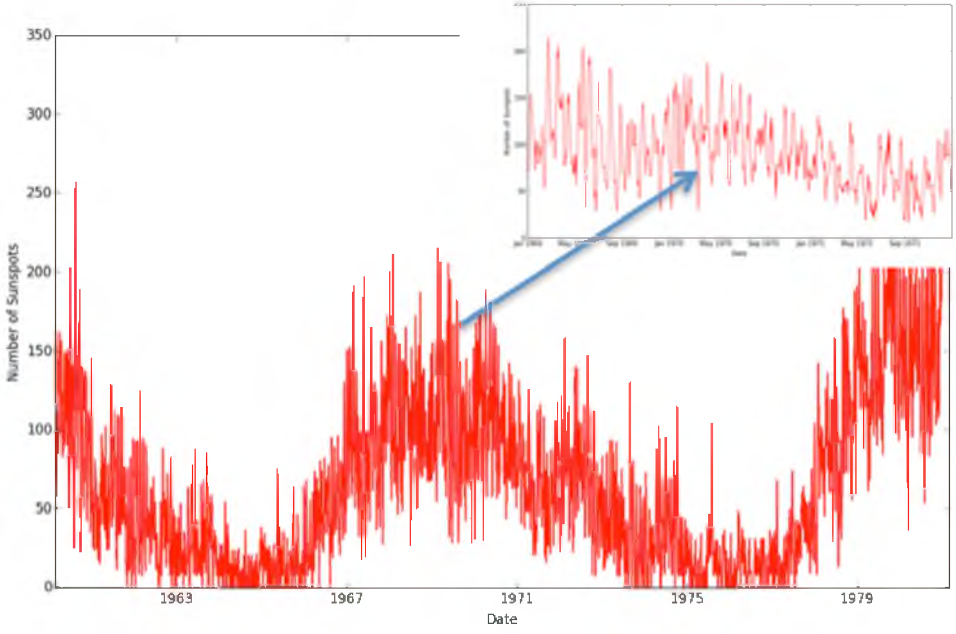

Figure 7.10: Number of sunspots versus date during Apollo missions [131].

Apollo 12, which detected a small SPE externally, with no increase in radiation monitors inside the crew capsule [133].

Before and during the Apollo 14 mission occurred, five major solar flares ranked on the "Experimental comprehensive solar flare indices for certain flares, 1970-1974" UAG-52 report [134]. Table 7.6 shows a list of the solar flares before and during the Apollo Mission, the two proceeding Apollo 14 mission launch were large flares; however, the Apollo 14 mission did not detect SPE events from the flares. Even though there was no known SPE, the solar flares could have indicated an increased flux of solar radiation, thus simulations were run for all five major examples of SPE events in SPENVIS: ESP-PSYCHIC Total Fluence, ESP-PYSCHIC Worst Case, JPL, King et al., and Rosenqvist et al. Figure 7.11 shows a comparison of the differential flux for the five possible scenarios for SPE during Apollo 14 mission at one astronomical unit in free space, outside Earth's

Table 7.6: Solar flares before and during Apollo 14 mission from UAG-52 report [134].

Begin YYMMDD	ID#	HHMM UT	Lat	Long	H-a Imp	McMath Plage	Profile abcde	Index
710121	71007	1320-1353	19	4	SN	11128	30220	7
710124	71008	2308-2530	18	49	2B	11128	22333	13
710205	71009	0524-0558	-9	-13	SN	11145	10	1
710205	71009	0533-0553	3	43	SN	11137	10	1
710205	71010	1424-1448	10	75	SN	11140	30	3

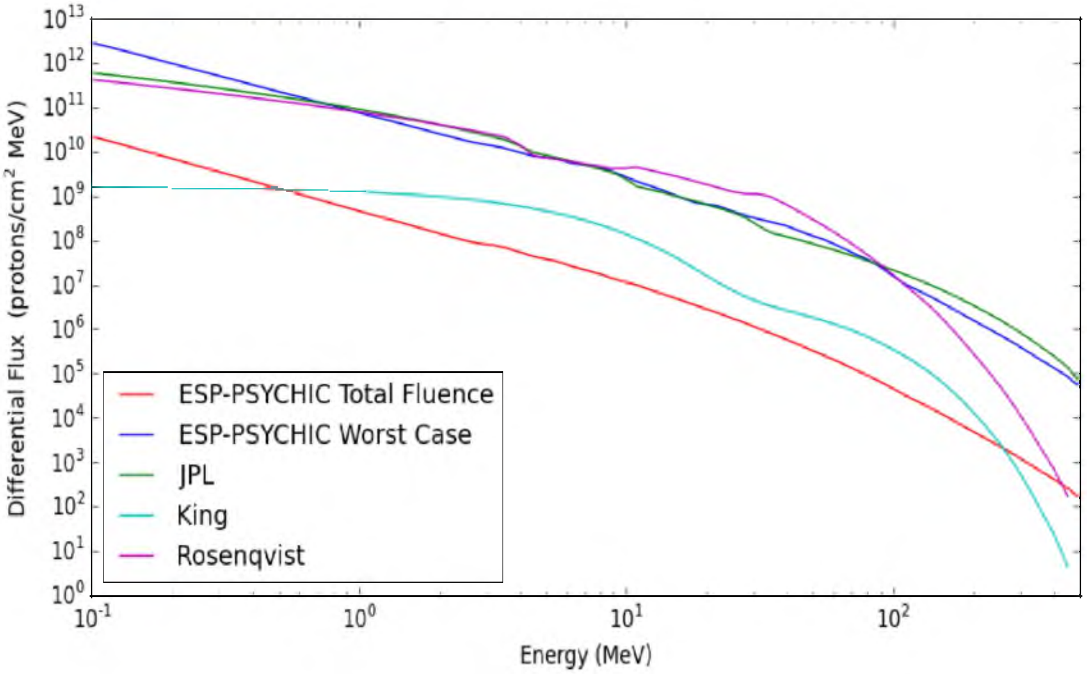

Figure 7.11: Calculated differential flux vs. energy for possible SPE event scenarios in free space during Apollo 14.

magnetosphere during lunar transit. The Rosenqvist model has the highest flux at high energy, and the ESP-PYSCHIC Worst Case model has the highest flux at low energy. The King and ESP-PSYCHIC Total Fluence have the lowest flux of all the models.

7.5 Apollo 11 and 14 Simulated Mission Dose and Equivelent Dose

Simulations of the trapped proton and electron dose showed double the dose for CM Model 1 than for Model 2 due to the added shielding from equipment racks in the hull of CM Model 2 reducing dose. The proton dose for Apollo 11 was higher than electron dose; however, for Apollo 14 the electron dose was higher due to the longer trajectory though the outer trapped electron radiation belt. Figure 7.12 shows the trapped proton and electron dose for both missions with error bars for the relative error. The small error bars show the relative error of the simulations, which was well under 5% for each simulation.

The GCR doses for all ions from hydrogen through iron were simulated individually using both CM models during Solar Maximum in μGy/day, which was then multiplied by the mission duration for the total dose. The total dose from all GCR ions for Apollo 14 for CM model 1 was 1.46 mGy and less for CM model 2 of .37 mGy. This dose was higher than for Apollo 11 due to the day longer mission. The total dose from all ions for Apollo 11 was 1.30 mGy for CM Model 1 and .41 mGy for CM Model 2. The GCR dose for CM model 1 was less than for CM model 2 due

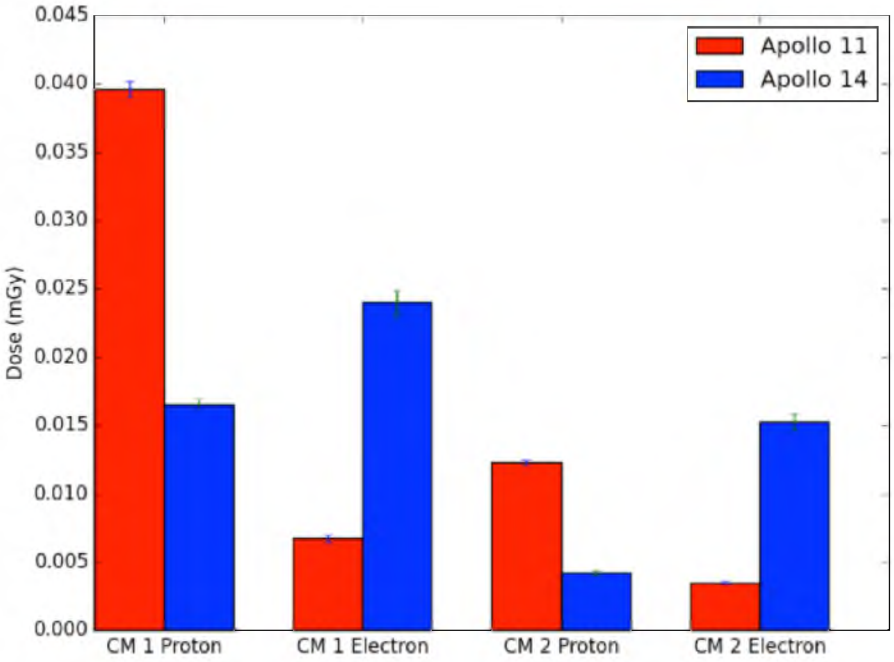

Figure 7.12: GEANT4-calculated dose from trapped protons and electrons for Apollo 11 and 14 for both CM 1 and 2 models.

to increased shielding from the added equipment racks; however, usually increased shielding for spacecraft increases GCR dose due to secondary radiation from the high-energy particles, so the results were unexpected. Table 7.7 shows the dose and simulation relative error for several important isotopes with the total dose. The hydrogen ions resulted in the highest dose, with helium ions having about a fourth as much dose. Carbon, oxygen, and iron also added to the total dose. Iron was anticipated to have a large affect on the total dose because it was the heaviest ion; however, the iron dose was relatively small compared with carbon and oxygen. Figure 7.13 shows the dose from each ion for both CM model 1 and 2 on a logarithmic scale. During simulations with high-energy heavy

Table 7.7: GEANT4-calculated GCR dose in μGy/day for several ions with relative error for Apollo 11 and 14 by CM model.

	CM Model 1		CM Model 2	
Ion	Dose (μGy/day)	Relative Error	Dose (μGy/day)	Relative Error
H	121.2	1.26%	37.5	1.07%
He	37.5	1.01%	7.9	1.09%
C	2.2	1.20%	0.29	2.22%
O	2.1	1.17%	0.26	2.88%
Fe	0.34	1.20%	0.02	7.06%
Total	162.6	1.17%	46.5	2.86%

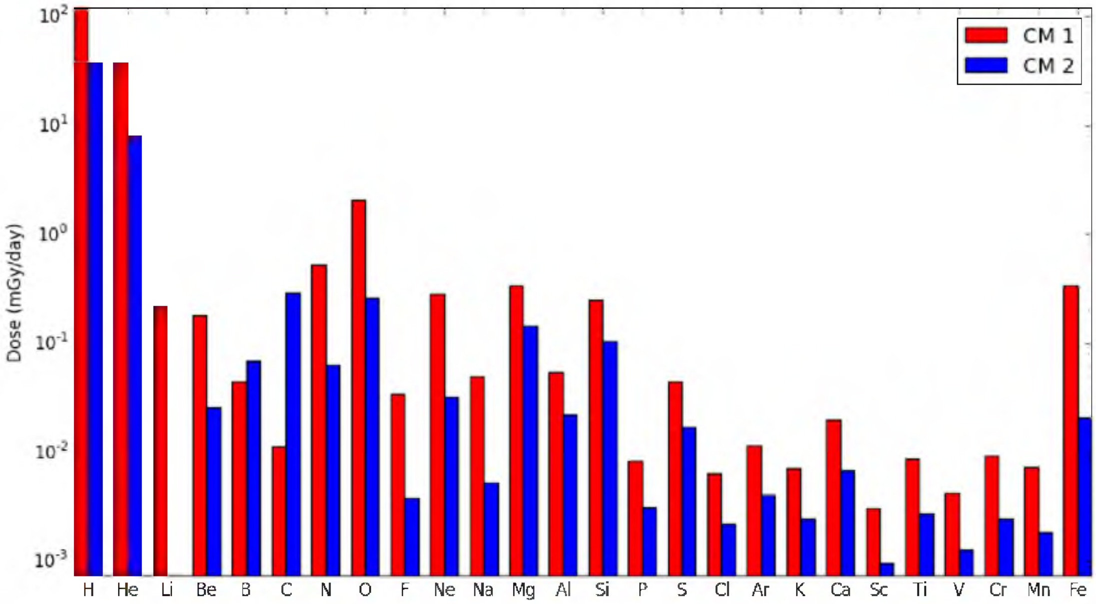

Figure 7.13: GEANT4-calculated GCR dose in μGy/day by ion through iron for CM model 1 and 2 during the Apollo missions in Solar Maximum.

ions in the GPS particle gun, often particles would cause a geometry exception warning message of "exceeding a distance to out" due to a bug in GEANT4, thus GCR results need revising after the GEANT4 collaboration has resolved the bug.

The dose from the SPEs was significantly below the established mission maximum dose of 4 Gy for astronauts within the CM; however, the dose would be significantly higher for astronauts within the thinner lunar module shielding or on EVA. The CM model 2 with additional shielding from equipment racks greatly reduced by over a third the dose from the simplified model 1. Contrary to popular misconception, the predicted SPEs would not be fatal, although the dose would be high but likely below the limit for radiation sickness. Table 7.8 shows the dose from the five models of SPEs for both CM models 1 and 2. The relative error for simulations again was very low, with the standard deviation across the ICRU spheres below one order of magnitude less, thus showing a variation within the capsule, but far below the average dose. The highest dose was from the JPL model, which was significantly higher than the dose from ESP-PYSCH Worst Case Model. The King model predicting a normal SPE during solar cycle twenty of the Apollo missions showed the smallest increase to overall dose.

Table 7.9 shows the summation of simulated dose for Apollo 11 and 14 using the CM model 1 for trapped protons, trapped electrons, and GCR compared with the measured mission total. The simulated total for Apollo 11 with CM model 1 was within 23% relative error, which is within error measurements in the radiation models; however, simulated Apollo 14 was an order of magnitude less

Table 7.8: GEANT4-calculated SPE dose to Apollo astronauts by SPE model for CM model 1 and 2 if free space with 2x10^9protons.

Model	Spectrum	Dose (mGy)	Relative Error	Standard Deviation across ICRU Spheres (mGy)
CM 1	ESP-PYSCH Total	13.82	0.4%	1.62
CM 2	ESP-PYSCH Total	4.52	0.5%	1.20
CM 1	ESP-PYSCH Worst	521.36	0.5%	67.80
CM 2	ESP-PYSCH Worst	169.41	0.7%	46.95
CM 1	JPL	884.31	0.3%	71.27
CM 2	JPL	319.42	0.3%	65.28
CM 1	King	8.51	3.7%	5.66
CM 2	King	1.54	2.8%	1.87

Table 7.9: GEANT4-calculated Apollo Mission dose for Apollo 11 and 14 missions with CM model 1.

Apollo Mission	Trapped (mGy)	GCR (mGy)	Total (mGy)	Measured Mission Total (mGy)
11	.093	1.30	1.39	1.8
14	.081	1.46	1.54	11.4

than the measured value. The simulated dose for Apollo 14 was higher than for Apollo 11, with most of the dose due to the increased mission length, thus increasing GCR dose. The standard deviation across the ICRU spheres measuring different locations within the capsule was below one order of magnitude less, thus spatial distribution within the capsule does not explain the significantly higher measured dose of one order of magnitude. If, for example, the King Model for CM 1 is added to the mission totals, the dose is within 5.4% relative error of the measured values; thus there is strong reason to conclude the increased dose was due to increased solar activity during the Apollo 14 mission shown in Table 7.10. The CM model 2 totals were significantly less total dose for both missions, with a very high relative error, thus the added shielding from equipment racks significantly underestimated the dose, requiring more detail in the CM modeling.

Figure 7.14 shows the simulated dose to individual human organs within the anatomical phantom from trapped protons during outbound travel to the moon for Apollo 11 and 14 missions. The dose from the ICRU spheres aligns closely to the trunk dose in the human phantom; however, each organ

Table 7.10: GEANT4-calculated Apollo 14 mission total with a King SPE for CM model 1.

Apollo Mission	Trapped (mGy)	GCR (mGy)	SPE (King) (mGy)	Total (mGy)	Measured (mGy)
14	.081	1.46	8.51	10.8	11.4

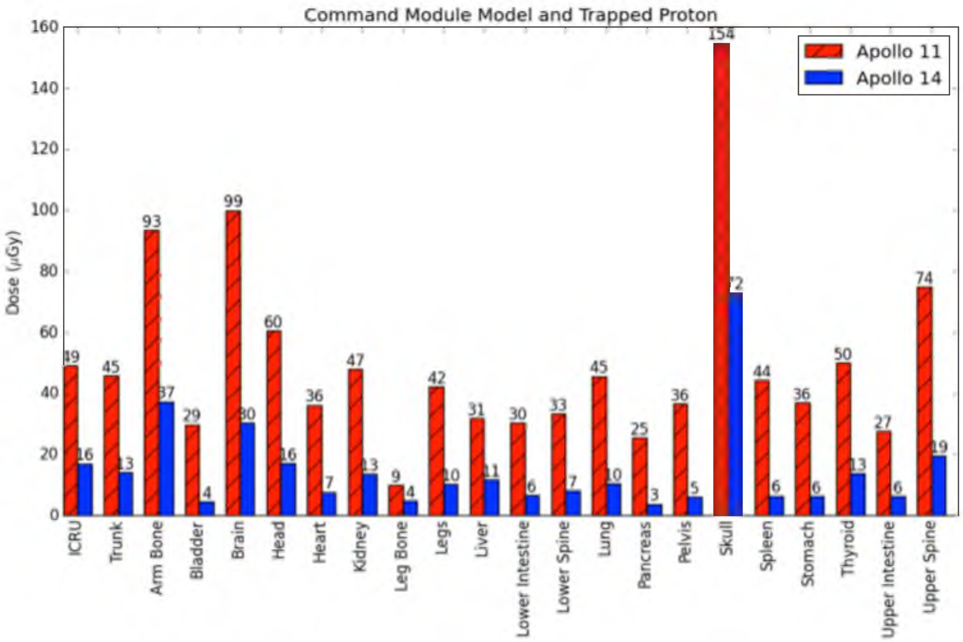

Figure 7.14: GEANT4-calculated trapped proton dose to a human phantom for Apollo 11 and 14 missions showing dose with ICRU spheres and individual organs.

dose varies greatly. The skull received a significantly higher dose than any other organ for both missions. The arm bone, brain, and upper spine also had higher dose rates, which are part of the upper human phantom. The human phantom was placed within the CM with the head towards the forward hatch, so there is less shielding for the upper body than the lower body, resulting in the higher dose distribution for those organs. Thus additional modeling of a human phantom in different orientations would be beneficial.

CHAPTER 8

CONCLUSION AND FUTURE WORK

8.1 Conclusion

The space radiation environment is one of the largest challenges to future deep-space manned missions to the Moon, Mars, and beyond. Future missions will require accurate dose predictions from radiation transport models verified by the long-term measurements of the radiation environment on the International Space Station to insure astronauts radiation doses will be below limits. This thesis developed a faster and more precise GEANT4 model and GEANT4 application that can quickly predict astronaut dose within a spacecraft during future missions from the space radiation environment. These predictions will allow longer missions that are close to the astronaut dose limits allowing for quick prototyping of future radiation-shielding designs.

The developed new simulation application based on GEANT4 successfully implemented MPI and multithreading in a high-performance computing cluster, greatly reducing runtime for large-scale spacecraft simulations. The runtime increases linearly with the number of particles after an initial load cost for the simulation. The speedup was linearly changing with the number of threads, showing strong scaling until all the cores of the node were used, after which hyperthreading gave an increase in performance, but not as strongly. The number of nodes showed strong scaling, with the speedup almost equal to the number of nodes. The application scaled well from one thread to 32 nodes with a total of 216 threads. All nodes and threads completed their own particle loop at roughly the same time, showing good load balancing by event parallelism. The newly developed GEANT4 statistics model is implemented into the application, thus providing calculated statistical relative errors for all simulations without any post processing. This itself is a highly valuable addition to the GEANT4 code system

The ISS simulations provided a valid benchmark of the application's effectiveness and reproducibility to actual experimental data by showing strong correlation with experimental data and previous simulations by others with the variation in dose less then the margin of error from the input spectra. The simulations showed similar results to the DESIRE study, with significantly shorter runtime and minimal post processing. The QBBC, QGSP_BIC_HP, and QGSP_BERT_HP physics lists all show close agreement, thus the faster QBBC physics list accurately models the needed physics transportation without the need for high-precision neutron libraries. The equivalent dose scorer resulted in a quality factor close to the experimental for GCR; however, the quality factor was significantly higher for the trapped proton spectrum, requiring further analysis and improvement of the scorer calculating the quality factor for each particle. The simulations also showed that the truncated geometry showed good agreement to the full geometry as long as the modules matched the correct mass and shielding density, similar to the DESIRE project results. The trapped proton dose estimates during Solar Maximum and Minimum match well to the experimental data; however, for GCR the simulated dose was half the experimental value, thus requiring improvements to the input models for GCR during the time period.

The implemented CPD and TEPC space radiation detector models were less efficient in scoring particles then the ICRU spheres and anatomical human phantom model due to the smaller size. The CPD was more efficient then the TEPC model at scoring particles due to the TLDs in the CPD being denser then the TEPC. The TEPC model showed the most uniform energy deposition across different proton energies; however, due to the low efficiency, the best detector models within simulations are the ICRU spheres and anatomical human phantom models. In the GEANT4 Apollo CM Module simulation comparing ICRU sphere dose with the anatomical model, the ICRU sphere and trunk from the anatomical model had similar dose values, thus showing the ICRU sphere closely approximates a whole-body dose. In the anatomical model, the dose was greater to organs with less shielding, showing a spatial dependence on the anatomical model orientation.

The Apollo simulations correctly recreated the trajectory for the Apollo 11 and 14 missions and Saturn V Command Module. The simulation of Apollo 11 closely matched the experimental data within input spectra error; however, the Apollo 14 simulation did not match the order of magnitude larger measured dose. Two models of the Command Module were built: CM model 1 with a simplified geometry of only outer shielding layers and CM model 2 with additional internal equipment racks to correctly match the Command Module mass. The CM model 1 simulations more closely matched the experimental data; however, CM model 2 did not. Although the CM model 2 correctly simulated the mass, the model’s extra shielding from the equipment racks underestimated dose, requiring more detailed modeling of interior spaces. The trapped proton and electron dose for Apollo 14 was less then for Apollo 11; however, the total dose was higher due to increased mission length and GCR exposure. The lateral and vertical variation in dose distribution was too small to explain the order of magnitude higher dose for Apollo 14, nor did the trajectory increase the dose. Simulations of SPE models showed that a SPE event would not be fatal and varied with magnitude. When combining a King SPE event with the Apollo 14 simulation, the calculated dose matched closely to experimental values, giving strong reason to conclude the increased dose was due to the previous week's solar flares.

8.2 Future Work

Future work to the new GEANT4-based application requires improving the scoring mesh and run merge to avoid occasional segmentation fault when overloading the buffer by adding a blocking function by node until each node has completed transmitting its data. Also the merge functions could use alternative methods for combining node data, such as prefix sum to reduce simulation merge time. Additional improvements to the MPI GEANT4 libraries include improving the random seed generator to store all seeds across nodes for rerunning. Other future improvements to the GEANT4 code include adding DAGMC interface for importing CAD drawings from high-precision models. The DAGMC toolkit creates a geometry file based on the tessellated geometry and allows for easy exchange between codes. The equivalent dose scorers need further analysis to improve the estimation of quality factor.

For ISS mission durations of six months, the error margin in dose estimation is not significant; however, for longer missions to Mars, the great variation in the dose distribution could cause different simulations to overestimate or underestimate the dose compared with the allowed dose limits for astronauts, providing poor predictions for mission preparation. Thus the next step in simulations is to use more precise CAD drawings of the full geometry, matching input spectra to the new AMAS detector-measured spectra. The AMAS detector is mounted externally to the ISS and will give a more precise input distribution for the models. Thus using the input data with DAGMC to provide better high-fidelity detailed geometry models, the simulations can be verified with more detailed experimental data from within different regions within the ISS and compared to other radiation transport codes, including FLUKA and HZETRN, for validation. Future dose predictions will also require improved input models for spectra especially for GCR.

After validation with more detailed ISS models, the application can then be applied to future cislunar missions similar to the Apollo missions and missions to Mars. For these future missions, the code will be combined with a statistical analysis package, which can perturb input geometry to allow for passive shielding optimization by varying shielding material and thicknesses, while striving to minimize shielding weight and providing thermal insulation and micrometeoroid protection. In future, the application will also transport radiation through magnetic fields allowing for the addition of magnetic fields, to the spacecraft models to study active shielding designs. Active shielding uses magnetic fields to deflect particles' trajectory from entering a spacecraft. These improved passive shielding designs, combined with active shielding using magnetic fields, could provide a breakthrough allowing for long duration missions and better protection for astronauts from SPEs and the space radiation environment.

APPENDIX A

GEOMETRY MODELS

A.1 Crew Personal Dosimeter GDML Model

```
<?xml version=”1.0” encoding=”UTF-8” ?>
<gdml xmlns:xsi=”http://www.w3.org/2001/XMLSchema-instance”
    xsi:noNamespaceSchemaLocation=”http://service-spi.web.cern.ch/service-spi/
    app/releases/GDML/schema/gdml.xsd”>

<define>
  <position name=”CPDPosition” unit=”m” x=”0” y=”0” z=”0” />
  <matrix name=”m” coldim=”2” values=”-2␣-0.75␣-2␣-0.25␣-2␣0.25␣-2␣0.75␣-1.5␣
      -0.75␣-1.5␣-0.25␣-1.5␣0.25␣␣-1.5␣0.75␣␣-1␣-0.75␣␣-1␣-0.25␣␣-1␣0.25␣␣-1␣
      0.75␣␣-0.5␣-0.75␣␣-0.5␣-0.25␣-0.5␣0.25␣␣-0.5␣0.75␣␣0.5␣-0.75␣␣0.5␣-0.25␣␣
      0.5␣0.25␣␣0.5␣0.75␣␣1␣-0.75␣␣1␣-0.25␣␣1␣0.25␣␣1␣0.75␣␣1.5␣-0.75␣␣1.5␣-0.25
      ␣␣1.5␣0.25␣␣1.5␣0.75␣␣2␣-0.75␣␣2␣-0.25␣␣2␣0.25␣␣2␣0.75” />
  <constant name=”numberofTLD” value=”32” />
  <variable name=”numberRows” value=”1” />
  <variable name=”numberTLD” value=”1” />
  <variable name=”number_TLD” value=”1” />
 </define>

<materials>
  <element Z=”1” formula=”H” name=”Hydrogen” >
        <atom value=”1.00794” />
    </element>
  <element Z=”6” formula=”C” name=”Carbon” >
      <atom value=”12.0107” />
  </element>
  <element Z=”8” formula=”O” name=”Oxygen” >
      <atom value=”15.9994” />
  </element>
  <element Z=”7” formula=”N” name=”Nitrogen” >
      <atom value=”14.0067” />
  </element>
  <element Z=”9” formula=”F” name=”Fluorine” >
      <atom value=”18.998404” />
  </element>
  <isotope Z=”3” N=”6” name=”Lithium6” >
      <atom value=”6.015122” />
  </isotope>
  <isotope Z=”3” N=”7” name=”Lithium7” >
      <atom value=”7.016004” />
  </isotope>
  <element name=”lithium_mixture” >
      <fraction ref=”Lithium6” n=”0.9214” />
      <fraction ref=”Lithium7” n=”0.0786” />
```

```
  </element>

  <material formula=”” name=”Lexan” >
      <D value=”1.2” />
      <composite n=”6” ref=”Hydrogen” />
      <composite n=”3” ref=”Carbon” />
      <composite n=”3” ref=”Oxygen” />
    </material>

  <material formula=”” name=”TLD100” >
      <D value=”2.64” />
      <composite n=”1” ref=”lithium_mixture” />
      <composite n=”1” ref=”Fluorine” />
  </material>

  <material Z=”1” formula=”” name=”Vacuum” >
      <D value=”1e-25” />
      <atom value=”1.01” />
    </material>
</materials>

<solids>
  <box name=”WorldBox” lunit=”m” x=”1” y=”1” z=”1”/>

  <box name=”holder” lunit=”cm” x=”5.0” y=”3.0” z=”.50”/>
  <tube name=”TLD” lunit=”cm” aunit=”degree” rmax=”.25” z=”.1” deltaphi=”360”
      startphi=”0”/>
</solids>

<structure>
<loop for=”numberTLD” to=”numberofTLD” step=”1”>
<volume name=”TLD”>
    <materialref ref=”TLD100”/>
    <solidref ref=”TLD” />
    <auxiliary auxtype=”SensDet” auxvalue=”ICRU1”/>
</volume>
</loop>

<volume name=”LexanHolder”>
    <materialref ref=”Lexan”/>
    <solidref ref=”holder” />
    <loop for=”numberRows” to=”numberofTLD” step=”1”>
    <physvol>
        <volumeref ref=”TLD”/>
        <position unit=”cm” x=”m[numberRows,1]” y=”m[numberRows,2]” z=”0”/>
    </physvol>
    </loop>
</volume>

<volume name=”World”>
    <materialref ref=”Vacuum”/>
    <solidref ref=”WorldBox”/>
    <physvol>
        <volumeref ref=”LexanHolder”/>
        <positionref ref=”CPDPosition”/>
    </physvol>
</volume>
</structure>
```

```
<setup version=”1.0” name=”Default”>
    <world ref=”World”/>
</setup>

</gdml>
```

A.2 Tissue Equivalent Proportional Counter GDML Model

```
<?xml version=”1.0” encoding=”UTF-8” ?>
<gdml xmlns:xsi=”http://www.w3.org/2001/XMLSchema-instance”
    xsi:noNamespaceSchemaLocation=”http://service-spi.web.cern.ch/service-spi/
    app/releases/GDML/schema/gdml.xsd”>

<define>
  <position name=”TEPCPosition” unit=”m” x=”0” y=”0” z=”0” />
 </define>

<materials>
  <element Z=”1” formula=”H” name=”Hydrogen” >
        <atom value=”1.00794” />
    </element>
  <element Z=”6” formula=”C” name=”Carbon” >
      <atom value=”12.0107” />
  </element>
  <element Z=”8” formula=”O” name=”Oxygen” >
      <atom value=”15.9994” />
  </element>
  <element Z=”7” formula=”N” name=”Nitrogen” >
      <atom value=”14.0067” />
  </element>
  <element Z=”20” formula=”Ca” name=”Calcium” >
      <atom value=”40.078” />
  </element>
  <element Z=”9” formula=”F” name=”Fluorine” >
      <atom value=”18.998404” />
  </element>
  <element Z=”28” formula=”Ni” name=”Nickel” >
      <atom value=”58.6934” />
  </element>
  <element Z=”24” formula=”Cr” name=”Chromium” >
      <atom value=”51.9961” />
  </element>
  <element Z=”26” formula=”Fe” name=”Iron” >
      <atom value=”55.845” />
  </element>
  <element Z=”14” formula=”Si” name=”Silicon” >
      <atom value=”28.0855” />
  </element>
  <element Z=”25” formula=”Mn” name=”Manganese” >
      <atom value=”54.93805” />
  </element>
  <element Z=”15” formula=”P” name=”Phosphorus” >
      <atom value=”30.97376” />
  </element>
  <element Z=”16” formula=”S” name=”Sulfur” >
      <atom value=”32.066” />
  </element>

<material name=”Aluminum” Z=”13.0” >
```

```
    <D value=”2.70” />
    <atom value=”26.98” />
</material>

  <material formula=”” name=”A150_Plastic” >
      <D value=”1.127” />
      <fraction n=”.102” ref=”Hydrogen” />
      <fraction n=”.768” ref=”Carbon” />
      <fraction n=”.059” ref=”Oxygen” />
      <fraction n=”0.036” ref=”Nitrogen” />
      <fraction n=”0.018” ref=”Calcium” />
      <fraction n=”0.017” ref=”Fluorine” />
    </material>

  <material formula=”” name=”StainlessSteel303” >
      <D value=”8.03” />
      <fraction n=”.09” ref=”Nickel” />
      <fraction n=”.18” ref=”Chromium” />
      <fraction n=”.6981” ref=”Iron” />
      <fraction n=”0.01” ref=”Silicon” />
      <fraction n=”0.02” ref=”Manganese” />
      <fraction n=”0.0012” ref=”Carbon” />
      <fraction n=”0.0004” ref=”Phosphorus” />
      <fraction n=”0.0003” ref=”Sulfur” />
  </material>

<material formula=”C3H8” name=”Propane” >
    <D value=”3.62e-5” />
    <composite n=”8” ref=”Hydrogen” />
    <composite n=”3” ref=”Carbon” />
</material>

  <material Z=”1” formula=”” name=”Vacuum” >
      <D value=”1e-25” />
      <atom value=”1.01” />
    </material>
 </materials>

 <solids>
  <box name=”WorldBox” unit=”m” x=”1” y=”1” z=”1”/>

<tube name=”Casing” lunit=”cm” aunit=”degree” rmax=”5.12/2” z=”5.12” deltaphi=”
    360” startphi=”0”  />
<tube name=”Vacuum_tube” lunit=”cm” aunit=”degree” rmax=”5.12/2” rmin=”5.1/2” z=
    ”5.12” deltaphi=”360” startphi=”0”  />
<tube name=”Plastic” lunit=”cm” aunit=”degree” rmax=”5.08/2” rmin=”5.06/2” z=”
    5.08” deltaphi=”360” startphi=”0”  />
<tube name=”Propane_Interior” lunit=”cm” aunit=”degree” rmax=”5.1/2” z=”5.1”
    deltaphi=”360” startphi=”0”  />
 </solids>

<structure>
<volume name=”Inside_Detector”>
    <materialref ref=”Propane”/>
    <solidref ref=”Propane_Interior” />
</volume>
<volume name=”Tissue_Plastic”>
    <materialref ref=”A150_Plastic”/>
    <solidref ref=”Plastic” />
```

```
    <physvol>
        <volumeref ref=”Inside_Detector”/>
    </physvol>
</volume>
<volume name=”Vacuum_Chamber”>
    <materialref ref=”StainlessSteel303”/>
    <solidref ref=”Vacuum_tube” />
    <physvol>
        <volumeref ref=”Tissue_Plastic”/>
    </physvol>
</volume>
<volume name=”TEPC”>
    <materialref ref=”Propane”/>
    <solidref ref=”Casing”/>
    <physvol>
        <volumeref ref=”Vacuum_Chamber”/>
    </physvol>
    <auxiliary auxtype=”SensDet” auxvalue=”ICRU1”/>
</volume>
<volume name=”World”>
   <materialref ref=”Vacuum”/>
   <solidref ref=”WorldBox”/>
   <physvol>
     <volumeref ref=”TEPC”/>
     <positionref ref=”TEPCPosition”/>
   </physvol>
  </volume>
</structure>

<setup version=”1.0” name=”Default”>
    <world ref=”World”/>
</setup>

</gdml>
```

A.3 Apollo Command Module GDML Model 1

```
<?xml version=”1.0” encoding=”UTF-8” ?>
<gdml xmlns:xsi=”http://www.w3.org/2001/XMLSchema-instance”
    xsi:noNamespaceSchemaLocation=”gdml.xsd”>
    <define>
        <position name=”CM_Central_Position” unit=”cm” x=”0” y=”0” z=”-120.65”/>
        <position name=”CM_Bottom_Position” unit=”cm” x=”0” y=”0” z=”229.65”/>
        <position name=”subtraction” unit=”cm” x=”0” y=”0” z=”34.7”/>
        <position name=”CM_Hatch_Position” unit=”cm” x=”0” y=”0” z=”123.03”/>
        <position name=”CM_Forward_Position” unit=”cm” x=”0” y=”0” z=”57.3”/>
        <position name=”Kapton_Hatch_Position” unit=”cm” x=”0” y=”0” z=”-2.32415
            ”/>
        <position name=”Insulation_Hatch_Position” unit=”cm” x=”0” y=”0” z=”
            -.58505”/>
        <position name=”Aluminum_Outer_Hatch_Position” unit=”cm” x=”0” y=”0” z=”
            1.15405”/>
        <position name=”Aluminum_Honeycomb_Hatch_Position” unit=”cm” x=”0” y=”0”
             z=”1.73905”/>
        <position name=”Aluminum_Inner_Hatch_Position” unit=”cm” x=”0” y=”0” z=”
            2.32405”/>
        <!--ICRU Spheres Positions-->
        <position name=”ICRUPosition1” unit=”cm” x=”0” y=”0” z=”20” />
        <position name=”ICRUPosition2” unit=”cm” x=”50” y=”0” z=”20” />
```

```
    <position name=”ICRUPosition3” unit=”cm” x=”-50” y=”0” z=”20” />
    <position name=”ICRUPosition4” unit=”cm” x=”0” y=”50” z=”20” />
    <position name=”ICRUPosition5” unit=”cm” x=”0” y=”-50” z=”20” />
    <position name=”ICRUPosition6” unit=”cm” x=”0” y=”0” z=”70” />
    <position name=”ICRUPosition7” unit=”cm” x=”50” y=”0” z=”70” />
    <position name=”ICRUPosition8” unit=”cm” x=”-50” y=”0” z=”70” />
    <position name=”ICRUPosition9” unit=”cm” x=”0” y=”50” z=”70” />
    <position name=”ICRUPosition10” unit=”cm” x=”0” y=”-50” z=”70” />
    <position name=”ICRUPosition11” unit=”cm” x=”0” y=”0” z=”120” />
    <position name=”ICRUPosition12” unit=”cm” x=”50” y=”0” z=”120” />
    <position name=”ICRUPosition13” unit=”cm” x=”-50” y=”0” z=”120” />
    <position name=”ICRUPosition14” unit=”cm” x=”0” y=”50” z=”120” />
    <position name=”ICRUPosition15” unit=”cm” x=”0” y=”-50” z=”120” />
</define>
<materials>
    <element Z=”1” formula=”H” name=”Hydrogen”>
        <atom value=”1.00794”/>
    </element>
    <element Z=”6” formula=”C” name=”Carbon”>
        <atom value=”12.0107”/>
    </element>
    <element Z=”8” formula=”O” name=”Oxygen”>
        <atom value=”15.9994”/>
    </element>
    <element Z=”7” formula=”N” name=”Nitrogen”>
        <atom value=”14.0067”/>
    </element>
    <element Z=”9” formula=”F” name=”Fluorine”>
        <atom value=”18.998404”/>
    </element>
    <element Z=”13” formula=”Al” name=”Aluminium”>
        <atom value=”26.9815385”/>
    </element>
    <element Z=”14” formula=”Si” name=”Silicon”>
        <atom value=”28.0855”/>
    </element>
    <element Z=”15” formula=”P” name=”Phosphorus”>
        <atom value=”30.97376”/>
    </element>
    <element Z=”16” formula=”S” name=”Sulfur”>
        <atom value=”32.066”/>
    </element>
    <element Z=”20” formula=”Ca” name=”Calcium”>
        <atom value=”40.078”/>
    </element>
    <element Z=”24” formula=”Cr” name=”Chromium”>
        <atom value=”51.9961”/>
    </element>
    <element Z=”25” formula=”Mn” name=”Manganese”>
        <atom value=”54.93805”/>
    </element>
    <element Z=”26” formula=”Fe” name=”Iron”>
        <atom value=”55.845”/>
    </element>
    <element Z=”28” formula=”Ni” name=”Nickel”>
        <atom value=”58.6934”/>
    </element>
    <element Z=”42” formula=”Mo” name=”Molybdenum”>
        <atom value=”95.95”/>
```

```
</element>
<material formula=”C10H8O4␣” name=”Mylar”>
    <D value=”1.38”/>
    <composite n=”8” ref=”Hydrogen”/>
    <composite n=”10” ref=”Carbon”/>
    <composite n=”4” ref=”Oxygen”/>
</material>
<material formula=”␣” name=”Ablator”>
    <D value=”.51”/>
    <fraction ref=”Oxygen” n=”.4087”/>
    <fraction ref=”Silicon” n=”.1169”/>
    <fraction ref=”Carbon” n=”.4137”/>
    <fraction ref=”Hydrogen” n=”.0608”/>
</material>
<material formula=”␣” name=”StainlessSteelPH14_8Mo”>
    <D value=”7.82”/>
    <fraction ref=”Carbon” n=”0.0005”/>
    <fraction ref=”Silicon” n=”0.01”/>
    <fraction ref=”Manganese” n=”0.01”/>
    <fraction ref=”Phosphorus” n=”0.00015”/>
    <fraction ref=”Sulfur” n=”0.0001”/>
    <fraction ref=”Chromium” n=”0.15”/>
    <fraction ref=”Nickel” n=”0.0875”/>
    <fraction ref=”Molybdenum” n=”0.03”/>
    <fraction ref=”Aluminium” n=”0.015”/>
    <fraction ref=”Iron” n=”0.69675”/>
</material>
<material formula=”␣” name=”StainlessSteelPH14_8Mo_Honeycomb”>
    <D value=”.14”/>
    <fraction ref=”Carbon” n=”0.0005”/>
    <fraction ref=”Silicon” n=”0.01”/>
    <fraction ref=”Manganese” n=”0.01”/>
    <fraction ref=”Phosphorus” n=”0.00015”/>
    <fraction ref=”Sulfur” n=”0.0001”/>
    <fraction ref=”Chromium” n=”0.15”/>
    <fraction ref=”Nickel” n=”0.0875”/>
    <fraction ref=”Molybdenum” n=”0.03”/>
    <fraction ref=”Aluminium” n=”0.015”/>
    <fraction ref=”Iron” n=”0.69675”/>
</material>
<material Z=”13” formula=”␣” name=”Aluminum”>
    <D value=”2.70”/>
    <atom value=”26.98”/>
</material>
<material formula=”␣” name=”Insulation”>
    <D value=”.056”/>
    <fraction ref=”Oxygen” n=”.5009”/>
    <fraction ref=”Silicon” n=”.4586”/>
    <fraction ref=”Carbon” n=”.0324”/>
    <fraction ref=”Hydrogen” n=”.0082”/>
</material>
<material Z=”13” formula=”␣” name=”Aluminum_Honeycomb”>
    <D value=”.0497”/>
    <atom value=”26.98”/>
</material>
<material Z=”1” formula=”␣” name=”Vacuum”>
    <D value=”1e-25”/>
    <atom value=”1.01”/>
</material>
```

```
        <material formula=”␣” name=”Air”>
            <D value=”0.00125”/>
            <fraction n=”0.79” ref=”Nitrogen”/>
            <fraction n=”0.21” ref=”Oxygen”/>
        </material>
        <material formula=”␣” name=”ICRU_Tissue” >
            <D value=”1” />
            <fraction n=”0.762” ref=”Oxygen” />
            <fraction n=”0.111” ref=”Carbon” />
            <fraction n=”0.101” ref=”Hydrogen” />
            <fraction n=”0.026” ref=”Nitrogen” />
        </material>
    </materials>
    <solids>
        <!-- -->
        <box name=”UniverseBox” lunit=”m” x=”10” y=”10” z=”10”/>
        <!--Central Heat Shield and Structure -->
        <polycone name=”Central_Heat_Shield” startphi=”␣0” deltaphi=”360” aunit=
            ”degree” lunit=”cm”>
            <zplane z=”0” rmax=”195.58” rmin=”0”/>
            <zplane z=”177.8” rmax=”99.07” rmin=”0”/>
            <zplane z=”178” rmax=”57.15” rmin=”0”/>
            <zplane z=”241.3” rmax=”45.73” rmin=”0”/> </polycone>
        <polycone name=”Kapton” startphi=”␣0” deltaphi=”360” aunit=”degree”
            lunit=”cm”>
            <zplane z=”0” rmax=”195.58” rmin=”195.48”/>
            <zplane z=”177.8” rmax=”99.06” rmin=”98.96”/>
            <zplane z=”178” rmax=”57.15” rmin=”57.05”/>
            <zplane z=”241.3” rmax=”45.72” rmin=”45.62”/> </polycone>
        <polycone name=”Ablator_SD” startphi=”␣0” deltaphi=”360” aunit=”degree”
            lunit=”cm”>
            <zplane z=”0” rmax=”195.48” rmin=”193.194”/>
            <zplane z=”177.8” rmax=”98.96” rmin=”96.674”/>
            <zplane z=”178” rmax=”57.05” rmin=”54.764”/>
            <zplane z=”241.3” rmax=”45.62” rmin=”43.334”/> </polycone>
        <polycone name=”Stainless_Steel_Outer_Plate” startphi=”␣0” deltaphi=”360
            ” aunit=”degree” lunit=”cm”>
            <zplane z=”0” rmax=”193.194” rmin=”193.004”/>
            <zplane z=”177.8” rmax=”96.674” rmin=”96.484”/>
            <zplane z=”178” rmax=”54.764” rmin=”54.574”/>
            <zplane z=”241.3” rmax=”43.334” rmin=”43.144”/> </polycone>
        <polycone name=”Saintless_Steel_Honeycomb” startphi=”␣0” deltaphi=”360”
            aunit=”degree” lunit=”cm”>
            <zplane z=”0” rmax=”193.004” rmin=”192.114”/>
            <zplane z=”177.8” rmax=”96.484” rmin=”95.594”/>
            <zplane z=”178” rmax=”54.574” rmin=”53.684”/>
            <zplane z=”241.3” rmax=”43.144” rmin=”42.254”/> </polycone>
        <polycone name=”Stainless_Steel_Inner_Plate” startphi=”␣0” deltaphi=”360
            ” aunit=”degree” lunit=”cm”>
            <zplane z=”0” rmax=”192.114” rmin=”191.924”/>
            <zplane z=”177.8” rmax=”95.594” rmin=”95.404”/>
            <zplane z=”178” rmax=”53.684” rmin=”53.494”/>
            <zplane z=”241.3” rmax=”42.254” rmin=”42.064”/> </polycone>
        <polycone name=”Insulation_SD” startphi=”␣0” deltaphi=”360” aunit=”
            degree” lunit=”cm”>
            <zplane z=”0” rmax=”191.924” rmin=”188.5458”/>
            <zplane z=”177.8” rmax=”95.404” rmin=”92.0258”/>
            <zplane z=”178” rmax=”53.494” rmin=”50.1158”/>
            <zplane z=”241.3” rmax=”42.064” rmin=”38.6858”/> </polycone>
```

```
<polycone name="Aluminum_Outer_Plate" startphi="␣0" deltaphi="360" aunit
    ="degree" lunit="cm">
    <zplane z="0" rmax="188.5458" rmin="188.4458"/>
    <zplane z="177.8" rmax="92.0258" rmin="91.9258"/>
    <zplane z="178" rmax="50.1158" rmin="50.0158"/>
    <zplane z="241.3" rmax="38.6858" rmin="38.5858"/> </polycone>
<polycone name="Aluminum_Honeycomb_SD" startphi="␣0" deltaphi="360"
    aunit="degree" lunit="cm">
    <zplane z="0" rmax="188.4458" rmin="185.0458"/>
    <zplane z="177.8" rmax="91.9258" rmin="90.8558"/>
    <zplane z="178" rmax="50.0158" rmin="48.9458"/>
    <zplane z="241.3" rmax="38.5858" rmin="37.5158"/> </polycone>
<polycone name="Aluminum_Inner_Plate" startphi="␣0" deltaphi="360" aunit
    ="degree" lunit="cm">
    <zplane z="0" rmax="185.0458" rmin="184.9458"/>
    <zplane z="177.8" rmax="90.8558" rmin="90.7558"/>
    <zplane z="178" rmax="48.9458" rmin="48.8458"/>
    <zplane z="241.3" rmax="37.5158" rmin="37.4158"/> </polycone>
<polycone name="Interior" startphi="␣0" deltaphi="360" aunit="degree"
    lunit="cm">
    <zplane z="0" rmax="184.9458" rmin="0"/>
    <zplane z="177.8" rmax="90.7558" rmin="0"/>
    <zplane z="178" rmax="48.8458" rmin="0"/>
    <zplane z="241.3" rmax="37.4158" rmin="0"/> </polycone>
<!--Aft Heat Shield -->
<tube name="sub_tube" startphi="0" deltaphi="360" aunit="degree" lunit="
    cm" rmax="410" z="770"/>
<sphere name="Aft_Heat_Shield_S" startphi="0" deltaphi="360" aunit="
    degree" lunit="cm" starttheta="0" deltatheta="180" rmax="401.90"
    rmin="0"/>
<subtraction name="Aft_Heat_Shield">
    <first ref="Aft_Heat_Shield_S"/> <second ref="sub_tube"/>
    <positionref ref="subtraction" />
</subtraction>
<sphere name="Kapton_Aft_S" startphi="0" deltaphi="360" aunit="degree"
    lunit="cm" starttheta="0" deltatheta="180" rmax="401.8915" rmin="0"/
    >
<subtraction name="Kapton_Aft">
    <first ref="Kapton_Aft_S"/> <second ref="sub_tube"/>
    <positionref ref="subtraction" />
</subtraction>
<sphere name="Ablator_Aft_S" startphi="0" deltaphi="360" aunit="degree"
    lunit="cm" starttheta="0" deltatheta="180" rmax="401.7915" rmin="0"/
    >
<subtraction name="Ablator_Aft">
    <first ref="Ablator_Aft_S"/> <second ref="sub_tube"/>
    <positionref ref="subtraction" />
</subtraction>
<sphere name="Stainless_Steel_Outer_Plate_Aft_S" startphi="0" deltaphi="
    360" aunit="degree" lunit="cm" starttheta="0" deltatheta="180" rmax=
    "394.9335" rmin="0"/>
<subtraction name="Stainless_Steel_Outer_Plate_Aft">
    <first ref="Stainless_Steel_Outer_Plate_Aft_S"/> <second ref="
        sub_tube"/>
    <positionref ref="subtraction" />
</subtraction>
<sphere name="Saintless_Steel_Honeycomb_Aft_S" startphi="0" deltaphi="
    360" aunit="degree" lunit="cm" starttheta="0" deltatheta="180" rmax=
    "394.7435" rmin="0"/>
```

```
<subtraction name=”Saintless_Steel_Honeycomb_Aft”>
    <first ref=”Saintless_Steel_Honeycomb_Aft_S”/> <second ref=”sub_tube
        ”/>
    <positionref ref=”subtraction” />
</subtraction>
<sphere name=”Stainless_Steel_Inner_Plate_Aft_S” startphi=”0” deltaphi=”
    360” aunit=”degree” lunit=”cm” starttheta=”0” deltatheta=”180” rmax=
    ”390.0435” rmin=”0”/>
<subtraction name=”Stainless_Steel_Inner_Plate_Aft”>
    <first ref=”Stainless_Steel_Inner_Plate_Aft_S”/> <second ref=”
        sub_tube”/>
    <positionref ref=”subtraction” />
</subtraction>
<sphere name=”Insulation_Aft_S” startphi=”0” deltaphi=”360” aunit=”
    degree” lunit=”cm” starttheta=”0” deltatheta=”180” rmax=”389.8535”
    rmin=”0”/>
<subtraction name=”Insulation_Aft”>
    <first ref=”Insulation_Aft_S”/> <second ref=”sub_tube”/>
    <positionref ref=”subtraction” />
</subtraction>
<sphere name=”Aluminum_Outer_Plate_Aft_S” startphi=”0” deltaphi=”360”
    aunit=”degree” lunit=”cm” starttheta=”0” deltatheta=”180” rmax=”
    387.8215” rmin=”0”/>
<subtraction name=”Aluminum_Outer_Plate_Aft”>
    <first ref=”Aluminum_Outer_Plate_Aft_S”/> <second ref=”sub_tube”/>
    <positionref ref=”subtraction” />
</subtraction>
<sphere name=”Aluminum_Honeycomb_Aft_S” startphi=”0” deltaphi=”360”
    aunit=”degree” lunit=”cm” starttheta=”0” deltatheta=”180” rmax=”
    387.7215” rmin=”0”/>
<subtraction name=”Aluminum_Honeycomb_Aft”>
    <first ref=”Aluminum_Honeycomb_Aft_S”/> <second ref=”sub_tube”/>
    <positionref ref=”subtraction” />
</subtraction>
<sphere name=”Aluminum_Inner_Plate_Aft_S” startphi=”0” deltaphi=”360”
    aunit=”degree” lunit=”cm” starttheta=”0” deltatheta=”180” rmax=”
    384.3215” rmin=”0”/>
<subtraction name=”Aluminum_Inner_Plate_Aft”>
    <first ref=”Aluminum_Inner_Plate_Aft_S”/> <second ref=”sub_tube”/>
    <positionref ref=”subtraction” />
</subtraction>
<sphere name=”Interior_Aft_S” startphi=”0” deltaphi=”360” aunit=”degree”
     lunit=”cm” starttheta=”0” deltatheta=”180” rmax=”384.2215” rmin=”0”
    />
<subtraction name=”Interior_Aft”>
    <first ref=”Interior_Aft_S”/> <second ref=”sub_tube”/>
    <positionref ref=”subtraction” />
</subtraction>
<!--Interior -->
<polycone name=”Interior_Central” startphi=”␣0” deltaphi=”360” aunit=”
    degree” lunit=”cm”>
    <zplane z=”0” rmax=”184.9458” rmin=”0”/>
    <zplane z=”177.8” rmax=”90.7558” rmin=”0”/>
    <zplane z=”178” rmax=”48.8458” rmin=”0”/>
    <zplane z=”241.3” rmax=”37.4158” rmin=”0”/> </polycone>
<!--Forward Hatch -->
<tube name=”Forward_Hatch”  startphi=”0” deltaphi=”360” aunit=”degree”
    lunit=”cm” z=”4.7483” rmax=”45.7”/>
<tube name=”Kapton_Hatch”  startphi=”0” deltaphi=”360” aunit=”degree”
```

```
        lunit="cm" z="0.1" rmax="45.7"/>
    <tube name="Insulation_Hatch"  startphi="0" deltaphi="360" aunit="degree
        " lunit="cm" z="3.3782" rmax="45.7"/>
    <tube name="Aluminum_Outer_Plate_Hatch"  startphi="0" deltaphi="360"
        aunit="degree" lunit="cm" z="0.1" rmax="45.7"/>
    <tube name="Aluminum_Honeycomb_Hatch"  startphi="0" deltaphi="360" aunit
        ="degree" lunit="cm" z="1.07" rmax="45.7"/>
    <tube name="Aluminum_Inner_Plate_Hatch"  startphi="0" deltaphi="360"
        aunit="degree" lunit="cm" z="0.1" rmax="45.7"/>
    <!--Forward Heat Shield -->
    <polycone name="Forward_Heat_Shield" startphi="␣0" deltaphi="360" aunit=
        "degree" lunit="cm">
        <zplane z="0" rmax="99" rmin="95"/>
        <zplane z="73.3" rmax="49.656" rmin="46"/> </polycone>
    <polycone name="Kapton_Forward" startphi="␣0" deltaphi="360" aunit="
        degree" lunit="cm">
        <zplane z="0" rmax="99" rmin="98.9"/>
        <zplane z="73.3" rmax="49.656" rmin="49.556"/> </polycone>
    <polycone name="Ablator_Forward" startphi="␣0" deltaphi="360" aunit="
        degree" lunit="cm">
        <zplane z="0" rmax="98.9" rmin="96.614"/>
        <zplane z="73.3" rmax="49.556" rmin="47.27"/> </polycone>
    <polycone name="Stainless_Steel_Outer_Plate_Forward" startphi="␣0"
        deltaphi="360" aunit="degree" lunit="cm">
        <zplane z="0" rmax="96.614" rmin="96.424"/>
        <zplane z="73.3" rmax="47.27" rmin="47.08"/> </polycone>
    <polycone name="Saintless_Steel_Honeycomb_Forward" startphi="␣0"
        deltaphi="360" aunit="degree" lunit="cm">
        <zplane z="0" rmax="96.424" rmin="95.534"/>
        <zplane z="73.3" rmax="47.08" rmin="46.19"/> </polycone>
    <polycone name="Stainless_Steel_Inner_Plate_Forward" startphi="␣0"
        deltaphi="360" aunit="degree" lunit="cm">
        <zplane z="0" rmax="95.534" rmin="95.344"/>
        <zplane z="73.3" rmax="46.19" rmin="46"/> </polycone>
    <sphere name="ICRUSphere15cm" rmax="150" rmin="0" aunit="degree"
        deltaphi="360" deltatheta="180" lunit="mm"  startphi="0" starttheta=
        "0" />
</solids>
<structure>
    <!--ICRU Spheres-->
    <volume name="ICRUSpherePhantom1">
        <materialref ref="ICRU_Tissue"/>
        <solidref ref="ICRUSphere15cm" />
        <auxiliary auxtype="SensDet" auxvalue="ICRU1"/>
    </volume>
    <volume name="ICRUSpherePhantom2">
        <materialref ref="ICRU_Tissue"/>
        <solidref ref="ICRUSphere15cm" />
        <auxiliary auxtype="SensDet" auxvalue="ICRU2"/>
    </volume>
    <volume name="ICRUSpherePhantom3">
        <materialref ref="ICRU_Tissue"/>
        <solidref ref="ICRUSphere15cm" />
        <auxiliary auxtype="SensDet" auxvalue="ICRU3"/>
    </volume>
    <volume name="ICRUSpherePhantom4">
        <materialref ref="ICRU_Tissue"/>
        <solidref ref="ICRUSphere15cm" />
        <auxiliary auxtype="SensDet" auxvalue="ICRU4"/>
```

```
</volume>
<volume name=”ICRUSpherePhantom5”>
    <materialref ref=”ICRU_Tissue”/>
    <solidref ref=”ICRUSphere15cm” />
    <auxiliary auxtype=”SensDet” auxvalue=”ICRU5”/>
</volume>
<volume name=”ICRUSpherePhantom6”>
    <materialref ref=”ICRU_Tissue”/>
    <solidref ref=”ICRUSphere15cm” />
    <auxiliary auxtype=”SensDet” auxvalue=”ICRU6”/>
</volume>
<volume name=”ICRUSpherePhantom7”>
    <materialref ref=”ICRU_Tissue”/>
    <solidref ref=”ICRUSphere15cm” />
    <auxiliary auxtype=”SensDet” auxvalue=”ICRU7”/>
</volume>
<volume name=”ICRUSpherePhantom8”>
    <materialref ref=”ICRU_Tissue”/>
    <solidref ref=”ICRUSphere15cm” />
    <auxiliary auxtype=”SensDet” auxvalue=”ICRU8”/>
</volume>
<volume name=”ICRUSpherePhantom9”>
    <materialref ref=”ICRU_Tissue”/>
    <solidref ref=”ICRUSphere15cm” />
    <auxiliary auxtype=”SensDet” auxvalue=”ICRU9”/>
</volume>
<volume name=”ICRUSpherePhantom10”>
    <materialref ref=”ICRU_Tissue”/>
    <solidref ref=”ICRUSphere15cm” />
    <auxiliary auxtype=”SensDet” auxvalue=”ICRU10”/>
</volume>
<volume name=”ICRUSpherePhantom11”>
    <materialref ref=”ICRU_Tissue”/>
    <solidref ref=”ICRUSphere15cm” />
    <auxiliary auxtype=”SensDet” auxvalue=”ICRU11”/>
</volume>
<volume name=”ICRUSpherePhantom12”>
    <materialref ref=”ICRU_Tissue”/>
    <solidref ref=”ICRUSphere15cm” />
    <auxiliary auxtype=”SensDet” auxvalue=”ICRU12”/>
</volume>
<volume name=”ICRUSpherePhantom13”>
    <materialref ref=”ICRU_Tissue”/>
    <solidref ref=”ICRUSphere15cm” />
    <auxiliary auxtype=”SensDet” auxvalue=”ICRU13”/>
</volume>
<volume name=”ICRUSpherePhantom14”>
    <materialref ref=”ICRU_Tissue”/>
    <solidref ref=”ICRUSphere15cm” />
    <auxiliary auxtype=”SensDet” auxvalue=”ICRU14”/>
</volume>
<volume name=”ICRUSpherePhantom15”>
    <materialref ref=”ICRU_Tissue”/>
    <solidref ref=”ICRUSphere15cm” />
    <auxiliary auxtype=”SensDet” auxvalue=”ICRU15”/>
</volume>
<!--Central Heat Shield and Structure -->

<volume name=”LV_Interior”>
```

```
<materialref ref=”Air”/>
<solidref ref=”Interior”/>
<physvol>
    <volumeref ref=”ICRUSpherePhantom1”/>
    <positionref ref=”ICRUPosition1”/>
</physvol>
<physvol>
    <volumeref ref=”ICRUSpherePhantom2”/>
    <positionref ref=”ICRUPosition2”/>
</physvol>
<physvol>
    <volumeref ref=”ICRUSpherePhantom3”/>
    <positionref ref=”ICRUPosition3”/>
</physvol>
<physvol>
    <volumeref ref=”ICRUSpherePhantom4”/>
    <positionref ref=”ICRUPosition4”/>
</physvol>
<physvol>
    <volumeref ref=”ICRUSpherePhantom5”/>
    <positionref ref=”ICRUPosition5”/>
</physvol>
<physvol>
    <volumeref ref=”ICRUSpherePhantom6”/>
    <positionref ref=”ICRUPosition6”/>
</physvol>
<physvol>
    <volumeref ref=”ICRUSpherePhantom7”/>
    <positionref ref=”ICRUPosition7”/>
</physvol>
<physvol>
    <volumeref ref=”ICRUSpherePhantom8”/>
    <positionref ref=”ICRUPosition8”/>
</physvol>
<physvol>
    <volumeref ref=”ICRUSpherePhantom9”/>
    <positionref ref=”ICRUPosition9”/>
</physvol>
<physvol>
    <volumeref ref=”ICRUSpherePhantom10”/>
    <positionref ref=”ICRUPosition10”/>
</physvol>
<physvol>
    <volumeref ref=”ICRUSpherePhantom11”/>
    <positionref ref=”ICRUPosition11”/>
</physvol>
<physvol>
    <volumeref ref=”ICRUSpherePhantom12”/>
    <positionref ref=”ICRUPosition12”/>
</physvol>
<physvol>
    <volumeref ref=”ICRUSpherePhantom13”/>
    <positionref ref=”ICRUPosition13”/>
</physvol>
<physvol>
    <volumeref ref=”ICRUSpherePhantom14”/>
    <positionref ref=”ICRUPosition14”/>
</physvol>
<physvol>
```

```
        <volumeref ref=”ICRUSpherePhantom15”/>
        <positionref ref=”ICRUPosition15”/>
    </physvol>
</volume>
<volume name=”LV_Aluminum_Inner_Plate”>
    <materialref ref=”Aluminum”/>
    <solidref ref=”Aluminum_Inner_Plate”/>
</volume>
<volume name=”LV_Aluminum_Honeycomb”>
    <materialref ref=”Aluminum_Honeycomb”/>
    <solidref ref=”Aluminum_Honeycomb_SD”/>
</volume>
<volume name=”LV_Aluminum_Outer_Plate”>
    <materialref ref=”Aluminum”/>
    <solidref ref=”Aluminum_Outer_Plate”/>
</volume>
<volume name=”LV_Insulation”>
    <materialref ref=”Insulation”/>
    <solidref ref=”Insulation_SD”/>
</volume>
<volume name=”LV_Stainless_Steel_Inner_Plate”>
    <materialref ref=”StainlessSteelPH14_8Mo”/>
    <solidref ref=”Stainless_Steel_Inner_Plate”/>
</volume>
<volume name=”LV_Saintless_Steel_Honeycomb”>
    <materialref ref=”StainlessSteelPH14_8Mo_Honeycomb”/>
    <solidref ref=”Saintless_Steel_Honeycomb”/>
</volume>
<volume name=”LV_Stainless_Steel_Outer_Plate”>
    <materialref ref=”StainlessSteelPH14_8Mo”/>
    <solidref ref=”Stainless_Steel_Outer_Plate”/>
</volume>
<volume name=”LV_Ablator”>
    <materialref ref=”Ablator”/>
    <solidref ref=”Ablator_SD”/>
</volume>
<volume name=”LV_Kapton”>
    <materialref ref=”Mylar”/>
    <solidref ref=”Kapton”/>
</volume>
<volume name=”LV_Central_Heat_Shield”>
    <materialref ref=”Vacuum”/>
    <solidref ref=”Central_Heat_Shield”/>
    <physvol>
        <volumeref ref=”LV_Kapton”/>
    </physvol>
    <physvol>
        <volumeref ref=”LV_Ablator”/>
    </physvol>
    <physvol>
        <volumeref ref=”LV_Stainless_Steel_Outer_Plate”/>
    </physvol>
    <physvol>
        <volumeref ref=”LV_Saintless_Steel_Honeycomb”/>
    </physvol>
    <physvol>
        <volumeref ref=”LV_Stainless_Steel_Inner_Plate”/>
    </physvol>
    <physvol>
```

```
        <volumeref ref=”LV_Insulation”/>
    </physvol>
    <physvol>
        <volumeref ref=”LV_Aluminum_Outer_Plate”/>
    </physvol>
    <physvol>
        <volumeref ref=”LV_Aluminum_Honeycomb”/>
    </physvol>
    <physvol>
        <volumeref ref=”LV_Aluminum_Inner_Plate”/>
    </physvol>
    <physvol>
        <volumeref ref=”LV_Interior”/>
    </physvol>
</volume>
<!--Aft Heat Shield and Structure -->
<volume name=”LV_Interior_Aft”> <materialref ref=”Air”/> <solidref ref=”
    Interior_Aft” />
</volume>
<volume name=”LV_Aluminum_Inner_Plate_Aft”> <materialref ref=”Aluminum”/
    > <solidref ref=”Aluminum_Inner_Plate_Aft” />
    <physvol>
        <volumeref ref=”LV_Interior_Aft”/>
    </physvol>
</volume>
<volume name=”LV_Aluminum_Honeycomb_Aft”> <materialref ref=”
    Aluminum_Honeycomb”/> <solidref ref=”Aluminum_Honeycomb_Aft” />
    <physvol>
        <volumeref ref=”LV_Aluminum_Inner_Plate_Aft”/>
    </physvol>
</volume>
<volume name=”LV_Aluminum_Outer_Plate_Aft”> <materialref ref=”Aluminum”/
    > <solidref ref=”Aluminum_Outer_Plate_Aft” />
    <physvol>
        <volumeref ref=”LV_Aluminum_Honeycomb_Aft”/>
    </physvol>
</volume>
<volume name=”LV_Insulation_Aft”> <materialref ref=”Insulation”/> <
    solidref ref=”Insulation_Aft” />
    <physvol>
        <volumeref ref=”LV_Aluminum_Outer_Plate_Aft”/>
    </physvol>
</volume>
<volume name=”LV_Stainless_Steel_Inner_Plate_Aft”> <materialref ref=”
    StainlessSteelPH14_8Mo”/> <solidref ref=”
    Stainless_Steel_Inner_Plate_Aft” />
    <physvol>
        <volumeref ref=”LV_Insulation_Aft”/>
    </physvol>
</volume>
<volume name=”LV_Saintless_Steel_Honeycomb_Aft”> <materialref ref=”
    StainlessSteelPH14_8Mo_Honeycomb”/> <solidref ref=”
    Saintless_Steel_Honeycomb_Aft” />
    <physvol>
        <volumeref ref=”LV_Stainless_Steel_Inner_Plate_Aft”/>
    </physvol>
</volume>
<volume name=”LV_Stainless_Steel_Outer_Plate_Aft”> <materialref ref=”
    StainlessSteelPH14_8Mo”/> <solidref ref=”
```

```
    Stainless_Steel_Outer_Plate_Aft” />
    <physvol>
        <volumeref ref=”LV_Saintless_Steel_Honeycomb_Aft”/>
    </physvol>
</volume>
<volume name=”LV_Ablator_Aft”> <materialref ref=”Ablator”/> <solidref
    ref=”Ablator_Aft” />
    <physvol>
        <volumeref ref=”LV_Stainless_Steel_Outer_Plate_Aft”/>
    </physvol>
</volume>
<volume name=”LV_Kapton_Aft”> <materialref ref=”Mylar”/> <solidref ref=”
    Kapton_Aft” />
    <physvol>
        <volumeref ref=”LV_Ablator_Aft”/>
    </physvol>
</volume>
<volume name=”LV_Aft_Heat_Shield”>
    <materialref ref=”Air”/>
    <solidref ref=”Aft_Heat_Shield” />
    <physvol>
        <volumeref ref=”LV_Kapton_Aft”/>
    </physvol>
</volume>
<!--Hatch Logic Volumes -->
<volume name=”LV_Kapton_Hatch”> <materialref ref=”Mylar”/> <solidref ref
    =”Kapton_Hatch” />
</volume>
<volume name=”LV_Insulation_Hatch”> <materialref ref=”Insulation”/> <
    solidref ref=”Insulation_Hatch” />
</volume>
<volume name=”LV_Aluminum_Outer_Plate_Hatch”> <materialref ref=”Aluminum
    ”/> <solidref ref=”Aluminum_Outer_Plate_Hatch” />
</volume>
<volume name=”LV_Aluminum_Honeycomb_Hatch”> <materialref ref=”
    Aluminum_Honeycomb”/> <solidref ref=”Aluminum_Honeycomb_Hatch” />
</volume>
<volume name=”LV_Aluminum_Inner_Plate_Hatch”> <materialref ref=”Aluminum
    ”/> <solidref ref=”Aluminum_Inner_Plate_Hatch” />
</volume>
<volume name=”LV_Forward_Hatch”> <materialref ref=”Vacuum”/> <solidref
    ref=”Forward_Hatch” />
    <physvol>
        <volumeref ref=”LV_Kapton_Hatch”/>
        <positionref ref=”Kapton_Hatch_Position”/>
    </physvol>
    <physvol>
        <volumeref ref=”LV_Insulation_Hatch”/>
        <positionref ref=”Insulation_Hatch_Position”/>
    </physvol>
    <physvol>
        <volumeref ref=”LV_Aluminum_Outer_Plate_Hatch”/>
        <positionref ref=”Aluminum_Outer_Hatch_Position”/>
    </physvol>
    <physvol>
        <volumeref ref=”LV_Aluminum_Honeycomb_Hatch”/>
        <positionref ref=”Aluminum_Honeycomb_Hatch_Position”/>
    </physvol>
    <physvol>
```

```
        <volumeref ref=”LV_Aluminum_Inner_Plate_Hatch”/>
        <positionref ref=”Aluminum_Inner_Hatch_Position”/>
    </physvol>
</volume>
<volume name=”LV_Kapton_Forward”> <materialref ref=”Mylar”/> <solidref
    ref=”Kapton_Forward” />
</volume>
<volume name=”LV_Ablator_Forward”> <materialref ref=”Ablator”/> <
    solidref ref=”Ablator_Forward” />
</volume>
<volume name=”LV_Stainless_Steel_Outer_Plate_Forward”> <materialref ref=
    ”StainlessSteelPH14_8Mo”/> <solidref ref=”
    Stainless_Steel_Outer_Plate_Forward” />
</volume>
<volume name=”LV_Saintless_Steel_Honeycomb_Forward”> <materialref ref=”
    StainlessSteelPH14_8Mo_Honeycomb”/> <solidref ref=”
    Saintless_Steel_Honeycomb_Forward” />
</volume>
<volume name=”LV_Stainless_Steel_Inner_Plate_Forward”> <materialref ref=
    ”StainlessSteelPH14_8Mo”/> <solidref ref=”
    Stainless_Steel_Inner_Plate_Forward” />
</volume>
<volume name=”LV_Forward_Heat_Shield”> <materialref ref=”Vacuum”/> <
    solidref ref=”Forward_Heat_Shield” />
    <physvol>
        <volumeref ref=”LV_Kapton_Forward”/>
    </physvol>
    <physvol>
        <volumeref ref=”LV_Ablator_Forward”/>
    </physvol>
    <physvol>
        <volumeref ref=”LV_Stainless_Steel_Outer_Plate_Forward”/>
    </physvol>
    <physvol>
        <volumeref ref=”LV_Saintless_Steel_Honeycomb_Forward”/>
    </physvol>
    <physvol>
        <volumeref ref=”LV_Stainless_Steel_Inner_Plate_Forward”/>
    </physvol>
</volume>
<!--Universe -->
<volume name=”LV_Universe”>
    <materialref ref=”Vacuum”/>
    <solidref ref=”UniverseBox”/>
    <physvol>
        <volumeref ref=”LV_Central_Heat_Shield”/>
        <positionref ref=”CM_Central_Position”/>
    </physvol>
    <physvol>
        <volumeref ref=”LV_Aft_Heat_Shield”/>
        <positionref ref=”CM_Bottom_Position”/>
    </physvol>
    <physvol>
        <volumeref ref=”LV_Forward_Hatch”/>
        <positionref ref=”CM_Hatch_Position”/>
    </physvol>
    <physvol>
        <volumeref ref=”LV_Forward_Heat_Shield”/>
        <positionref ref=”CM_Forward_Position”/>
```

```
            </physvol>
        </volume>
    </structure>
    <setup version=”1.0” name=”Default”>
        <world ref=”LV_Universe”/>
    </setup>
</gdml>
```

A.4 Apollo Command Module GDML Model 2

```
<?xml version=”1.0” encoding=”utf-8”?>
<gdml xmlns:xsi=”http://www.w3.org/2001/XMLSchema-instance”
    xsi:noNamespaceSchemaLocation=”gdml.xsd”>
        <define>
                <position name=”CM_Central_Position” unit=”cm” x=”0” y=”0” z=”
                    -120.65”/>
                <position name=”CM_Bottom_Position” unit=”cm” x=”0” y=”0” z=”
                    229.65”/>
                <position name=”subtraction” unit=”cm” x=”0” y=”0” z=”34.7”/>
                <position name=”CM_Hatch_Position” unit=”cm” x=”0” y=”0” z=”
                    123.03”/>
                <position name=”CM_Forward_Position” unit=”cm” x=”0” y=”0” z=”
                    57.3”/>
                <position name=”Kapton_Hatch_Position” unit=”cm” x=”0” y=”0” z=”
                    -2.32415”/>
                <position name=”Insulation_Hatch_Position” unit=”cm” x=”0” y=”0”
                     z=”-.58505”/>
                <position name=”Aluminum_Outer_Hatch_Position” unit=”cm” x=”0” y
                    =”0” z=”1.15405”/>
                <position name=”Aluminum_Honeycomb_Hatch_Position” unit=”cm” x=”
                    0” y=”0” z=”1.73905”/>
                <position name=”Aluminum_Inner_Hatch_Position” unit=”cm” x=”0” y
                    =”0” z=”2.32405”/>
                <!--ICRU Spheres Positions-->
                <position name=”ICRUPosition1” unit=”cm” x=”0” y=”0” z=”20”/>
                <position name=”ICRUPosition2” unit=”cm” x=”50” y=”0” z=”20”/>
                <position name=”ICRUPosition3” unit=”cm” x=”-50” y=”0” z=”20”/>
                <position name=”ICRUPosition4” unit=”cm” x=”0” y=”50” z=”20”/>
                <position name=”ICRUPosition5” unit=”cm” x=”0” y=”-50” z=”20”/>
                <position name=”ICRUPosition6” unit=”cm” x=”0” y=”0” z=”70”/>
                <position name=”ICRUPosition7” unit=”cm” x=”50” y=”0” z=”70”/>
                <position name=”ICRUPosition8” unit=”cm” x=”-50” y=”0” z=”70”/>
                <position name=”ICRUPosition9” unit=”cm” x=”0” y=”50” z=”70”/>
                <position name=”ICRUPosition10” unit=”cm” x=”0” y=”-50” z=”70”/>
                <position name=”ICRUPosition11” unit=”cm” x=”0” y=”0” z=”120”/>
                <position name=”ICRUPosition12” unit=”cm” x=”50” y=”0” z=”120”/>
                <position name=”ICRUPosition13” unit=”cm” x=”-50” y=”0” z=”120”/
                    >
                <position name=”ICRUPosition14” unit=”cm” x=”0” y=”50” z=”120”/>
                <position name=”ICRUPosition15” unit=”cm” x=”0” y=”-50” z=”120”/
                    >
        </define>
        <materials>
                <element Z=”1” formula=”H” name=”Hydrogen”>
                        <atom value=”1.00794”/>
                </element>
                <element Z=”6” formula=”C” name=”Carbon”>
                        <atom value=”12.0107”/>
                </element>
```

```
<element Z=”8” formula=”O” name=”Oxygen”>
        <atom value=”15.9994”/>
</element>
<element Z=”7” formula=”N” name=”Nitrogen”>
        <atom value=”14.0067”/>
</element>
<element Z=”9” formula=”F” name=”Fluorine”>
        <atom value=”18.998404”/>
</element>
<element Z=”13” formula=”Al” name=”Aluminium”>
        <atom value=”26.9815385”/>
</element>
<element Z=”14” formula=”Si” name=”Silicon”>
        <atom value=”28.0855”/>
</element>
<element Z=”15” formula=”P” name=”Phosphorus”>
        <atom value=”30.97376”/>
</element>
<element Z=”16” formula=”S” name=”Sulfur”>
        <atom value=”32.066”/>
</element>
<element Z=”20” formula=”Ca” name=”Calcium”>
        <atom value=”40.078”/>
</element>
<element Z=”24” formula=”Cr” name=”Chromium”>
        <atom value=”51.9961”/>
</element>
<element Z=”25” formula=”Mn” name=”Manganese”>
        <atom value=”54.93805”/>
</element>
<element Z=”26” formula=”Fe” name=”Iron”>
        <atom value=”55.845”/>
</element>
<element Z=”28” formula=”Ni” name=”Nickel”>
        <atom value=”58.6934”/>
</element>
<element Z=”42” formula=”Mo” name=”Molybdenum”>
        <atom value=”95.95”/>
</element>
<material formula=”C10H8O4␣” name=”Mylar”>
        <D value=”1.38”/>
        <composite n=”8” ref=”Hydrogen”/>
        <composite n=”10” ref=”Carbon”/>
        <composite n=”4” ref=”Oxygen”/>
</material>
<material formula=”␣” name=”Ablator”>
        <D value=”.51”/>
        <fraction ref=”Oxygen” n=”.4087”/>
        <fraction ref=”Silicon” n=”.1169”/>
        <fraction ref=”Carbon” n=”.4137”/>
        <fraction ref=”Hydrogen” n=”.0608”/>
</material>
<material formula=”␣” name=”StainlessSteelPH14_8Mo”>
        <D value=”7.82”/>
        <fraction ref=”Carbon” n=”0.0005”/>
        <fraction ref=”Silicon” n=”0.01”/>
        <fraction ref=”Manganese” n=”0.01”/>
        <fraction ref=”Phosphorus” n=”0.00015”/>
        <fraction ref=”Sulfur” n=”0.0001”/>
```

```
                <fraction ref=”Chromium” n=”0.15”/>
                <fraction ref=”Nickel” n=”0.0875”/>
                <fraction ref=”Molybdenum” n=”0.03”/>
                <fraction ref=”Aluminium” n=”0.015”/>
                <fraction ref=”Iron” n=”0.69675”/>
        </material>
        <material formula=”␣” name=”StainlessSteelPH14_8Mo_Honeycomb”>
                <D value=”.14”/>
                <fraction ref=”Carbon” n=”0.0005”/>
                <fraction ref=”Silicon” n=”0.01”/>
                <fraction ref=”Manganese” n=”0.01”/>
                <fraction ref=”Phosphorus” n=”0.00015”/>
                <fraction ref=”Sulfur” n=”0.0001”/>
                <fraction ref=”Chromium” n=”0.15”/>
                <fraction ref=”Nickel” n=”0.0875”/>
                <fraction ref=”Molybdenum” n=”0.03”/>
                <fraction ref=”Aluminium” n=”0.015”/>
                <fraction ref=”Iron” n=”0.69675”/>
        </material>
        <material Z=”13” formula=”␣” name=”Aluminum”>
                <D value=”2.70”/>
                <atom value=”26.98”/>
        </material>
        <material formula=”␣” name=”Insulation”>
                <D value=”.056”/>
                <fraction ref=”Oxygen” n=”.5009”/>
                <fraction ref=”Silicon” n=”.4586”/>
                <fraction ref=”Carbon” n=”.0324”/>
                <fraction ref=”Hydrogen” n=”.0082”/>
        </material>
        <material Z=”13” formula=”␣” name=”Aluminum_Honeycomb”>
                <D value=”.0497”/>
                <atom value=”26.98”/>
        </material>
        <material Z=”1” formula=”␣” name=”Vacuum”>
                <D value=”1e-25”/>
                <atom value=”1.01”/>
        </material>
        <material formula=”␣” name=”Air”>
                <D value=”0.00125”/>
                <fraction n=”0.79” ref=”Nitrogen”/>
                <fraction n=”0.21” ref=”Oxygen”/>
        </material>
        <material Z=”13” formula=”␣” name=”Racks_Aluminum”>
                <D value=”1”/>
                <atom value=”26.98”/>
        </material>
        <material formula=”␣” name=”ICRU_Tissue”>
                <D value=”1”/>
                <fraction n=”0.762” ref=”Oxygen”/>
                <fraction n=”0.111” ref=”Carbon”/>
                <fraction n=”0.101” ref=”Hydrogen”/>
                <fraction n=”0.026” ref=”Nitrogen”/>
        </material>
</materials>
<solids>
        <!-- -->
        <box name=”UniverseBox” lunit=”m” x=”10” y=”10” z=”10”/>
        <!--Central Heat Shield and Structure -->
```

```
<polycone name=”Central_Heat_Shield” startphi=”␣0” deltaphi=”360
    ” aunit=”degree” lunit=”cm”>
        <zplane z=”0” rmax=”195.58” rmin=”0”/>
        <zplane z=”177.8” rmax=”99.07” rmin=”0”/>
        <zplane z=”178” rmax=”57.15” rmin=”0”/>
        <zplane z=”241.3” rmax=”45.73” rmin=”0”/>
</polycone>
<polycone name=”Kapton” startphi=”␣0” deltaphi=”360” aunit=”
    degree” lunit=”cm”>
        <zplane z=”0” rmax=”195.58” rmin=”195.48”/>
        <zplane z=”177.8” rmax=”99.06” rmin=”98.96”/>
        <zplane z=”178” rmax=”57.15” rmin=”57.05”/>
        <zplane z=”241.3” rmax=”45.72” rmin=”45.62”/>
</polycone>
<polycone name=”Ablator_SD” startphi=”␣0” deltaphi=”360” aunit=”
    degree” lunit=”cm”>
        <zplane z=”0” rmax=”195.48” rmin=”193.194”/>
        <zplane z=”177.8” rmax=”98.96” rmin=”96.674”/>
        <zplane z=”178” rmax=”57.05” rmin=”54.764”/>
        <zplane z=”241.3” rmax=”45.62” rmin=”43.334”/>
</polycone>
<polycone name=”Stainless_Steel_Outer_Plate” startphi=”␣0”
    deltaphi=”360” aunit=”degree” lunit=”cm”>
        <zplane z=”0” rmax=”193.194” rmin=”193.004”/>
        <zplane z=”177.8” rmax=”96.674” rmin=”96.484”/>
        <zplane z=”178” rmax=”54.764” rmin=”54.574”/>
        <zplane z=”241.3” rmax=”43.334” rmin=”43.144”/>
</polycone>
<polycone name=”Saintless_Steel_Honeycomb” startphi=”␣0”
    deltaphi=”360” aunit=”degree” lunit=”cm”>
        <zplane z=”0” rmax=”193.004” rmin=”192.114”/>
        <zplane z=”177.8” rmax=”96.484” rmin=”95.594”/>
        <zplane z=”178” rmax=”54.574” rmin=”53.684”/>
        <zplane z=”241.3” rmax=”43.144” rmin=”42.254”/>
</polycone>
<polycone name=”Stainless_Steel_Inner_Plate” startphi=”␣0”
    deltaphi=”360” aunit=”degree” lunit=”cm”>
        <zplane z=”0” rmax=”192.114” rmin=”191.924”/>
        <zplane z=”177.8” rmax=”95.594” rmin=”95.404”/>
        <zplane z=”178” rmax=”53.684” rmin=”53.494”/>
        <zplane z=”241.3” rmax=”42.254” rmin=”42.064”/>
</polycone>
<polycone name=”Insulation_SD” startphi=”␣0” deltaphi=”360”
    aunit=”degree” lunit=”cm”>
        <zplane z=”0” rmax=”191.924” rmin=”188.5458”/>
        <zplane z=”177.8” rmax=”95.404” rmin=”92.0258”/>
        <zplane z=”178” rmax=”53.494” rmin=”50.1158”/>
        <zplane z=”241.3” rmax=”42.064” rmin=”38.6858”/>
</polycone>
<polycone name=”Aluminum_Outer_Plate” startphi=”␣0” deltaphi=”
    360” aunit=”degree” lunit=”cm”>
        <zplane z=”0” rmax=”188.5458” rmin=”188.4458”/>
        <zplane z=”177.8” rmax=”92.0258” rmin=”91.9258”/>
        <zplane z=”178” rmax=”50.1158” rmin=”50.0158”/>
        <zplane z=”241.3” rmax=”38.6858” rmin=”38.5858”/>
</polycone>
<polycone name=”Aluminum_Honeycomb_SD” startphi=”␣0” deltaphi=”
    360” aunit=”degree” lunit=”cm”>
        <zplane z=”0” rmax=”188.4458” rmin=”185.0458”/>
```

```
        <zplane z=”177.8” rmax=”91.9258” rmin=”90.8558”/>
        <zplane z=”178” rmax=”50.0158” rmin=”48.9458”/>
        <zplane z=”241.3” rmax=”38.5858” rmin=”37.5158”/>
</polycone>
<polycone name=”Aluminum_Inner_Plate” startphi=”␣0” deltaphi=”
    360” aunit=”degree” lunit=”cm”>
        <zplane z=”0” rmax=”185.0458” rmin=”184.9458”/>
        <zplane z=”177.8” rmax=”90.8558” rmin=”90.7558”/>
        <zplane z=”178” rmax=”48.9458” rmin=”48.8458”/>
        <zplane z=”241.3” rmax=”37.5158” rmin=”37.4158”/>
</polycone>
<polycone name=”Interior” startphi=”␣0” deltaphi=”360” aunit=”
    degree” lunit=”cm”>
        <zplane z=”0” rmax=”184.9458” rmin=”0”/>
        <zplane z=”177.8” rmax=”90.7558” rmin=”0”/>
        <zplane z=”178” rmax=”48.8458” rmin=”0”/>
        <zplane z=”241.3” rmax=”37.4158” rmin=”0”/>
</polycone>
<polycone name=”Equipment_Racks” startphi=”␣0” deltaphi=”360”
    aunit=”degree” lunit=”cm”>
        <zplane z=”0” rmax=”184” rmin=”164”/>
        <zplane z=”177.8” rmax=”90” rmin=”75”/>
</polycone>
<!--Aft Heat Shield -->
<tube name=”sub_tube” startphi=”0” deltaphi=”360” aunit=”degree”
     lunit=”cm” rmax=”410” z=”770”/>
<sphere name=”Aft_Heat_Shield_S” startphi=”0” deltaphi=”360”
    aunit=”degree” lunit=”cm” starttheta=”0” deltatheta=”180”
    rmax=”401.90” rmin=”0”/>
<subtraction name=”Aft_Heat_Shield”>
        <first ref=”Aft_Heat_Shield_S”/>
        <second ref=”sub_tube”/>
        <positionref ref=”subtraction”/>
</subtraction>
<sphere name=”Kapton_Aft_S” startphi=”0” deltaphi=”360” aunit=”
    degree” lunit=”cm” starttheta=”0” deltatheta=”180” rmax=”
    401.8915” rmin=”0”/>
<subtraction name=”Kapton_Aft”>
        <first ref=”Kapton_Aft_S”/>
        <second ref=”sub_tube”/>
        <positionref ref=”subtraction”/>
</subtraction>
<sphere name=”Ablator_Aft_S” startphi=”0” deltaphi=”360” aunit=”
    degree” lunit=”cm” starttheta=”0” deltatheta=”180” rmax=”
    401.7915” rmin=”0”/>
<subtraction name=”Ablator_Aft”>
        <first ref=”Ablator_Aft_S”/>
        <second ref=”sub_tube”/>
        <positionref ref=”subtraction”/>
</subtraction>
<sphere name=”Stainless_Steel_Outer_Plate_Aft_S” startphi=”0”
    deltaphi=”360” aunit=”degree” lunit=”cm” starttheta=”0”
    deltatheta=”180” rmax=”394.9335” rmin=”0”/>
<subtraction name=”Stainless_Steel_Outer_Plate_Aft”>
        <first ref=”Stainless_Steel_Outer_Plate_Aft_S”/>
        <second ref=”sub_tube”/>
        <positionref ref=”subtraction”/>
</subtraction>
<sphere name=”Saintless_Steel_Honeycomb_Aft_S” startphi=”0”
```

```
    deltaphi=”360” aunit=”degree” lunit=”cm” starttheta=”0”
    deltatheta=”180” rmax=”394.7435” rmin=”0”/>
<subtraction name=”Saintless_Steel_Honeycomb_Aft”>
        <first ref=”Saintless_Steel_Honeycomb_Aft_S”/>
        <second ref=”sub_tube”/>
        <positionref ref=”subtraction”/>
</subtraction>
<sphere name=”Stainless_Steel_Inner_Plate_Aft_S” startphi=”0”
    deltaphi=”360” aunit=”degree” lunit=”cm” starttheta=”0”
    deltatheta=”180” rmax=”390.0435” rmin=”0”/>
<subtraction name=”Stainless_Steel_Inner_Plate_Aft”>
        <first ref=”Stainless_Steel_Inner_Plate_Aft_S”/>
        <second ref=”sub_tube”/>
        <positionref ref=”subtraction”/>
</subtraction>
<sphere name=”Insulation_Aft_S” startphi=”0” deltaphi=”360”
    aunit=”degree” lunit=”cm” starttheta=”0” deltatheta=”180”
    rmax=”389.8535” rmin=”0”/>
<subtraction name=”Insulation_Aft”>
        <first ref=”Insulation_Aft_S”/>
        <second ref=”sub_tube”/>
        <positionref ref=”subtraction”/>
</subtraction>
<sphere name=”Aluminum_Outer_Plate_Aft_S” startphi=”0” deltaphi=
    ”360” aunit=”degree” lunit=”cm” starttheta=”0” deltatheta=”
    180” rmax=”387.8215” rmin=”0”/>
<subtraction name=”Aluminum_Outer_Plate_Aft”>
        <first ref=”Aluminum_Outer_Plate_Aft_S”/>
        <second ref=”sub_tube”/>
        <positionref ref=”subtraction”/>
</subtraction>
<sphere name=”Aluminum_Honeycomb_Aft_S” startphi=”0” deltaphi=”
    360” aunit=”degree” lunit=”cm” starttheta=”0” deltatheta=”
    180” rmax=”387.7215” rmin=”0”/>
<subtraction name=”Aluminum_Honeycomb_Aft”>
        <first ref=”Aluminum_Honeycomb_Aft_S”/>
        <second ref=”sub_tube”/>
        <positionref ref=”subtraction”/>
</subtraction>
<sphere name=”Aluminum_Inner_Plate_Aft_S” startphi=”0” deltaphi=
    ”360” aunit=”degree” lunit=”cm” starttheta=”0” deltatheta=”
    180” rmax=”384.3215” rmin=”0”/>
<subtraction name=”Aluminum_Inner_Plate_Aft”>
        <first ref=”Aluminum_Inner_Plate_Aft_S”/>
        <second ref=”sub_tube”/>
        <positionref ref=”subtraction”/>
</subtraction>
<sphere name=”Interior_Aft_S” startphi=”0” deltaphi=”360” aunit=
    ”degree” lunit=”cm” starttheta=”0” deltatheta=”180” rmax=”
    384.2215” rmin=”0”/>
<subtraction name=”Interior_Aft”>
        <first ref=”Interior_Aft_S”/>
        <second ref=”sub_tube”/>
        <positionref ref=”subtraction”/>
</subtraction>
<sphere name=”Equipment_Rack_Aft_S” startphi=”0” deltaphi=”360”
    aunit=”degree” lunit=”cm” starttheta=”0” deltatheta=”180”
    rmax=”380” rmin=”370”/>
<subtraction name=”Equipment_Rack_Aft”>
```

```
        <first ref=”Equipment_Rack_Aft_S”/>
        <second ref=”sub_tube”/>
        <positionref ref=”subtraction”/>
</subtraction>
<!--Interior -->
<polycone name=”Interior_Central” startphi=”␣0” deltaphi=”360”
    aunit=”degree” lunit=”cm”>
        <zplane z=”0” rmax=”184.9458” rmin=”0”/>
        <zplane z=”177.8” rmax=”90.7558” rmin=”0”/>
        <zplane z=”178” rmax=”48.8458” rmin=”0”/>
        <zplane z=”241.3” rmax=”37.4158” rmin=”0”/>
</polycone>
<!--Forward Hatch -->
<tube name=”Forward_Hatch” startphi=”0” deltaphi=”360” aunit=”
    degree” lunit=”cm” z=”4.7483” rmax=”45.7”/>
<tube name=”Kapton_Hatch” startphi=”0” deltaphi=”360” aunit=”
    degree” lunit=”cm” z=”0.1” rmax=”45.7”/>
<tube name=”Insulation_Hatch” startphi=”0” deltaphi=”360” aunit=
    ”degree” lunit=”cm” z=”3.3782” rmax=”45.7”/>
<tube name=”Aluminum_Outer_Plate_Hatch” startphi=”0” deltaphi=”
    360” aunit=”degree” lunit=”cm” z=”0.1” rmax=”45.7”/>
<tube name=”Aluminum_Honeycomb_Hatch” startphi=”0” deltaphi=”360
    ” aunit=”degree” lunit=”cm” z=”1.07” rmax=”45.7”/>
<tube name=”Aluminum_Inner_Plate_Hatch” startphi=”0” deltaphi=”
    360” aunit=”degree” lunit=”cm” z=”0.1” rmax=”45.7”/>
<!--Forward Heat Shield -->
<polycone name=”Forward_Heat_Shield” startphi=”␣0” deltaphi=”360
    ” aunit=”degree” lunit=”cm”>
        <zplane z=”0” rmax=”99” rmin=”95”/>
        <zplane z=”73.3” rmax=”49.656” rmin=”46”/>
</polycone>
<polycone name=”Kapton_Forward” startphi=”␣0” deltaphi=”360”
    aunit=”degree” lunit=”cm”>
        <zplane z=”0” rmax=”99” rmin=”98.9”/>
        <zplane z=”73.3” rmax=”49.656” rmin=”49.556”/>
</polycone>
<polycone name=”Ablator_Forward” startphi=”␣0” deltaphi=”360”
    aunit=”degree” lunit=”cm”>
        <zplane z=”0” rmax=”98.9” rmin=”96.614”/>
        <zplane z=”73.3” rmax=”49.556” rmin=”47.27”/>
</polycone>
<polycone name=”Stainless_Steel_Outer_Plate_Forward” startphi=”␣
    0” deltaphi=”360” aunit=”degree” lunit=”cm”>
        <zplane z=”0” rmax=”96.614” rmin=”96.424”/>
        <zplane z=”73.3” rmax=”47.27” rmin=”47.08”/>
</polycone>
<polycone name=”Saintless_Steel_Honeycomb_Forward” startphi=”␣0”
     deltaphi=”360” aunit=”degree” lunit=”cm”>
        <zplane z=”0” rmax=”96.424” rmin=”95.534”/>
        <zplane z=”73.3” rmax=”47.08” rmin=”46.19”/>
</polycone>
<polycone name=”Stainless_Steel_Inner_Plate_Forward” startphi=”␣
    0” deltaphi=”360” aunit=”degree” lunit=”cm”>
        <zplane z=”0” rmax=”95.534” rmin=”95.344”/>
        <zplane z=”73.3” rmax=”46.19” rmin=”46”/>
</polycone>
<sphere name=”ICRUSphere15cm” aunit=”degree” deltaphi=”360”
    deltatheta=”180” lunit=”mm” rmax=”150” rmin=”0” startphi=”0”
     starttheta=”0”/>
```

```
</solids>
<structure>
        <!--ICRU Spheres-->
        <volume name=”ICRUSpherePhantom1”>
                <materialref ref=”ICRU_Tissue”/>
                <solidref ref=”ICRUSphere15cm”/>
                <auxiliary auxtype=”SensDet” auxvalue=”ICRU1”/>
        </volume>
        <volume name=”ICRUSpherePhantom2”>
                <materialref ref=”ICRU_Tissue”/>
                <solidref ref=”ICRUSphere15cm”/>
                <auxiliary auxtype=”SensDet” auxvalue=”ICRU2”/>
        </volume>
        <volume name=”ICRUSpherePhantom3”>
                <materialref ref=”ICRU_Tissue”/>
                <solidref ref=”ICRUSphere15cm”/>
                <auxiliary auxtype=”SensDet” auxvalue=”ICRU3”/>
        </volume>
        <volume name=”ICRUSpherePhantom4”>
                <materialref ref=”ICRU_Tissue”/>
                <solidref ref=”ICRUSphere15cm”/>
                <auxiliary auxtype=”SensDet” auxvalue=”ICRU4”/>
        </volume>
        <volume name=”ICRUSpherePhantom5”>
                <materialref ref=”ICRU_Tissue”/>
                <solidref ref=”ICRUSphere15cm”/>
                <auxiliary auxtype=”SensDet” auxvalue=”ICRU5”/>
        </volume>
        <volume name=”ICRUSpherePhantom6”>
                <materialref ref=”ICRU_Tissue”/>
                <solidref ref=”ICRUSphere15cm”/>
                <auxiliary auxtype=”SensDet” auxvalue=”ICRU6”/>
        </volume>
        <volume name=”ICRUSpherePhantom7”>
                <materialref ref=”ICRU_Tissue”/>
                <solidref ref=”ICRUSphere15cm”/>
                <auxiliary auxtype=”SensDet” auxvalue=”ICRU7”/>
        </volume>
        <volume name=”ICRUSpherePhantom8”>
                <materialref ref=”ICRU_Tissue”/>
                <solidref ref=”ICRUSphere15cm”/>
                <auxiliary auxtype=”SensDet” auxvalue=”ICRU8”/>
        </volume>
        <volume name=”ICRUSpherePhantom9”>
                <materialref ref=”ICRU_Tissue”/>
                <solidref ref=”ICRUSphere15cm”/>
                <auxiliary auxtype=”SensDet” auxvalue=”ICRU9”/>
        </volume>
        <volume name=”ICRUSpherePhantom10”>
                <materialref ref=”ICRU_Tissue”/>
                <solidref ref=”ICRUSphere15cm”/>
                <auxiliary auxtype=”SensDet” auxvalue=”ICRU10”/>
        </volume>
        <volume name=”ICRUSpherePhantom11”>
                <materialref ref=”ICRU_Tissue”/>
                <solidref ref=”ICRUSphere15cm”/>
                <auxiliary auxtype=”SensDet” auxvalue=”ICRU11”/>
        </volume>
        <volume name=”ICRUSpherePhantom12”>
```

```
        <materialref ref=”ICRU_Tissue”/>
        <solidref ref=”ICRUSphere15cm”/>
        <auxiliary auxtype=”SensDet” auxvalue=”ICRU12”/>
</volume>
<volume name=”ICRUSpherePhantom13”>
        <materialref ref=”ICRU_Tissue”/>
        <solidref ref=”ICRUSphere15cm”/>
        <auxiliary auxtype=”SensDet” auxvalue=”ICRU13”/>
</volume>
<volume name=”ICRUSpherePhantom14”>
        <materialref ref=”ICRU_Tissue”/>
        <solidref ref=”ICRUSphere15cm”/>
        <auxiliary auxtype=”SensDet” auxvalue=”ICRU14”/>
</volume>
<volume name=”ICRUSpherePhantom15”>
        <materialref ref=”ICRU_Tissue”/>
        <solidref ref=”ICRUSphere15cm”/>
        <auxiliary auxtype=”SensDet” auxvalue=”ICRU15”/>
</volume>
<volume name=”LV_Equipment_Racks”>
        <materialref ref=”Racks_Aluminum”/>
        <solidref ref=”Equipment_Racks”/>
</volume>
<!--Central Heat Shield and Structure -->
<volume name=”LV_Interior”>
        <materialref ref=”Air”/>
        <solidref ref=”Interior”/>
        <physvol>
                <volumeref ref=”LV_Equipment_Racks”/>
        </physvol>
        <physvol>
                <volumeref ref=”ICRUSpherePhantom1”/>
                <positionref ref=”ICRUPosition1”/>
        </physvol>
        <physvol>
                <volumeref ref=”ICRUSpherePhantom2”/>
                <positionref ref=”ICRUPosition2”/>
        </physvol>
        <physvol>
                <volumeref ref=”ICRUSpherePhantom3”/>
                <positionref ref=”ICRUPosition3”/>
        </physvol>
        <physvol>
                <volumeref ref=”ICRUSpherePhantom4”/>
                <positionref ref=”ICRUPosition4”/>
        </physvol>
        <physvol>
                <volumeref ref=”ICRUSpherePhantom5”/>
                <positionref ref=”ICRUPosition5”/>
        </physvol>
        <physvol>
                <volumeref ref=”ICRUSpherePhantom6”/>
                <positionref ref=”ICRUPosition6”/>
        </physvol>
        <physvol>
                <volumeref ref=”ICRUSpherePhantom7”/>
                <positionref ref=”ICRUPosition7”/>
        </physvol>
        <physvol>
```

```
                                <volumeref ref=”ICRUSpherePhantom8”/>
                                <positionref ref=”ICRUPosition8”/>
                        </physvol>
                        <physvol>
                                <volumeref ref=”ICRUSpherePhantom9”/>
                                <positionref ref=”ICRUPosition9”/>
                        </physvol>
                        <physvol>
                                <volumeref ref=”ICRUSpherePhantom10”/>
                                <positionref ref=”ICRUPosition10”/>
                        </physvol>
                        <physvol>
                                <volumeref ref=”ICRUSpherePhantom11”/>
                                <positionref ref=”ICRUPosition11”/>
                        </physvol>
                        <physvol>
                                <volumeref ref=”ICRUSpherePhantom12”/>
                                <positionref ref=”ICRUPosition12”/>
                        </physvol>
                        <physvol>
                                <volumeref ref=”ICRUSpherePhantom13”/>
                                <positionref ref=”ICRUPosition13”/>
                        </physvol>
                        <physvol>
                                <volumeref ref=”ICRUSpherePhantom14”/>
                                <positionref ref=”ICRUPosition14”/>
                        </physvol>
                        <physvol>
                                <volumeref ref=”ICRUSpherePhantom15”/>
                                <positionref ref=”ICRUPosition15”/>
                        </physvol>
                </volume>
                <volume name=”LV_Aluminum_Inner_Plate”>
                        <materialref ref=”Aluminum”/>
                        <solidref ref=”Aluminum_Inner_Plate”/>
                </volume>
                <volume name=”LV_Aluminum_Honeycomb”>
                        <materialref ref=”Aluminum_Honeycomb”/>
                        <solidref ref=”Aluminum_Honeycomb_SD”/>
                </volume>
                <volume name=”LV_Aluminum_Outer_Plate”>
                        <materialref ref=”Aluminum”/>
                        <solidref ref=”Aluminum_Outer_Plate”/>
                </volume>
                <volume name=”LV_Insulation”>
                        <materialref ref=”Insulation”/>
                        <solidref ref=”Insulation_SD”/>
                </volume>
                <volume name=”LV_Stainless_Steel_Inner_Plate”>
                        <materialref ref=”StainlessSteelPH14_8Mo”/>
                        <solidref ref=”Stainless_Steel_Inner_Plate”/>
                </volume>
                <volume name=”LV_Saintless_Steel_Honeycomb”>
                        <materialref ref=”StainlessSteelPH14_8Mo_Honeycomb”/>
                        <solidref ref=”Saintless_Steel_Honeycomb”/>
                </volume>
                <volume name=”LV_Stainless_Steel_Outer_Plate”>
                        <materialref ref=”StainlessSteelPH14_8Mo”/>
                        <solidref ref=”Stainless_Steel_Outer_Plate”/>
```

```
</volume>
<volume name="LV_Ablator">
        <materialref ref="Ablator"/>
        <solidref ref="Ablator_SD"/>
</volume>
<volume name="LV_Kapton">
        <materialref ref="Mylar"/>
        <solidref ref="Kapton"/>
</volume>
<volume name="LV_Central_Heat_Shield">
        <materialref ref="Vacuum"/>
        <solidref ref="Central_Heat_Shield"/>
        <physvol>
                <volumeref ref="LV_Kapton"/>
        </physvol>
        <physvol>
                <volumeref ref="LV_Ablator"/>
        </physvol>
        <physvol>
                <volumeref ref="LV_Stainless_Steel_Outer_Plate"/
                    >
        </physvol>
        <physvol>
                <volumeref ref="LV_Saintless_Steel_Honeycomb"/>
        </physvol>
        <physvol>
                <volumeref ref="LV_Stainless_Steel_Inner_Plate"/
                    >
        </physvol>
        <physvol>
                <volumeref ref="LV_Insulation"/>
        </physvol>
        <physvol>
                <volumeref ref="LV_Aluminum_Outer_Plate"/>
        </physvol>
        <physvol>
                <volumeref ref="LV_Aluminum_Honeycomb"/>
        </physvol>
        <physvol>
                <volumeref ref="LV_Aluminum_Inner_Plate"/>
        </physvol>
        <physvol>
                <volumeref ref="LV_Interior"/>
        </physvol>
</volume>
<!--Aft Heat Shield and Structure -->
<volume name="LV_Equipment_Rack_Aft">
        <materialref ref="Racks_Aluminum"/>
        <solidref ref="Equipment_Rack_Aft"/>
</volume>
<volume name="LV_Interior_Aft">
        <materialref ref="Air"/>
        <solidref ref="Interior_Aft"/>
        <physvol>
                <volumeref ref="LV_Equipment_Rack_Aft"/>
        </physvol>
</volume>
<volume name="LV_Aluminum_Inner_Plate_Aft">
        <materialref ref="Aluminum"/>
```

```
        <solidref ref=”Aluminum_Inner_Plate_Aft”/>
        <physvol>
                <volumeref ref=”LV_Interior_Aft”/>
        </physvol>
</volume>
<volume name=”LV_Aluminum_Honeycomb_Aft”>
        <materialref ref=”Aluminum_Honeycomb”/>
        <solidref ref=”Aluminum_Honeycomb_Aft”/>
        <physvol>
                <volumeref ref=”LV_Aluminum_Inner_Plate_Aft”/>
        </physvol>
</volume>
<volume name=”LV_Aluminum_Outer_Plate_Aft”>
        <materialref ref=”Aluminum”/>
        <solidref ref=”Aluminum_Outer_Plate_Aft”/>
        <physvol>
                <volumeref ref=”LV_Aluminum_Honeycomb_Aft”/>
        </physvol>
</volume>
<volume name=”LV_Insulation_Aft”>
        <materialref ref=”Insulation”/>
        <solidref ref=”Insulation_Aft”/>
        <physvol>
                <volumeref ref=”LV_Aluminum_Outer_Plate_Aft”/>
        </physvol>
</volume>
<volume name=”LV_Stainless_Steel_Inner_Plate_Aft”>
        <materialref ref=”StainlessSteelPH14_8Mo”/>
        <solidref ref=”Stainless_Steel_Inner_Plate_Aft”/>
        <physvol>
                <volumeref ref=”LV_Insulation_Aft”/>
        </physvol>
</volume>
<volume name=”LV_Saintless_Steel_Honeycomb_Aft”>
        <materialref ref=”StainlessSteelPH14_8Mo_Honeycomb”/>
        <solidref ref=”Saintless_Steel_Honeycomb_Aft”/>
        <physvol>
                <volumeref ref=”
                    LV_Stainless_Steel_Inner_Plate_Aft”/>
        </physvol>
</volume>
<volume name=”LV_Stainless_Steel_Outer_Plate_Aft”>
        <materialref ref=”StainlessSteelPH14_8Mo”/>
        <solidref ref=”Stainless_Steel_Outer_Plate_Aft”/>
        <physvol>
                <volumeref ref=”LV_Saintless_Steel_Honeycomb_Aft
                    ”/>
        </physvol>
</volume>
<volume name=”LV_Ablator_Aft”>
        <materialref ref=”Ablator”/>
        <solidref ref=”Ablator_Aft”/>
        <physvol>
                <volumeref ref=”
                    LV_Stainless_Steel_Outer_Plate_Aft”/>
        </physvol>
</volume>
<volume name=”LV_Kapton_Aft”>
        <materialref ref=”Mylar”/>
```

```
                <solidref ref=”Kapton_Aft”/>
                <physvol>
                        <volumeref ref=”LV_Ablator_Aft”/>
                </physvol>
        </volume>
        <volume name=”LV_Aft_Heat_Shield”>
                <materialref ref=”Air”/>
                <solidref ref=”Aft_Heat_Shield”/>
                <physvol>
                        <volumeref ref=”LV_Kapton_Aft”/>
                </physvol>
        </volume>
        <!--Hatch Logic Volumes -->
        <volume name=”LV_Kapton_Hatch”>
                <materialref ref=”Mylar”/>
                <solidref ref=”Kapton_Hatch”/>
        </volume>
        <volume name=”LV_Insulation_Hatch”>
                <materialref ref=”Insulation”/>
                <solidref ref=”Insulation_Hatch”/>
        </volume>
        <volume name=”LV_Aluminum_Outer_Plate_Hatch”>
                <materialref ref=”Aluminum”/>
                <solidref ref=”Aluminum_Outer_Plate_Hatch”/>
        </volume>
        <volume name=”LV_Aluminum_Honeycomb_Hatch”>
                <materialref ref=”Aluminum_Honeycomb”/>
                <solidref ref=”Aluminum_Honeycomb_Hatch”/>
        </volume>
        <volume name=”LV_Aluminum_Inner_Plate_Hatch”>
                <materialref ref=”Aluminum”/>
                <solidref ref=”Aluminum_Inner_Plate_Hatch”/>
        </volume>
        <volume name=”LV_Forward_Hatch”>
                <materialref ref=”Vacuum”/>
                <solidref ref=”Forward_Hatch”/>
                <physvol>
                        <volumeref ref=”LV_Kapton_Hatch”/>
                        <positionref ref=”Kapton_Hatch_Position”/>
                </physvol>
                <physvol>
                        <volumeref ref=”LV_Insulation_Hatch”/>
                        <positionref ref=”Insulation_Hatch_Position”/>
                </physvol>
                <physvol>
                        <volumeref ref=”LV_Aluminum_Outer_Plate_Hatch”/>
                        <positionref ref=”Aluminum_Outer_Hatch_Position”
                            />
                </physvol>
                <physvol>
                        <volumeref ref=”LV_Aluminum_Honeycomb_Hatch”/>
                        <positionref ref=”
                            Aluminum_Honeycomb_Hatch_Position”/>
                </physvol>
                <physvol>
                        <volumeref ref=”LV_Aluminum_Inner_Plate_Hatch”/>
                        <positionref ref=”Aluminum_Inner_Hatch_Position”
                            />
                </physvol>
```

```
</volume>
<volume name=”LV_Kapton_Forward”>
        <materialref ref=”Mylar”/>
        <solidref ref=”Kapton_Forward”/>
</volume>
<volume name=”LV_Ablator_Forward”>
        <materialref ref=”Ablator”/>
        <solidref ref=”Ablator_Forward”/>
</volume>
<volume name=”LV_Stainless_Steel_Outer_Plate_Forward”>
        <materialref ref=”StainlessSteelPH14_8Mo”/>
        <solidref ref=”Stainless_Steel_Outer_Plate_Forward”/>
</volume>
<volume name=”LV_Saintless_Steel_Honeycomb_Forward”>
        <materialref ref=”StainlessSteelPH14_8Mo_Honeycomb”/>
        <solidref ref=”Saintless_Steel_Honeycomb_Forward”/>
</volume>
<volume name=”LV_Stainless_Steel_Inner_Plate_Forward”>
        <materialref ref=”StainlessSteelPH14_8Mo”/>
        <solidref ref=”Stainless_Steel_Inner_Plate_Forward”/>
</volume>
<volume name=”LV_Forward_Heat_Shield”>
        <materialref ref=”Vacuum”/>
        <solidref ref=”Forward_Heat_Shield”/>
        <physvol>
                <volumeref ref=”LV_Kapton_Forward”/>
        </physvol>
        <physvol>
                <volumeref ref=”LV_Ablator_Forward”/>
        </physvol>
        <physvol>
                <volumeref ref=”
                    LV_Stainless_Steel_Outer_Plate_Forward”/>
        </physvol>
        <physvol>
                <volumeref ref=”
                    LV_Saintless_Steel_Honeycomb_Forward”/>
        </physvol>
        <physvol>
                <volumeref ref=”
                    LV_Stainless_Steel_Inner_Plate_Forward”/>
        </physvol>
</volume>
<!--Universe -->
<volume name=”LV_Universe”>
        <materialref ref=”Vacuum”/>
        <solidref ref=”UniverseBox”/>
        <physvol>
                <volumeref ref=”LV_Central_Heat_Shield”/>
                <positionref ref=”CM_Central_Position”/>
        </physvol>
        <physvol>
                <volumeref ref=”LV_Aft_Heat_Shield”/>
                <positionref ref=”CM_Bottom_Position”/>
        </physvol>
        <physvol>
                <volumeref ref=”LV_Forward_Hatch”/>
                <positionref ref=”CM_Hatch_Position”/>
        </physvol>
```

```
            <physvol>
                <volumeref ref=”LV_Forward_Heat_Shield”/>
                <positionref ref=”CM_Forward_Position”/>
            </physvol>
        </volume>
    </structure>
    <setup version=”1.0” name=”Default”>
        <world ref=”LV_Universe”/>
    </setup>
</gdml>
```

APPENDIX B

COMMAND MODULE GDML

B.1 GPS Macro File

```
# GPS macro to for particles shotting inward from a sphere.
# spherical surface
/gps/pos/type Surface
/gps/pos/shape Sphere
/gps/pos/centre 0. 0. 0. cm
/gps/pos/radius 20. m
/analysis/Source_Surface_Area 50265482.46
```

B.2 Trapped Proton Energy Spectrum for Solar Maximum Macro File

```
#Source definition
#
# ================================
# SPENVIS particle source
# Project: ISS380KM
# title: ISS at 380km During Solar Maximum 01-104 from TLE
# Particle: trapped proton
# ================================
/gps/particle proton
/gps/ene/type Arb
/gps/hist/type arb
/gps/hist/point 1.000000E-01 9.396800E+02
/gps/hist/point 1.500000E-01 7.326500E+02
/gps/hist/point 2.000000E-01 5.505500E+02
/gps/hist/point 3.000000E-01 3.186300E+02
/gps/hist/point 4.000000E-01 1.917900E+02
/gps/hist/point 5.000000E-01 1.171700E+02
/gps/hist/point 6.000000E-01 7.442500E+01
/gps/hist/point 7.000000E-01 4.795600E+01
/gps/hist/point 1.000000E+00 2.166900E+01
/gps/hist/point 1.500000E+00 6.632000E+00
/gps/hist/point 2.000000E+00 3.237300E+00
/gps/hist/point 3.000000E+00 9.945900E-01
/gps/hist/point 4.000000E+00 5.250800E-01
/gps/hist/point 5.000000E+00 3.205300E-01
/gps/hist/point 6.000000E+00 2.654800E-01
/gps/hist/point 7.000000E+00 2.292400E-01
/gps/hist/point 1.000000E+01 1.437800E-01
/gps/hist/point 1.500000E+01 7.616900E-02
/gps/hist/point 2.000000E+01 6.497900E-02
/gps/hist/point 3.000000E+01 4.994100E-02
```

```
/gps/hist/point 4.000000E+01 4.346700E-02
/gps/hist/point 5.000000E+01 4.401600E-02
/gps/hist/point 6.000000E+01 4.422500E-02
/gps/hist/point 7.000000E+01 4.078600E-02
/gps/hist/point 1.000000E+02 3.591900E-02
/gps/hist/point 1.500000E+02 2.500700E-02
/gps/hist/point 2.000000E+02 1.436600E-02
/gps/hist/point 3.000000E+02 5.401700E-03
/gps/hist/point 4.000000E+02 0.000000E+00
/gps/hist/inter Lin
/gps/hist/type biase
/gps/hist/point 0.0000000000 0.1064E-02
/gps/hist/point 0.2172626814 0.1365E-02
/gps/hist/point 0.3806903622 0.1816E-02
/gps/hist/point 0.5851178649 0.3138E-02
/gps/hist/point 0.7118587594 0.5214E-02
/gps/hist/point 0.7844424747 0.8535E-02
/gps/hist/point 0.8336318682 0.1344E-01
/gps/hist/point 0.8617913150 0.2085E-01
/gps/hist/point 0.9073691906 0.4615E-01
/gps/hist/point 0.9308986194 0.1508E+00
/gps/hist/point 0.9418319053 0.3089E+00
/gps/hist/point 0.9485586822 0.1005E+01
/gps/hist/point 0.9521686412 0.1904E+01
/gps/hist/point 0.9540154519 0.3120E+01
/gps/hist/point 0.9554995519 0.3767E+01
/gps/hist/point 0.9567747555 0.4362E+01
/gps/hist/point 0.9595938180 0.6955E+01
/gps/hist/point 0.9617248734 0.1313E+02
/gps/hist/point 0.9635519377 0.1539E+02
/gps/hist/point 0.9663725592 0.2002E+02
/gps/hist/point 0.9687421307 0.2301E+02
/gps/hist/point 0.9708903343 0.2272E+02
/gps/hist/point 0.9733165468 0.2261E+02
/gps/hist/point 0.9754865754 0.2452E+02
/gps/hist/point 0.9813912773 0.2784E+02
/gps/hist/point 0.9898760059 0.3999E+02
/gps/hist/point 0.9943859864 0.6961E+02
/gps/hist/point 0.9987399700 0.1851E+03
/gps/ang/type cos
/gps/ang/mintheta 0.000E+00 deg
/gps/ang/maxtheta 9.000E+01 deg
/gps/source/list
#
#Normalisation
#
/analysis/NORM_FACTOR_SPECTRUM 1.662843E+07
/analysis/NORM_FACTOR_ANGULAR .25
```

B.3 Run File for Trapped Solar Maximum Macro File

```
# Macro file for Trapped Particles AP8 Solar Maximum
# Load detector file
/mydet/readFile col3iss1_spheres.gdml
/run/initialize
/control/verbose 2
/run/verbose 2
/run/printProgress 10000000
# Load Sphere
```

```
/control/execute gps.mac
# Load Spectrum for Proton Run 0
/control/execute proton.mac
/run/beamOn 1500000000
```

APPENDIX C

APOLLO TRAJECTORY INPUT FILES FOR SPENVIS

C.1 Apollo 11 Trajectory Input File

```
******************************************************************
* Apollo 11 Spacecraft TLI Path from Earth to Moon
* 5 min resolution for 5 hours, then 30 minute for remaining 4 days
*
*
******************************************************************
Title: Apollo 11 Spacecraft TLI Path from Earth to Moon
Planet: Earth
Coordinates: GEI
Columns: DYEA, DMON, DDAY, DHOU, DMIN, DSEC, X, Y, Z
Format: Free
******************************************************************
$$BEGIN
1969 7 16 16 22 31 12498 3696 2461
1969 7 16 16 29 31 8959 9646 6018
1969 7 16 16 34 31 5864 12505 7705
1969 7 16 16 39 31 2895 14576 8915
1969 7 16 16 44 31 160 16157 9832
1969 7 16 16 49 31 -2352 17428 10564
1969 7 16 16 54 31 -4679 18493 11174
1969 7 16 16 59 31 -6852 19413 11698
1969 7 16 17 4 31 -8901 20226 12159
1969 7 16 17 9 31 -10844 20957 12571
1969 7 16 17 14 31 -12700 21622 12945
1969 7 16 17 19 31 -14481 22234 13288
1969 7 16 17 24 31 -16197 22802 13605
1969 7 16 17 29 31 -17855 23332 13901
1969 7 16 17 34 31 -19463 23830 14177
1969 7 16 17 39 31 -21025 24300 14436
1969 7 16 17 44 31 -22547 24744 14682
1969 7 16 17 49 31 -24031 25166 14914
1969 7 16 17 54 31 -25482 25569 15134
1969 7 16 17 59 31 -26901 25953 15344
1969 7 16 18 4 31 -28291 26321 15545
1969 7 16 18 9 31 -29655 26674 15737
1969 7 16 18 14 31 -30994 27013 15921
1969 7 16 18 19 31 -32310 27340 16098
1969 7 16 18 24 31 -33603 27655 16268
1969 7 16 18 29 31 -34877 27959 16431
1969 7 16 18 34 31 -36131 28253 16589
```

```
1969 7 16 18 39 31 -37366 28537 16741
1969 7 16 18 44 31 -38585 28813 16889
1969 7 16 18 49 31 -39787 29080 17031
1969 7 16 18 54 31 -40973 29339 17169
1969 7 16 18 59 31 -42144 29591 17302
1969 7 16 19 4 31 -43301 29836 17432
1969 7 16 19 9 31 -44444 30074 17558
1969 7 16 19 14 31 -45574 30306 17680
1969 7 16 19 19 31 -46692 30532 17798
1969 7 16 19 24 31 -47798 30752 17914
1969 7 16 19 29 31 -48892 30967 18026
1969 7 16 19 34 31 -49974 31176 18135
1969 7 16 19 39 31 -51046 31381 18241
1969 7 16 19 44 31 -52108 31581 18345
1969 7 16 19 49 31 -53160 31776 18446
1969 7 16 19 54 31 -54202 31967 18545
1969 7 16 19 59 31 -55234 32154 18641
1969 7 16 20 4 31 -56257 32337 18735
1969 7 16 20 9 31 -57272 32516 18827
1969 7 16 20 14 31 -58278 32691 18916
1969 7 16 20 19 31 -59276 32862 19004
1969 7 16 20 24 31 -60265 33031 19089
1969 7 16 20 29 31 -61247 33195 19173
1969 7 16 20 34 31 -62222 33357 19255
1969 7 16 20 39 31 -63188 33515 19335
1969 7 16 20 44 31 -64148 33671 19413
1969 7 16 20 49 31 -65100 33823 19490
1969 7 16 20 54 31 -66046 33973 19565
1969 7 16 20 59 31 -66985 34120 19638
1969 7 16 21 4 31 -67917 34265 19710
1969 7 16 21 9 31 -68844 34406 19781
1969 7 16 21 14 31 -69763 34546 19850
1969 7 16 21 44 31 -75159 35333 20237
1969 7 16 22 14 31 -80363 36046 20583
1969 7 16 22 44 31 -85395 36696 20893
1969 7 16 23 14 31 -90275 37291 21172
1969 7 16 23 44 31 -95015 37837 21423
1969 7 17 0 14 31 -99629 38341 21651
1969 7 17 0 44 31 -104127 38806 21857
1969 7 17 1 14 31 -108518 39236 22044
1969 7 17 1 44 31 -112809 39636 22214
1969 7 17 2 14 31 -117008 40007 22368
1969 7 17 2 44 31 -121121 40352 22507
1969 7 17 3 14 31 -125152 40673 22634
1969 7 17 3 44 31 -129107 40972 22748
1969 7 17 4 14 31 -132990 41251 22852
1969 7 17 4 44 31 -136804 41511 22944
1969 7 17 5 14 31 -140554 41754 23028
1969 7 17 5 44 31 -144242 41980 23102
1969 7 17 6 14 31 -147872 42191 23168
1969 7 17 6 44 31 -151446 42387 23226
1969 7 17 7 14 31 -154966 42570 23277
1969 7 17 7 44 31 -158435 42740 23321
1969 7 17 8 14 31 -161854 42898 23359
1969 7 17 8 44 31 -165227 43045 23390
1969 7 17 9 14 31 -168553 43181 23416
1969 7 17 9 44 31 -171837 43306 23436
1969 7 17 10 14 31 -175078 43422 23451
1969 7 17 10 44 31 -178278 43529 23460
```

```
1969 7 17 11 14 31 -181439 43627 23466
1969 7 17 11 44 31 -184562 43716 23467
1969 7 17 12 14 31 -187648 43798 23463
1969 7 17 12 44 31 -190698 43872 23455
1969 7 17 13 14 31 -193714 43938 23444
1969 7 17 13 44 31 -196696 43998 23429
1969 7 17 14 14 31 -199645 44050 23410
1969 7 17 14 44 31 -202563 44097 23388
1969 7 17 15 14 31 -205450 44137 23363
1969 7 17 15 44 31 -208307 44171 23334
1969 7 17 16 14 31 -211134 44199 23303
1969 7 17 16 44 31 -213933 44222 23269
1969 7 17 17 14 31 -216705 44239 23231
1969 7 17 17 44 31 -219449 44252 23192
1969 7 17 18 14 31 -222166 44259 23149
1969 7 17 18 44 31 -224858 44261 23104
1969 7 17 19 14 31 -227525 44259 23057
1969 7 17 19 44 31 -230167 44253 23008
1969 7 17 20 14 31 -232785 44242 22956
1969 7 17 20 44 31 -235379 44227 22902
1969 7 17 21 14 31 -237950 44207 22846
1969 7 17 21 44 31 -240498 44184 22788
1969 7 17 22 14 31 -243024 44157 22728
1969 7 17 22 44 31 -245528 44127 22666
1969 7 17 23 14 31 -248011 44093 22603
1969 7 17 23 44 31 -250473 44055 22537
1969 7 18 0 14 31 -252915 44014 22470
1969 7 18 0 44 31 -255336 43970 22401
1969 7 18 1 14 31 -257738 43922 22331
1969 7 18 1 44 31 -260120 43871 22259
1969 7 18 2 14 31 -262483 43818 22185
1969 7 18 2 44 31 -264828 43761 22111
1969 7 18 3 14 31 -267154 43701 22034
1969 7 18 3 44 31 -269462 43639 21956
1969 7 18 4 14 31 -271752 43574 21877
1969 7 18 4 44 31 -274024 43507 21797
1969 7 18 5 14 31 -276280 43436 21715
1969 7 18 5 44 31 -278518 43364 21632
1969 7 18 6 14 31 -280740 43288 21548
1969 7 18 6 44 31 -282945 43211 21463
1969 7 18 7 14 31 -285134 43131 21376
1969 7 18 7 44 31 -287307 43049 21289
1969 7 18 8 14 31 -289464 42964 21200
1969 7 18 8 44 31 -291606 42878 21110
1969 7 18 9 14 31 -293732 42789 21020
1969 7 18 9 44 31 -295843 42698 20928
1969 7 18 10 14 31 -297940 42606 20835
1969 7 18 10 44 31 -300022 42511 20742
1969 7 18 11 14 31 -302089 42414 20647
1969 7 18 11 44 31 -304142 42315 20551
1969 7 18 12 14 31 -306181 42215 20455
1969 7 18 12 44 31 -308207 42113 20358
1969 7 18 13 14 31 -310218 42009 20260
1969 7 18 13 44 31 -312216 41903 20161
1969 7 18 14 14 31 -314200 41795 20061
1969 7 18 14 44 31 -316172 41686 19960
1969 7 18 15 14 31 -318130 41575 19859
1969 7 18 15 44 31 -320075 41463 19757
1969 7 18 16 14 31 -322008 41349 19654
```

```
1969 7 18 16 44 31 -323928 41233 19551
1969 7 18 17 14 31 -325835 41116 19446
1969 7 18 17 44 31 -327731 40998 19341
1969 7 18 18 14 31 -329614 40878 19236
1969 7 18 18 44 31 -331485 40757 19130
1969 7 18 19 14 31 -333344 40634 19023
1969 7 18 19 44 31 -335191 40510 18915
1969 7 18 20 14 31 -337027 40385 18807
1969 7 18 20 44 31 -338851 40258 18698
1969 7 18 21 14 31 -340664 40130 18589
1969 7 18 21 44 31 -342465 40000 18479
1969 7 18 22 14 31 -344255 39870 18369
1969 7 18 22 44 31 -346035 39738 18258
1969 7 18 23 14 31 -347803 39605 18146
1969 7 18 23 44 31 -349560 39471 18034
1969 7 19 0 14 31 -351307 39336 17922
1969 7 19 0 44 31 -353043 39200 17809
1969 7 19 1 14 31 -354769 39062 17695
1969 7 19 1 44 31 -356484 38923 17581
1969 7 19 2 14 31 -358189 38784 17466
1969 7 19 2 44 31 -359883 38643 17351
1969 7 19 3 14 31 -361568 38501 17236
1969 7 19 3 44 31 -363242 38359 17120
1969 7 19 4 14 31 -364907 38215 17004
1969 7 19 4 44 31 -366561 38070 16887
1969 7 19 5 14 31 -368206 37924 16770
1969 7 19 5 44 31 -369841 37778 16652
1969 7 19 6 14 31 -371467 37630 16534
1969 7 19 6 44 31 -373083 37482 16415
1969 7 19 7 14 31 -374690 37332 16297
1969 7 19 7 44 31 -376287 37182 16177
1969 7 19 8 14 31 -377875 37031 16058
1969 7 19 8 44 31 -379454 36879 15938
1969 7 19 9 14 31 -381023 36726 15818
1969 7 19 9 44 31 -382584 36572 15697
1969 7 19 10 14 31 -384135 36417 15576
1969 7 19 10 44 31 -385678 36262 15455
1969 7 19 11 14 31 -387212 36106 15333
1969 7 19 11 44 31 -388737 35949 15211
1969 7 19 12 14 31 -390253 35791 15089
1969 7 19 12 44 31 -391761 35633 14966
1969 7 19 13 14 31 -393260 35474 14843
1969 7 19 13 44 31 -394750 35314 14720
1969 7 19 14 14 31 -396232 35153 14597
1969 7 19 14 44 31 -397706 34992 14473
1969 7 19 15 14 31 -399172 34830 14349
1969 7 19 15 44 31 -400629 34667 14224
1969 7 19 16 14 31 -402078 34504 14100
1969 7 19 16 59 31 -404236 34257 13912
1969 7 19 17 21 50 -405299 34135 13819
$$END
```

C.2 Apollo 14 Trajectory Input File

```
****************************************************************
* Apollo 14 Spacecraft TLI Path from Earth to Moon
* 5 min resolution for 5 hours, then 30 minute for remaining 4 days
*
*
```

```
*****************************************************************
Title: Apollo 14 Spacecraft TLI Path from Earth to Moon
Planet: Earth
Coordinates: GEI
Columns: DYEA, DMON, DDAY, DHOU, DMIN, DSEC, X, Y, Z
Format: Free
*****************************************************************
$$BEGIN
1971 1 31 23 34 49 -3750.740748 -11320.23215 -5532.207944
1971 1 31 23 39 49 1693.717431 -12983.64188 -3350.246646
1971 1 31 23 44 49 6513.664028 -12908.16606 -917.9730138
1971 1 31 23 49 49 10328.9162 -11908.63737 1312.007569
1971 1 31 23 54 49 13332.51199 -10573.11285 3245.930709
1971 1 31 23 59 49 15778.69093 -9157.418653 4927.806221
1971 2 1 0 4 49 17846.82816 -7753.389489 6417.326087
1971 2 1 0 9 49 19650.05359 -6389.855249 7761.544565
1971 2 1 0 14 49 21259.71115 -5073.104667 8993.987803
1971 2 1 0 19 49 22722.25106 -3801.718047 10138.27328
1971 2 1 0 24 49 24069.12059 -2571.943276 11211.29791
1971 2 1 0 29 49 25322.43269 -1379.630598 12225.43577
1971 2 1 0 34 49 26498.27729 -220.8955051 13189.97314
1971 2 1 0 39 49 27608.71752 907.6934533 14112.04217
1971 2 1 0 44 49 28663.03497 2009.101269 14997.23705
1971 2 1 0 49 49 29668.53273 3085.871838 15850.02884
1971 2 1 0 54 49 30631.06946 4140.187656 16674.05096
1971 2 1 0 59 49 31555.42472 5173.927494 17472.30006
1971 2 1 1 4 49 32445.55526 6188.716809 18247.28005
1971 2 1 1 9 49 33304.77903 7185.970003 19001.10761
1971 2 1 1 14 49 34135.90994 8166.925185 19735.59062
1971 2 1 1 19 49 34941.35852 9132.672577 20452.28762
1971 2 1 1 24 49 35723.20824 10084.17767 21152.55337
1971 2 1 1 29 49 36483.27434 11022.30017 21837.57435
1971 2 1 1 34 49 37223.14978 11947.8095 22508.39673
1971 2 1 1 39 49 37944.24156 12861.39766 23165.94864
1971 2 1 1 44 49 38647.79975 13763.68975 23811.05812
1971 2 1 1 49 49 39334.94102 14655.2529 24444.46773
1971 2 1 1 54 49 40006.66772 15536.60362 25066.84646
1971 2 1 1 59 49 40663.88368 16408.21406 25678.7997
1971 2 1 2 4 49 41307.40727 17270.51731 26280.8774
1971 2 1 2 9 49 41937.98233 18123.91189 26873.58106
1971 2 1 2 14 49 42556.28733 18968.76561 27457.36953
1971 2 1 2 19 49 43162.94317 19805.4189 28032.66398
1971 2 1 2 24 49 43758.51981 20634.18767 28599.85215
1971 2 1 2 29 49 44343.54195 21455.3658 29159.29201
1971 2 1 2 34 49 44918.49391 22269.22729 29711.31486
1971 2 1 2 39 49 45483.82385 23076.02821 30256.22812
1971 2 1 2 44 49 46039.94746 23876.00833 30794.31766
1971 2 1 2 49 49 46587.25116 24669.39258 31325.84989
1971 2 1 2 54 49 47126.09493 25456.39239 31851.07362
1971 2 1 2 59 49 47656.81474 26237.20683 32370.22165
1971 2 1 3 4 49 48179.72478 27012.02363 32883.51218
1971 2 1 3 9 49 48695.11937 27781.02013 33391.1501
1971 2 1 3 14 49 49203.27465 28544.36406 33893.32809
1971 2 1 3 19 49 49704.45019 29302.21432 34390.22768
1971 2 1 3 24 49 50198.89029 30054.72164 34882.02007
1971 2 1 3 29 49 50686.82521 30802.02914 35368.86703
1971 2 1 3 34 49 51168.47231 31544.27296 35850.92155
1971 2 1 3 39 49 51644.03703 32281.58267 36328.32855
1971 2 1 3 44 49 52113.71378 33014.08178 36801.22544
```

```
1971 2 1 3 49 49 52577.68674 33741.88809 37269.7427
1971 2 1 3 54 49 53036.13062 34465.11414 37734.00431
1971 2 1 3 59 49 53489.21132 35183.8675 38194.12826
1971 2 1 4 4 49 53937.08655 35898.25109 38650.22693
1971 2 1 4 9 49 54379.90638 36608.36347 39102.40745
1971 2 1 4 14 49 54817.81373 37314.29913 39550.77204
1971 2 1 4 19 49 55250.94486 38016.14869 39995.41837
1971 2 1 4 24 49 55679.4298 38713.99918 40436.43978
1971 2 1 4 29 49 56103.39274 39407.93418 40873.92559
1971 2 1 4 34 49 56522.95235 40098.03409 41307.96133
1971 2 1 5 4 49 58953.87537 44162.23447 43844.08949
1971 2 1 5 34 49 61251.20447 48105.64761 46274.10474
1971 2 1 6 4 49 63431.75544 51940.30032 48610.33212
1971 2 1 6 34 49 65509.05481 55676.14964 50862.77788
1971 2 1 7 4 49 67494.17645 59321.56607 53039.70511
1971 2 1 7 34 49 69396.32287 62883.67824 55148.03667
1971 2 1 8 4 49 71223.24054 66368.62513 57193.64499
1971 2 1 8 34 49 72981.52367 69781.74487 59181.56552
1971 2 1 9 4 49 74676.84108 73127.71871 61116.15699
1971 2 1 9 34 49 76314.10863 76410.68279 63001.22412
1971 2 1 10 4 49 77897.62245 79634.31606 64840.11282
1971 2 1 10 34 49 79431.16324 82801.91053 66635.78524
1971 2 1 11 4 49 80918.07911 85916.42782 68390.87964
1971 2 1 11 34 49 82361.35197 88980.54549 70107.75866
1971 2 1 12 4 49 83763.65138 91996.69502 71788.54861
1971 2 1 12 34 49 85127.37867 94967.09348 73435.17186
1971 2 1 13 4 49 86454.70328 97893.77 75049.37362
1971 2 1 13 34 49 87747.59305 100778.5881 76632.74441
1971 2 1 14 4 49 89007.83959 103623.2648 78186.73885
1971 2 1 14 34 49 90237.0797 106429.3866 79712.69172
1971 2 1 15 4 49 91436.81349 109198.4235 81211.83154
1971 2 1 15 34 49 92608.41995 111931.7413 82685.29224
1971 2 1 16 4 49 93753.17024 114630.6117 84134.12327
1971 2 1 16 34 49 94872.23917 117296.2215 85559.2983
1971 2 1 17 4 49 95966.71521 119929.6808 86961.72276
1971 2 1 17 34 49 97037.6091 122532.0297 88342.24054
1971 2 1 18 4 49 98085.86148 125104.245 89701.63974
1971 2 1 18 34 49 99112.34953 127647.2452 91040.65784
1971 2 1 19 4 49 100117.8928 130161.8956 92359.98618
1971 2 1 19 34 49 101103.2586 132649.0126 93660.27402
1971 2 1 20 4 49 102069.1661 135109.3678 94942.13207
1971 2 1 20 34 49 103016.2911 137543.6914 96206.13571
1971 2 1 21 4 49 103945.2691 139952.6751 97452.82782
1971 2 1 21 34 49 104856.6988 142336.9756 98682.72134
1971 2 1 22 4 49 105751.1453 144697.2162 99896.30162
1971 2 1 22 34 49 106629.1421 147033.9902 101094.0284
1971 2 1 23 4 49 107491.194 149347.8622 102276.3378
1971 2 1 23 34 49 108337.7792 151639.3705 103443.6441
1971 2 2 0 4 49 109169.3511 153909.0285 104596.3408
1971 2 2 0 34 49 109986.3399 156157.3268 105734.8028
1971 2 2 1 4 49 110789.1547 158384.7341 106859.387
1971 2 2 1 34 49 111578.1847 160591.6991 107970.434
1971 2 2 2 4 49 112353.8002 162778.6513 109068.2687
1971 2 2 2 34 49 113116.3544 164946.0024 110153.2016
1971 2 2 3 4 49 113866.1844 167094.1474 111225.5297
1971 2 2 3 34 49 114603.6119 169223.4653 112285.537
1971 2 2 4 4 49 115328.9443 171334.3203 113333.4959
1971 2 2 4 34 49 116042.4759 173427.0624 114369.6673
1971 2 2 5 4 49 116744.4882 175502.0284 115394.3014
```

```
1971 2 2 5 34 49 117435.251 177559.5424 116407.6386
1971 2 2 6 4 49 118115.0228 179599.9166 117409.9098
1971 2 2 6 34 49 118784.052 181623.4521 118401.3369
1971 2 2 7 4 49 119442.5766 183630.4389 119382.1333
1971 2 2 7 34 49 120090.8255 185621.1572 120352.5047
1971 2 2 8 4 49 120729.0189 187595.8773 121312.6489
1971 2 2 8 34 49 121357.3683 189554.8604 122262.7568
1971 2 2 9 4 49 121976.0775 191498.3589 123203.0123
1971 2 2 9 34 49 122585.3427 193426.617 124133.5928
1971 2 2 10 4 49 123185.3529 195339.8708 125054.6699
1971 2 2 10 34 49 123776.2906 197238.3489 125966.4088
1971 2 2 11 4 49 124358.3316 199122.2727 126868.9696
1971 2 2 11 34 49 124931.6456 200991.8566 127762.507
1971 2 2 12 4 49 125496.3966 202847.3085 128647.1704
1971 2 2 12 34 49 126052.7431 204688.8301 129523.1046
1971 2 2 13 4 49 126600.838 206516.6167 130390.4498
1971 2 2 13 34 49 127140.8296 208330.8582 131249.3417
1971 2 2 14 4 49 127672.861 210131.7388 132099.9118
1971 2 2 14 34 49 128197.071 211919.4373 132942.2877
1971 2 2 15 4 49 128713.5939 213694.1277 133776.593
1971 2 2 15 34 49 129222.5597 215455.9788 134602.9478
1971 2 2 16 4 49 129724.0946 217205.1548 135421.4684
1971 2 2 16 34 49 130218.3208 218941.8155 136232.268
1971 2 2 17 4 49 130705.357 220666.1164 137035.4564
1971 2 2 17 34 49 131185.3181 222378.2085 137831.1402
1971 2 2 18 4 49 131658.3159 224078.2392 138619.4232
1971 2 2 18 34 49 132124.4589 225766.3519 139400.4063
1971 2 2 19 4 49 132583.8523 227442.6862 140174.1875
1971 2 2 19 34 49 133036.5985 229107.3781 140940.8622
1971 2 2 20 4 49 133482.7971 230760.5603 141700.5234
1971 2 2 20 34 49 133922.5447 232402.3622 142453.2614
1971 2 2 21 4 49 134355.9355 234032.9097 143199.1643
1971 2 2 21 34 49 134783.061 235652.326 143938.3178
1971 2 2 22 4 49 135204.0104 237260.731 144670.8056
1971 2 2 22 34 49 135618.8704 238858.2418 145396.7091
1971 2 2 23 4 49 136027.7253 240444.9729 146116.1076
1971 2 2 23 34 49 136430.6577 242021.0358 146829.0787
1971 2 3 0 4 49 136827.7475 243586.5396 147535.6979
1971 2 3 0 34 49 137219.073 245141.5907 148236.0388
1971 2 3 1 4 49 137604.7102 246686.2934 148930.1735
1971 2 3 1 34 49 137984.7336 248220.7492 149618.1721
1971 2 3 2 4 49 138359.2156 249745.0576 150300.1031
1971 2 3 2 34 49 138728.2268 251259.3159 150976.0336
1971 2 3 3 4 49 139091.8362 252763.6191 151646.0288
1971 2 3 3 34 49 139450.1112 254258.0601 152310.1529
1971 2 3 4 4 49 139803.1176 255742.7301 152968.468
1971 2 3 4 34 49 140150.9194 257217.7179 153621.0354
1971 2 3 5 4 49 140493.5795 258683.1107 154267.9147
1971 2 3 5 34 49 140831.1591 260138.9938 154909.1643
1971 2 3 6 4 49 141163.718 261585.4507 155544.8411
1971 2 3 6 34 49 141491.3149 263022.5632 156175.0012
1971 2 3 7 4 49 141814.0069 264450.4113 156799.6991
1971 2 3 7 34 49 142131.8499 265869.0735 157418.9883
1971 2 3 8 4 49 142444.8987 267278.6266 158032.9211
1971 2 3 8 34 49 142753.2068 268679.1459 158641.5488
1971 2 3 9 4 49 143056.8265 270070.7052 159244.9216
1971 2 3 9 34 49 143355.8092 271453.377 159843.0885
1971 2 3 10 4 49 143650.2049 272827.232 160436.0978
1971 2 3 10 34 49 143940.0628 274192.3398 161023.9966
```

```
1971 2 3 11 4 49 144225.431 275548.7687 161606.8311
1971 2 3 11 34 49 144506.3565 276896.5854 162184.6466
1971 2 3 12 4 49 144782.8854 278235.8557 162757.4874
1971 2 3 12 34 49 145055.063 279566.6438 163325.3971
1971 2 3 13 4 49 145322.9335 280889.0129 163888.4183
1971 2 3 13 34 49 145586.5402 282203.025 164446.593
1971 2 3 14 4 49 145845.9258 283508.7408 164999.962
1971 2 3 14 34 49 146101.1318 284806.2202 165548.5656
1971 2 3 15 4 49 146352.1992 286095.5216 166092.4435
1971 2 3 15 34 49 146599.1679 287376.7027 166631.6341
1971 2 3 16 4 49 146842.0774 288649.8199 167166.1757
1971 2 3 16 34 49 147080.9662 289914.9287 167696.1055
1971 2 3 17 4 49 147315.872 291172.0836 168221.4601
1971 2 3 17 34 49 147546.832 292421.3382 168742.2754
1971 2 3 18 4 49 147773.8826 293662.7449 169258.5869
1971 2 3 18 34 49 147997.0595 294896.3556 169770.4291
1971 2 3 19 4 49 148216.3978 296122.2209 170277.836
1971 2 3 19 34 49 148431.932 297340.3907 170780.8412
1971 2 3 20 4 49 148643.6957 298550.9141 171279.4774
1971 2 3 20 34 49 148851.7224 299753.8393 171773.777
1971 2 3 21 4 49 149056.0445 300949.2136 172263.7716
1971 2 3 21 34 49 149256.694 302137.0835 172749.4923
1971 2 3 22 4 49 149453.7025 303317.4949 173230.9698
1971 2 3 22 34 49 149647.1009 304490.4929 173708.2342
1971 2 3 23 4 49 149836.9195 305656.1215 174181.3151
1971 2 3 23 34 49 150023.1881 306814.4245 174650.2414
1971 2 4 0 4 49 150205.9361 307965.4445 175115.0419
1971 2 4 0 34 49 150385.1923 309109.2238 175575.7445
1971 2 4 1 4 49 150560.9851 310245.8038 176032.3771
1971 2 4 1 34 49 150733.3423 311375.2251 176484.9666
1971 2 4 2 4 49 150902.2914 312497.528 176933.5399
1971 2 4 2 34 49 151067.8591 313612.7518 177378.1232
1971 2 4 3 4 49 151230.0722 314720.9354 177818.7425
1971 2 4 3 34 49 151388.9566 315822.117 178255.4232
1971 2 4 4 4 49 151544.5379 316916.3342 178688.1902
1971 2 4 4 34 49 151696.8413 318003.624 179117.0683
1971 2 4 5 4 49 151845.8918 319084.0228 179542.0817
1971 2 4 5 34 49 151991.7136 320157.5665 179963.2542
1971 2 4 6 4 49 152134.3309 321224.2903 180380.6094
1971 2 4 6 34 49 152273.7672 322284.229 180794.1703
1971 2 4 6 34 49 152273.7672 322284.229 180794.1703
1971 2 4 6 39 49 152296.699 322460.2282 180862.7299
1971 2 4 6 44 49 152319.5431 322636.04 180931.1848
1971 2 4 6 49 49 152342.2998 322811.6647 180999.5351
1971 2 4 6 54 49 152364.9691 322987.1022 181067.781
1971 2 4 6 59 42 152387.0101 323158.1491 181134.2883
$$END
```

REFERENCES

[1] R. A. Scheuring, J. A. Jones, J. D. Novak, J. D. Polk, D. B. Gillis, J. Schmid *et al.*, "The apollo medical operations project: Recommendations to improve crew health and performance for future exploration missions and lunar surface operations," *Acta Astronautica*, vol. 63, no. 7-10, pp. 980–987, 2008.

[2] T. Ersmark, "Geant4 monte carlo simulations of the international space station radiation environment," Ph.D. dissertation, KTH, Physics, 2006, qC 20110125.

[3] J. W. Wilson, S. Y. Chun, F. F. Badavi, L. W. Townsend, and S. L. Lamkin, *HZETRN: A heavy ion/nucleon transport code for space radiations*, ser. NASA technical paper ;3146. Washington, D.C.: National Aeronautics and Space Administration, Office of Management, Scientific and Technical Information Program, 1991.

[4] R. C. Singleterry, S. R. Blattnig, M. S. Clowdsley, G. D. Qualls, C. A. Sandridge, L. C. Simonsen *et al.*, "Oltaris: On-line tool for the assessment of radiation in space," NASA Langley Research Center, Report NASA/TP-2010-216722, Jul 01, 2010 2010.

[5] F. Lei, P. R. Truscott, C. S. Dyer, B. Quaghebeur, D. Heynderickx, P. Nieminen, H. Evans, and E. Daly, "Mulassis: a geant4-based multilayered shielding simulation tool," *IEEE Transactions on Nuclear Science*, vol. 49, no. 6, pp. 2788–2793, 2002.

[6] G. Santina, V. Ivanchenko, H. Evans, P. Nieminen, and E. Daly, "Gras: a general-purpose 3-d modular simulation tool for space environment effects analysis," *IEEE Transactions on Nuclear Science*, vol. 52, no. 6, pp. 2294–2299, 2005.

[7] J. E. Sweezy, T. Booth, F. Brown *et al.*, "Mcnp–a general monte carlo n-particle transport code, version 5," *MCNP user manual, Report LA–UR–03–1987, Los Alamos, CA: Los Alamos National Laboratory*, 2003.

[8] E. R. Benton and E. V. Benton, "Space radiation dosimetry in low-earth orbit and beyond," *Nuclear Instruments and Methods in Physics Research Section B: Beam Interactions with Materials and Atoms*, vol. 184, no. 1-2, pp. 255–294, 2001.

[9] R. A. English and M. S. Center, "Apollo experience report: Protection against radiation," 1973.

[10] "Second symposium on protection against radiations in space, gatlinburg, tennessee, october 12-14, 1964," A. Reetz, Ed. National Aeronautics and Space Administration, 1964, Conference Proceedings.

[11] Space Radiation Analysis Group, "Space radiation analysis group - nasa, jsc," 2014. [Online]. Available: http://srag.jsc.nasa.gov/

[12] Belgian Institute for Space Aeronomy, "Spenvis user manual," 2010. [Online]. Available: https://www.spenvis.oma.be/help/

[13] P. Kristóf, "Solar cycle prediction," *Living Reviews in Solar Physics*, vol. 7, no. 6, 2010.

[14] R. Turner, *What We Must Know about Solar Particle Events to Reduce the Risk to Astronauts*. American Geophysical Union, 2013, pp. 39–44.

[15] J. W. Wilson, F. A. Cucinotta, J. L. Shinn, L. C. Simonsen, R. R. Dubey, W. R. Jordan *et al.*, "Shielding from solar particle event exposures in deep space," *Radiation Measurements*, vol. 30, no. 3, pp. 361–382, 1999.

[16] L. B. Peter, "Galactic cosmic rays," *Journal of Physics: Conference Series*, vol. 47, no. 1, p. 78, 2006.

[17] A. J. Tylka, J. H. Adams, P. R. Boberg, B. Brownstein, W. F. Dietrich, E. O. Flueckiger *et al.*, "Creme96: A revision of the cosmic ray effects on micro-electronics code," *Nuclear Science, IEEE Transactions on*, vol. 44, no. 6, pp. 2150–2160, 1997.

[18] G. D. Badhwar, "The radiation environment in low-earth orbit," *Radiation Research*, vol. 148, no. 5, pp. S3–S10, 1997. [Online]. Available: http://www.jstor.org/stable/3579710

[19] J. H. Adams, A. F. Barghouty, M. H. Mendenhall, R. A. Reed, B. D. Sierawski, K. M. Warren *et al.*, "Crème: The 2011 revision of the cosmic ray effects on micro-electronics code," *IEEE Transactions on Nuclear Science*, vol. 59, no. 6, pp. 3141–3147, 2012.

[20] G. Falzetta, F. Longo, and A. Zanini, "Geant4 and creme96 comparison using only proton fluxes," 2008.

[21] ISO, "Space environment (natural and artificial) — galactic cosmic ray model," International Organization for Standardization, Geneva, Switzerland, ISO Standard, 2004.

[22] M. Walt, *Introduction to Geomagnetically Trapped Radiation*. Cambridge, UK: Cambridge University Press, 1994.

[23] N. Y. Ganushkina, I. Dandouras, Y. Y. Shprits, and J. Cao, "Locations of boundaries of outer and inner radiation belts as observed by cluster and double star," *Journal of Geophysical Research: Space Physics*, vol. 116, no. A9, p. A09234, 2011.

[24] R. B. Horne, "Plasma astrophysics: Acceleration of killer electrons," *Nat Phys*, vol. 3, no. 9, pp. 590–591, 2007, 10.1038/nphys703.

[25] European Space Agency, "Space environment information system," 2015. [Online]. Available: https://www.spenvis.oma.be

[26] I. Getselev, S. Rumin, N. Sobolevsky, M. Ufimtsev, and M. Podzolko, "Absorbed dose of secondary neutrons from galactic cosmic rays inside the international space station," *Advances in Space Research*, vol. 34, no. 6, pp. 1429–1432, 2004.

[27] D. Heynderickx, J. Lemaire, E. J. Daly, and H. D. R. Evans, "Calculating low-altitude trapped particle fluxes with the nasa models ap-8 and ae-8," *Radiation Measurements*, vol. 26, no. 6, pp. 947–952, 1996.

[28] D. Bilitza, "Radbelt (1988)," *Planetary and Space Science*, vol. 40, pp. 568–568, 1992.

[29] G. P. Ginet, T. P. O'Brien, S. L. Huston, W. R. Johnston, T. B. Guild, R. Friedel *et al.*, "Ae9, ap9 and spm: New models for specifying the trapped energetic particle and space plasma environment," *Space Science Reviews*, vol. 179, no. 1-4, pp. 579–615, 2013.

[30] C. E. Jordan, “Nasa radiation belt models ap-8 and ae-8,” DTIC Document, Report, 1989.

[31] D. Heynderickx, B. Quaghebeur, J. Wera, E. J. Daly, and H. D. R. Evans, “New radiation environment and effects models in the european space agency’s space environment information system (spenvis),” *Space Weather*, vol. 2, no. 10, p. S10S03, 2004.

[32] F. A. Cucinotta and M. Durante, “Risk of radiation carcinogenesis,” *Human health and performance risks of space exploration missions. NASA SP-2009-3405. Houston: National Aeronautics and Space Administration*, pp. 119–170, 2009.

[33] H. Wu, J. Huff, R. Casey, M.-H. Kim, and F. A. Cucinotta, “Risk of acute radiation syndromes due to solar particle events,” *H NASA, HHC*, 2008. [Online]. Available: http://humanresearchroadmap.nasa.gov/Risks/risk.aspx?i=97

[34] F. A. Cucinotta, H. Wang, and J. L. Huff, “Risk of acute or late central nervous system effects from radiation exposure,” *NASA Human Research Program Roadmap*, 2012.

[35] J. Huff and F. A. Cucinotta, “Risk of degenerative tissue or other health effects from radiation exposure,” *Human Health and performance risks of space exploration missions National Aeronautics and Space Administration, NASA SP-2009-3405, Houston, TX*, pp. 213–35, 2009.

[36] J. K. Shultis and R. E. Faw, *Radiation shielding*. American Nuclear Society, 2000.

[37] J. W. Wilson, J. L. Shinn, R. K. Tripathi, R. C. Singleterry, M. S. Clowdsley, S. A. Thibeault *et al.*, “Issues in deep space radiation protection,” *Acta Astronautica*, vol. 49, no. 3–10, pp. 289–312, 2001.

[38] D. Rapp, “Radiation effects and shielding requirements in human missions to the moon and mars,” *The Mars Journal*, pp. 46–71, 2006.

[39] G. Reitz, R. Facius, and H. Sandler, “Radiation protection in space,” *Acta Astronautica*, vol. 35, no. 4-5, pp. 313–338, 1995.

[40] E. S. Gilbert, “Ionizing radiation and cancer risks: What have we learned from epidemiology?” *International journal of radiation biology*, vol. 85, no. 6, pp. 467–482, 2009, 19401906[pmid] Int J Radiat Biol.

[41] ICRP, “The 2007 recommendations of the interenational commission on radiological protection,” Report 0146-6453, 2007.

[42] ——, “1990 recommendations of the icrp,” Report ICRP Publication 60, 1990.

[43] L. W. Townsend and R. J. M. Fry, “Radiation protection guidance for activities in low-earth orbit,” *Advances in Space Research*, vol. 30, no. 4, pp. 957–963, 2002.

[44] M. A. Christgen, “International space station medical operations requirements documents (iss mord),” 2003.

[45] T. Gabriel, “High energy transport code, hetc,” Oak Ridge National Lab., TN (USA), Report, 1985.

[46] Y. M. Charara, L. W. Townsend, T. A. Gabriel, C. J. Zeitlin, L. H. Heilbronn, and J. Miller, “Hetc-heds code validation using laboratory beam energy loss spectra data,” *Nuclear Science, IEEE Transactions on*, vol. 55, no. 6, pp. 3164–3168, 2008.

[47] G. Battistoni, F. Cerutti, A. Fasso, A. Ferrari, S. Muraro, J. Ranft *et al.*, "The fluka code: Description and benchmarking," in *Hadronic Shower Simulation Workshop(AIP Conference Proceedings Volume 896)*, vol. 896, Conference Proceedings, pp. 31–49.

[48] K. Niita, T. Sato, H. Iwase, H. Nose, H. Nakashima, and L. Sihver, "Phits—a particle and heavy ion transport code system," *Radiation Measurements*, vol. 41, no. 9–10, pp. 1080–1090, 2006.

[49] S. Agostinelli, J. Allison, K. Amako, J. Apostolakis, H. Araujo, P. Arce *et al.*, "Geant4—a simulation toolkit," *Nuclear Instruments and Methods in Physics Research Section A: Accelerators, Spectrometers, Detectors and Associated Equipment*, vol. 506, no. 3, pp. 250–303, 2003.

[50] J. W. Wilson, L. W. Townsend, J. E. Nealy, S. Y. Chun, B. Hong, W. W. Buck *et al.*, "Bryntrn: a baryon transport model," 1989.

[51] G. Rudstam, "Systematics of spallation yields," CERN, Geneva, Report, 1966.

[52] D. Greiner, P. Lindstrom, H. Heckman, B. Cork, and F. Bieser, "Momentum distributions of isotopes produced by fragmentation of relativistic c 12 and o 16 projectiles," *Physical Review Letters*, vol. 35, no. 3, p. 152, 1975.

[53] J. H. Heinbockel, T. C. Slaba, R. K. Tripathi, S. R. Blattnig, J. W. Norbury, F. F. Badavi *et al.*, "Comparison of the transport codes hzetrn, hetc and fluka for galactic cosmic rays," *Advances in Space Research*, vol. 47, no. 6, pp. 1089–1105, 2011.

[54] T. C. Slaba, S. R. Blattnig, and F. F. Badavi, "Faster and more accurate transport procedures for hzetrn," 2010.

[55] T. C. Slaba, S. R. Blattnig, S. K. Aghara, L. W. Townsend, T. Handler, T. A. Gabriel, L. S. Pinsky, and B. Reddell, "Coupled neutron transport for hzetrn," *Radiation Measurements*, vol. 45, no. 2, pp. 173–182, 2010.

[56] N. Metropolis, "The beginning of the monte carlo method," *Los Alamos Science*, vol. 15, no. 584, pp. 125–130, 1987.

[57] B. Kiedrowski, "A millenial's perspective on the future of monte carlo radiation transport," in *M&C 2013*. Los Alamos National Lab, Conference Proceedings.

[58] J. K. Shultis and R. E. Faw, *An MCNP Primer*. Manhattan, KS: Dept. of Mechanical and Nuclear Engineering, 2006.

[59] H. Tsige-Tamirat, U. Fischer, A. Serikov, and S. Stickel, "Use of mccad for the conversion of iter cad data to mcnp geometry," *Fusion Engineering and Design*, vol. 83, no. 10-12, pp. 1771–1773, 2008.

[60] L. W. Townsend, T. M. Miller, and T. A. Gabriel, "Hetc radiation transport code development for cosmic ray shielding applications in space," *Radiation Protection Dosimetry*, vol. 116, no. 1-4, pp. 135–139, 2005.

[61] A. Ferrari, P. R. Sala, A. Fasso, and J. Ranft, "Fluka: A multi-particle transport code (program version 2005)," Report, 2005.

[62] A. V. Dementyev and N. M. Sobolevsky, "shield — universal monte carlo hadron transport code: scope and applications," *Radiation Measurements*, vol. 30, no. 5, pp. 553–557, 1999.

[63] K. Niita, H. Takada, S.-i. Meigo, and Y. Ikeda, “High-energy particle transport code nmtc/-jam,” *Nuclear Instruments and Methods in Physics Research Section B: Beam Interactions with Materials and Atoms*, vol. 184, no. 3, pp. 406–420, 2001.

[64] T. Sato, K. Niita, H. Iwase, H. Nakashima, Y. Yamaguchi, and L. Sihver, “Applicability of particle and heavy ion transport code phits to the shielding design of spacecrafts,” *Radiation measurements*, vol. 41, no. 9, pp. 1142–1146, 2006.

[65] T. Ersmark, P. Carlson, E. Daly, C. Fuglesang, I. Gudowska, B. Lund-Jensen *et al.*, “Status of the desire project: Geant4 physics validation studies and first results from columbus/iss radiation simulations,” in *Nuclear Science Symposium Conference Record, 2003 IEEE*, vol. 3, Conference Proceedings, pp. 1540–1544 Vol.3.

[66] J. Apostolakis, R. Chytracek, G. Cosmo, M. Dressel, V. Grichine, O. Link *et al.*, “Recent developments and upgrades to the geant4 geometry modeller,” in *CHEP*, Conference Proceedings.

[67] R. Chytracek, J. McCormick, W. Pokorski, and G. Santin, “Geometry description markup language for physics simulation and analysis applications,” *Nuclear Science, IEEE Transactions on*, vol. 53, no. 5, pp. 2892–2896, 2006.

[68] Qinetic, “Gps user manual,” 2005.

[69] C. Ferguson, “General purpose source particle module for geant4 sparset: Technical note,” *Uos-GSPM-Tech,*, no. 1.0, 2000.

[70] X.-Y. Zhao, H.-Y. Wang, F. Wu, X.-C. Meng, Y.-Q. Ma, H. Lu *et al.*, “A geometric factor calculation method based on the isotropic flux assumption,” *Chinese Physics C*, vol. 37, no. 12, p. 126201, 2013.

[71] C. GEANT4, “Geant4 10.0 release notes,” 2013. [Online]. Available: http://geant4.cern.ch/support/ReleaseNotes4.10.0.html

[72] T. Jevremovic, *Nuclear principles in engineering*. Springer, 2005, vol. 2006.

[73] C. GEANT4, “Physics reference manual,” 2013.

[74] G. A. P. Cirrone, G. Cuttone, F. Di Rosa, L. Pandola, F. Romano, and Q. Zhang, “Validation of the geant4 electromagnetic photon cross-sections for elements and compounds,” *Nuclear Instruments and Methods in Physics Research Section A: Accelerators, Spectrometers, Detectors and Associated Equipment*, vol. 618, no. 1–3, pp. 315–322.

[75] G. I. Lykasov, G. H. Arakelyan, and M. N. Sergeenko, “The quark–gluon string model: soft and semihard hadronic processes,” *Physics of Particles and Nuclei*, vol. 30, no. 4, pp. 343–368, 1999.

[76] J. Apostolakis, G. Folger, V. Grichine, A. Howard, V. Ivanchenko, M. Kosov *et al.*, “Geant4 physics lists for hep,” in *Nuclear Science Symposium Conference Record, 2008. NSS ’08. IEEE*, Conference Proceedings, pp. 833–836.

[77] C. GEANT4, “Geant4 user’s guide for application developers v10.0,” 2013.

[78] D. Wright, “A short guide to choosing a physics list,” in *Geant4 Tutorial at Marshall Space Flight Center*. SLAC, Conference Proceedings. [Online]. Available: http://geant4.slac.stanford.edu/MSFC2012/ChoosePhys.pdf

[79] T. Koi *et al.*, "New native qmd code in geant4," in *Proceedings of the MC2010 Monte Carlo Conference*, 2010, p. 103.

[80] A. V. Ivantchenko, V. N. Ivanchenko, J. M. Molina, and S. L. Incerti, "Geant4 hadronic physics for space radiation environment," *Int J Radiat Biol*, vol. 88, no. 1-2, pp. 171–5, 2012, ivantchenko, Anton V Ivanchenko, Vladimir N Molina, Jose-Manuel Quesada Incerti, Sebastien L eng England Int J Radiat Biol. 2012 Jan;88(1-2):171-5. doi: 10.3109/09553002.2011.610865. Epub 2011 Sep 22.

[81] M. A. Chavy-Macdonald, A. Menicucci, G. Santin, H. Evans, P. T. A. Jiggens, P. Nieminen *et al.*, "High-accuracy simulations of the iss radiation environment and applications to interplanetary manned missions," *Nuclear Science, IEEE Transactions on*, vol. 60, no. 4, pp. 2427–2434, 2013.

[82] T. Ersmark, P. Carlson, E. Daly, C. Fuglesang, I. Gudowska, B. Lund-Jensen *et al.*, "Geant4 monte carlo simulations of the belt proton radiation environment on board the international space station/columbus," *IEEE Transactions on Nuclear Science*, vol. 54, no. 4, pp. 1444–1453, 2007.

[83] ——, "Geant4 monte carlo simulations of the galactic cosmic ray radiation environment on-board the international space station/columbus," *IEEE Transactions on Nuclear Science*, vol. 54, no. 5, pp. 1854–1862, 2007.

[84] ——, "Influence of geometry model approximations on geant4 simulation results of the columbus/iss radiation environment," *Radiation Measurements*, vol. 42, no. 8, pp. 1342–1350, 2007.

[85] G. Santina, "Normalisation modeling sources," in *Geant4 tutorial*, 2007, Conference Proceedings.

[86] S. M. Seltzer, "Conversion of depth-dose distributions from slab to spherical geometries for space-shielding applications," *Nuclear Science, IEEE Transactions on*, vol. 33, no. 6, pp. 1292–1297, 1986.

[87] D. Xin, C. Gene, A. John, J. Sverre, N. Andrzej, A. Makoto, and B. Daniel, "Creating and improving multi-threaded geant4," *Journal of Physics: Conference Series*, vol. 396, no. 5, p. 052029, 2012.

[88] K. Murakami, K. Amako, Y. Kanematsu, M. G. Pia, T. Sasaki, and H. Yoshida, "Design of simulation framework for generic radiotherapy," in *Nuclear Science Symposium Conference Record, 2004 IEEE*, vol. 3, Conference Proceedings, pp. 1898–1901 Vol. 3.

[89] N. Tsoulfanidis and S. Landsberger, *Measurement and Detection of Radiation, Third Edition*. Taylor & Francis, 2010.

[90] G. D. Badhwar, F. A. Cucinotta, L. A. Braby, and A. Konradi, "Measurements on the shuttle of the let spectra of galactic cosmic radiation and comparison with the radiation transport model," *Radiation Research*, vol. 139, no. 3, pp. 344–351, 1994.

[91] NASA Space Radiation Analysis Group, "How do we protect the astronauts from space radiation?" 2014. [Online]. Available: http://srag-nt.jsc.nasa.gov/SpaceRadiation/How/How.cfm

[92] D. Zhou, *CR-39 plastic nuclear track detectors in physics research.* Hauppauge, N.Y.: Hauppauge, N.Y. : Nova Science Publishers, 2012, includes bibliographical references (p. [179]-188) and index.

[93] G. D. Badhwar, A. Kondradi, A. Hardy, and L. A. Braby, "Active dosimetric measurements on shuttle flights," *International Journal of Radiation Applications and Instrumentation. Part D. Nuclear Tracks and Radiation Measurements*, vol. 20, no. 1, pp. 13–20, 1992.

[94] Y. Uchihori and E. Benton, "Results from the first two intercomparison of dosimetric instruments for cosmic radiation with heavy ions beams at nirs (icchiban1&2) experiments," *HIMAC-078, NIRS Chiba, Japan, February*, 2004.

[95] G. D. Badhwar, M. J. Golightly, A. Konradi, W. Atwell, J. W. Kern, B. Cash *et al.*, "In-flight radiation measurements on sts-60," *Radiation Measurements*, vol. 26, no. 1, pp. 17–34, 1996.

[96] G. D. Badhwar, W. Atwell, E. V. Benton, A. L. Frank, R. P. Keegan, V. E. Dudkin *et al.*, "A study of the radiation environment on board the space shuttle flight sts-57," *Radiation Measurements*, vol. 24, no. 3, pp. 283–289, 1995.

[97] G. D. Badhwar, J. U. Patel, F. A. Cucinotta, and J. W. Wilson, "Measurements of the secondary particle energy spectra in the space shuttle," *Radiation Measurements*, vol. 24, no. 2, pp. 129–138, 1995.

[98] R. Rios, "Calibration and readiness of the iss-rad charged particle detector," 2015.

[99] M. Kroupa, A. Bahadori, T. Campbell-Ricketts, A. Empl, S. M. Hoang, J. Idarraga-Munoz *et al.*, "A semiconductor radiation imaging pixel detector for space radiation dosimetry," *Life Sciences in Space Research*, vol. 6, pp. 69 – 78, 2015.

[100] A. A. Bahadori, E. J. Semones, R. Gaza, M. Kroupa, R. R. Rios, N. N. Stoffle *et al.*, "Battery-operated independent radiation detector data report from exploration flight test 1," Government Document, 2015. [Online]. Available: http://ston.jsc.nasa.gov/collections/trs/_techrep/TP-2015-218575.pdf

[101] E. R. Benton, E. V. Benton, and A. L. Frank, "Neutron dosimetry in low-earth orbit using passive detectors," *Radiation Measurements*, vol. 33, no. 3, pp. 255–263, 2001.

[102] I. Apáthy, S. Deme, L. Bodnár, A. Csöke, and I. Héjja, "An on-board tld system for dose monitoring on the international space station," *Radiation Protection Dosimetry*, vol. 84, no. 1-4, pp. 321–323, 1999.

[103] E. L. Hubbard, E. L. Petroka, D. R. McMorrow, and B. R. Kramer, "The nuclear particle detection system (npds) a proton-alpha particle counter for the apollo system," *Nuclear Instruments and Methods*, vol. 77, no. 1, pp. 125–135, 1970.

[104] G. Reitz, R. Beaujean, E. Benton, S. Burmeister, T. Dachev, S. Deme *et al.*, "Space radiation measurements on-board iss—the dosmap experiment," *Radiation Protection Dosimetry*, vol. 116, no. 1-4, pp. 374–379, 2005.

[105] T. Sakaguchi, T. Doke, N. Hasebe, T. Hayashi, T. Kashiwagi, J. Kikuchi *et al.*, "Let distribution measurement with a new real-time radiation monitoring device-iii onboard the space shuttle sts-84," *Nuclear Instruments and Methods in Physics Research Section A: Accelerators, Spectrometers, Detectors and Associated Equipment*, vol. 437, no. 1, pp. 75–87, 1999.

[106] J. Semkova, R. Koleva, G. Todorova, N. Kanchev, V. Petrov, V. Shurshakov *et al.*, “Experiment for radiation dose measurements in a human phantom onboard the iss for estimation of the radiation risk in long duration space flights,” in *Recent Advances in Space Technologies, 2005. RAST 2005. Proceedings of 2nd International Conference on*, Conference Proceedings, pp. 734–738.

[107] G. Reitz, T. Berger, P. Bilski, R. Facius, M. Hajek, V. Petrov *et al.*, “Astronaut’s organ doses inferred from measurements in a human phantom outside the international space station,” *Radiation Research*, vol. 171, no. 2, pp. 225–235, 2009.

[108] Q. ICRU, “Units in radiation protection dosimetry report 51,” Report, 1 Sep 1993 1993.

[109] E. Semones, “Passive dosimetry: Area and crew monitoring,” NASA- Johnson Space Center, Report, Dec 8, 1999.

[110] ——, “Update on nasa tepc activities september 08 - september 09,” in *14th Workshops on Radiation Monitoring for the International Space Station, Dublin*, Conference Proceedings.

[111] D. Perez-Nunez and L. A. Braby, “Replacement tissue-equivalent proportional counter for the international space station,” *Radiation Protection Dosimetry*, vol. 143, no. 2-4, pp. 394–397, 2011.

[112] D. P. Nunez, “Design, construction and implementation of spherical tissue equivalent proportional counter,” Thesis, 2008.

[113] R. Destefanis, E. Amerio, M. Briccarello, M. Belluco, M. Faraud, E. Tracino, and C. Lobascio, “Space environment characterisation of kevlar®: Good for bullets, debris and radiation too.”

[114] I. Ertel and M. Morse, *The Apollo spacecraft: a chronology vol IV*. Washington, D.C.: National Aeronautics and Space Administration, 1978, vol. IV.

[115] W. D. Compton, *Where no man has gone before : a history of Apollo lunar exploration missions*, ser. The NASA history series. Washington, DC: National Aeronautics and Space Administration, Office of Management, Scientific and Technical Information Division, 1989.

[116] R. H. Hilberg, “Radiation protection for apollo missions - case 340,” Bellcomm, Inc., Report, 1969.

[117] M. Lombardi, “Technical schematics for apollo command module,” 2014.

[118] R. L. Dotts, “Apollo experience report- spacecraft heating environment and thermal protection for launch throught the atmosphere of the earth,” 1973.

[119] S. Schneeweis, “Thickness of apollo heatshield stainless steel,” 2010.

[120] National Aeronautics and Space Administration, “Apollo operations handbook: Command and service modules,” 1968.

[121] *Spacecraft Description: Block II Spacecraft*. National Aeronautics and Space Administration, 1969.

[122] Public Relations Department, “Apollo spacecraft news reference,” pp. 39–52, 1968.

[123] O. E. Pigg and S. P. Weiss, “Apollo experience report - spacecraft structural windows,” National Aeronautics and Space Administration, Report, 1973.

[124] J. E. Pavlosky and L. G. St. Leger, "Apollo experience report thermal protection subsystem," 1974.

[125] R. W. Orloff, "Apollo by the numbers," 1996.

[126] Division, NASA/MSC Computations and Analysis, "Apollo mission 11, trajectory reconstruction and postflight analysis," Report NASA/MSC Report MSC-00171, 16 March 1970 1970.

[127] MISSION PLANNING AND ANALYSIS DIVISION, "Postflight evaluation of the apollo 14 spacecraft trajectories," 1971.

[128] R. Bate, D. Mueller, J. White, and W. Saylor, *Fundamentals of Astrodynamics: Second Edition*. Dover Publications, Incorporated, 2015.

[129] R. A. Braunig, "Apollo 11's translunar trajectory," 2013. [Online]. Available: http://www.braeunig.us/space/orbmech.htm

[130] V. G. Szebehely and H. Mark, *Adventures in celestial mechanics*. John Wiley & Sons, 2008.

[131] *SILSO data*. Royal Observatory of Belgium, Brussels, 2014. [Online]. Available: http://www.sidc.be/silso/

[132] G. M. Simnett, "Solar cosmic radiation during august 1972," *Space Science Reviews*, vol. 19, no. 4-5, pp. 579–610, 1976.

[133] National Aeronautics and Space Administration, *Biomedical results of Apollo*. Washington, D.C.: Washington, D.C. : Scientific and Technical Information Office, National Aeronautics and Space Administration, 1975.

[134] H. W. Dodson and E. R. Hedeman, "Experimental comprehensive solar flare indices for certain flares, 1970-1974," *NASA STI/Recon Technical Report N*, vol. 76, p. 27156, 1975.